El 108

ACTA POLYTECHNICA SCANDINAVICA

ELECTRICAL ENGINEERING SERIES No. 108

Design and Voltage Supply of High-Speed Induction Machines

Jussi Lähteenmäki

Helsinki University of Technology
Laboratory of Electromechanics
P.O.Box 3000
FIN-02015 HUT
Finland

Dissertation for the degree of Doctor of Science in Technology to be presented with due permission of the Department of Electrical and Communications Engineering, for public examination and debate in Auditorium S1 at Helsinki University of Technology (Espoo, Finland), on the 29th of November, 2002, at 12 o'clock noon.

ESPOO 2002

Lähteenmäki J. **Design and Voltage Supply of High-Speed Induction Machines.** Acta Polytechnica Scandinavica, Electrical Engineering Series, No 108, Espoo 2002. 140 p. Published by the Finnish Academies of Technology. ISBN 951-666-607-8, ISSN 0001-6845

Keywords: high-speed induction machine, rotor design, voltage modulation, PAM, PWM, circulatory currents, optimization.

ABSTRACT

The motivation for this work is to find good designs for high-speed induction machines. Special attention is paid to rotors suitable for these machines. Another goal is to find supply voltage waveforms appropriate for a high-speed induction machine with a solid rotor. In order to design good high-speed machines, modeling is modified and verified.

A laminated rotor made for high speeds was tested on a 65 kW 30600 $^{1}/_{\min}$ compressor drive. Two squirrel cage solid steel rotors were tested on a 60 kW 60000 $^{1}/_{\min}$ high-speed machine. In both cases, the rotors were compared against a commercially used copper coated solid steel rotor. The results showed that the laminated construction with a cage should be used whenever possible. At higher speeds, a well-designed squirrel cage solid steel rotor would be better than a copper coated solid steel rotor. The copper coated rotor is preferred at very high speeds.

Pulse amplitude modulation and pulse width modulation are techniques used to adjust the supply voltage of electric machines. The feasibility of these modulation types for supplying high-speed induction machines was tested. The results show that pulse amplitude modulation is the best choice for a high-speed induction motor drive.

For the high-speed machines considered, the 3D effects made the 2D modeling of the electromagnetic properties difficult. Two modifications to the current modeling software were made. In the first modification, the end ring inductance was calculated with a separate 2D FEM model. In the other modification, the flux fringing in the air gap region was also modeled with a separate 2D FEM model.

A discrepancy between electromagnetic loss calculated and electromagnetic loss measured was noticed. The measurements show circulatory currents flowing in the parallel paths of a stator winding of a high-speed machine. These currents produce extra power loss not modeled in the calculations. It is shown that taking circulatory currents into account, the model provides results close to the measured ones. Thus, the model can be used for the designing and optimization of high-speed machines.

Genetic optimization software was used to derive the optimal parameters for a squirrel cage solid steel rotor. General topology suitable for a high-speed induction machine was also studied by using optimization. The results show that both the positioning and the volume of conductors in the rotor are important. Considering the electromagnetic performance, the choice between a laminated and a solid rotor core material is less significant for a high-speed induction machine.

PREFACE

This thesis is the result of a personal desire to study and understand high-speed induction motor drives. The work towards this goal started in 1996 with a master's thesis project and is now reaching a new, if not a final, stage. The work has been carried out in the Laboratory of Electromechanics, Helsinki University of Technology. It has been a part of the "Development of a High-Speed Electric Motor" project. The project has been financed by the Laboratory of Electromechanics, the National Technology Agency TEKES and High Speed Tech Oy Ltd.

I would like to express my gratitude to Professors Tapani Jokinen and Antero Arkkio for their commitment and support throughout the project. I also wish to thank Mr. Jarmo Perho for cooperation seasoned with an especially dry sense of humor and for sharing the same lot in finishing the thesis. I owe thanks to Mr. Kimmo Hamunen for the practical help given on conducting the measurements. I also wish to thank Professor Asko Niemenmaa for his comments on the manuscript of the thesis.

For their long time cooperation and intensive discussion sessions, I would like to thank Dr. Erkki Lantto and Mr. Ville Tommila from High Speed Tech Oy Ltd. For the help with frequency converters, I wish to thank Mr. Martti Alatalo and Mr. Tero Halkosaari from Vacon Plc.

To all the staff of the laboratory during these years, I wish to send my warmest thanks for making the time spent here worthwhile.

Barole Oy was responsible for the proofreading.

The financial support of the Imatran Voima Foundation, Tekniikan Edistämissäätiö and The Graduate School of Electrical Engineering is gratefully acknowledged.

Espoo, September 2002

Jussi Lähteenmäki

CONTENTS

LIST OF SYMBOLS

a	Number of parallel paths in a stator winding
a_c	Average diameter of coil
a_s	Scaling factor
B, $\boldsymbol{B}$	Magnetic flux density
B_r	Radial component of magnetic flux density
B_φ	Tangential component of magnetic flux density
C	Utilization factor
C_f	Friction coefficient
d	Distortion factor
d^2	Loss factor
D_r	Outer diameter of rotor
d_r	Inner diameter of rotor or lamination
$\boldsymbol{E}$	Electric field strength
E	Young's modulus
e_{cc}	Electromotive force producing a circulatory current
f	Frequency
f_{in}	Frequency measured at machine terminal
g	Modulating function
g_a	Modulation index
h_ν	Normalized current of ν^{th} harmonic
I_h	Harmonic current
I_{in}	Current measured at machine terminal
I_r	Rotor current
i	Current
i_1	Fundamental current
i_{ave}	Average strand current
i_n	Strand current
i_{cc}	Circulatory part of strand current
k_{cc}	Circulatory current loss factor
k_f	Roughness coefficient
k_{sc}	Scaling factor
L_{er}	Inductance of end ring

L_l	Inductance of current loop
l_2D	Length of 2D region of stator core
l_eff	Effective core length
l_ic	Length of iron core
l_e	Length of a stator coil end
l_r	Length of rotor
l_s	Length of a stator coil end winding
l_w	Length of a circular part of the stator end winding
m	Number of phases
N_c	Number of turns in series in an air core coil
N_s	Number of parallel conductors
N_p	Pulse number
N_u	Number of turns in series in a stator coil
n	Speed
$\boldsymbol{n}$	Unit vector
P_Cu	Ohmic loss not depending on frequency
P_cc	Stator winding loss in case of circulatory currents
P_ed	Stator winding loss in case of no circulatory currents
P_f	Friction loss
P_h	Harmonics loss
P_in	Power measured at machine terminal
P_L	Total loss
P_m	Electromechanic power
P_out	Output power
P_r	Rotor loss
P_tl	Theoretical load loss
P_δ	Air gap power
p	Number of pole pairs
p_cus	Normalized power loss for stator winding
p_e	Eddy-current loss coefficient
p_f	Friction loss coefficient
p_fes	Normalized power loss for stator iron
p_h	Hysteresis loss coefficient
p_rot	Normalized power loss for rotor
Q	Number of slots
q	Number of slots per pole and phase
R_h	Effective harmonics resistance

R_n	Resistance of a parallel conductor
R_r	Rotor resistance
r	Radius
r_r	Inner radii of the air gap
r_s	Outer radii of the air gap
S	Penalty function term
S_{ag}	Air gap surface
s	Slip
$T_{ambient}$	Ambient temperature
T_e	Electromagnetic torque
T_{PT100}	Temperature measured with PT100 thermoelement
$T_{thermocouples}$	Temperature measured with thermocouples
ΔT	Temperature rise
U_{ac}	Voltage of electricity network
U_d	DC-link voltage
U_1	Fundamental of the supply voltage
U_{in}	Voltage measured at machine terminal
u_n	Voltage of current loop
u_{ref}	Reference voltage signal
V_{rt}	Rotor volume
v_c	Circumferential speed
W	Coil span
w_{cus}	Weight for stator winding power loss
w_{fes}	Weight for stator core power loss
w_{rot}	Weight for rotor power loss
X_s	Leakage reactance of stator
α	Heat transfer coefficient
α_n	Angle between strand current and reference signal
γ	Conductivity
δ	Penetration depth
δ_g	Air gap
λ_e, λ_f, λ_s, λ_w	Empirical coefficients for calculation of leakage reactance
μ_0	Permeability of vacuum
μ_r	Relative permeability
ν	Order of a harmonic
ν_P	Poisson’s number

ξ_ν	Winding factor of a ν^{th} harmonic
ρ	Material density
σ	Leakage factor
σ_{max}	Maximum stress allowed
τ	Pole pitch
Φ_l	Magnetic flux through current loop
Ω_m	Mechanical speed
Ω_s	Synchronous speed
ω	Angular frequency
ω_c	First bending critical speed

Abbreviations

AC	Alternating current
AMB	Active magnetic bearing
CFD	Computational fluid dynamics
CMS	Cross magnetic structure
DC	Direct current
emf	Electromotive force
FEM	Finite element method
FFNF	Free-free natural frequency
GA	Genetic optimization algorithm
GTO	Gate-turn-off thyristor
IGBT	Insulated-gate bipolar transistor
LC	Inductance - capacitance
mmf	Magnetomotive force
PAM	Pulse amplitude modulation
pf	Power factor
pphc	Pulses per half cycle
PWM	Pulse width modulation
rms	Effective (root mean square) value
TEFC	Totally enclosed fan cooled
THD	Total harmonic distortion
VSI	Voltage source inverter
UPS	Uninterruptible power supply

1 INTRODUCTION

The need for high rotational speed is a built-in requirement in some industrial applications. Compressors, pumps and machine tools can often achieve better performance at higher speeds. The energy efficiencies of pump and compressor drives improve at higher speeds. The rate of material removal in a spindle tool is increased by an increase in speed. The sizes of the machines and drives are reduced when the rotational speed is increased.

The Laboratory of Electromechanics has taken part in a project for the development of high-speed drive systems. In the Laboratory, electric high-speed machines and active magnetic bearing systems have been studied. On the machines side, emphasis has been on high-speed induction motors. At the beginning of the project, frequency converters had to be specially made as there were no suitable products on the market.

1.1 High speed electric drive systems

Traditionally, a drive consists of a load machine, a power source and a gearbox. Nowadays, electric induction motors are the most common source of mechanical power. Induction motors are low cost, reliable and easily operated.

Electric motors, which are supplied by the electricity distribution network, have a supply frequency of 50 or 60 Hz. Thus, these motors have a maximum operating speed of 3000 or 3600 $^{1}/_{\mathrm{min}}$. A gearbox in a traditional drive changes that speed into one more suitable for a load machine. Another way to have a high rotational speed is to use a frequency converter, also called as an inverter. The frequency converter transforms the 50/60 Hz supply frequency and voltage into a desired frequency and voltage. High rotational speeds can be achieved and the sizes of the motor and the drive can be reduced. There are fewer components subject to wear and tear if active magnetic bearings are used. Lubrication is not needed anymore. Table 1.1 and Fig. 1.1 show the difference between these two approaches and the benefits of high-speed technology. Fig. 1.2 illustrates a high-speed compressor drive and a rotary compressor drive.

The development of power electronics has made inverters available at the large power vs. speed region. A voltage source inverter and simple scalar control are usually suitable for feeding a high-speed induction motor in the applications considered. Newer power semiconductors can operate at

higher switching frequencies without causing excessive switching loss. Different voltage modulation techniques can be used. The voltage waveforms can be selected or optimized to produce low loss, torque ripple, noise etc., depending on the application and demands.

The use of power electronics together with integrated control and information networks makes it possible to use and supervise the drives efficiently and cost-effectively. Processes can be adjusted without unnecessary losses by simply changing the supply frequency of the electric motor.

Feeding an electric motor from an inverter sets some new requirements for the design of a motor. An increase in a supply frequency further emphasizes these requirements. The supply waveforms of the voltage and current are not sinusoidal and more losses are induced in the motor. Some loss components such as eddy current loss are strongly frequency dependent and its share of the total loss increases as frequency increases. The change in loss balance makes the optimal design of the high-speed motor different from the design of a 50/60 Hz conventional motor.

In this work, high-speed motors with a supply frequency up to 1000 Hz are studied. Output power is in the range of 50 – 65 kW. For an electric motor with one pole pair, the increased frequency means a rotational speed up to 60000 $^{1}/_{\mathrm{min}}$. The torques produced by these motors are around 10 - 20 Nm. In the motors studied, active magnetic bearings are used for contactless suspension. The motors are fed by voltage source frequency converters.

The high-speed induction motor drives considered in this work have all the rotating components attached to the same shaft. The compressor wheel is attached to the same shaft with the rotor. The cooling fan of the motor is attached to the other end of the shaft. The cooling fan blows or sucks the air through the inner parts of the motor, air gap and end winding regions.

Table 1.1 Difference between a conventional and a high-speed compressor drive.

	High-speed drive	Conventional drive
Voltage source inverter	YES	NONE/YES
Electric motor	small size and weight	large size and weight
Gearbox & accessories	NONE	YES
Control of power and work	motor speed control	motor on/off, choking or adjustment of compressor blades, motor speed control
Lubrication	NONE	oil / grease
Mechanical wear	NONE	bearings and gears

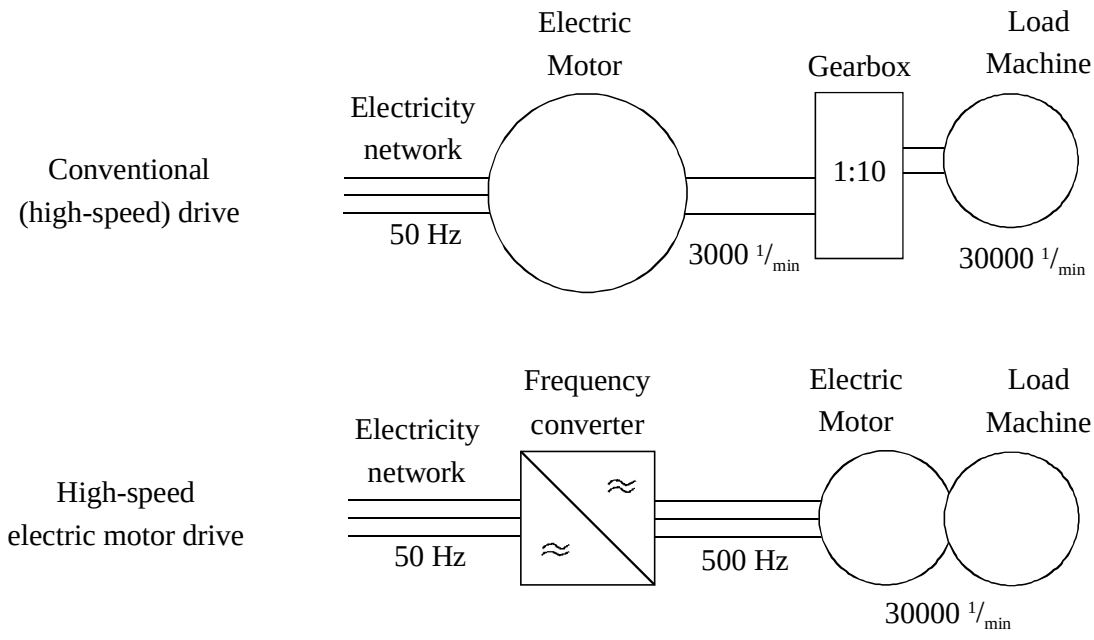

Fig. 1.1 Difference between drives using either a gearbox or an inverter (converter) fed high-speed electric motor.

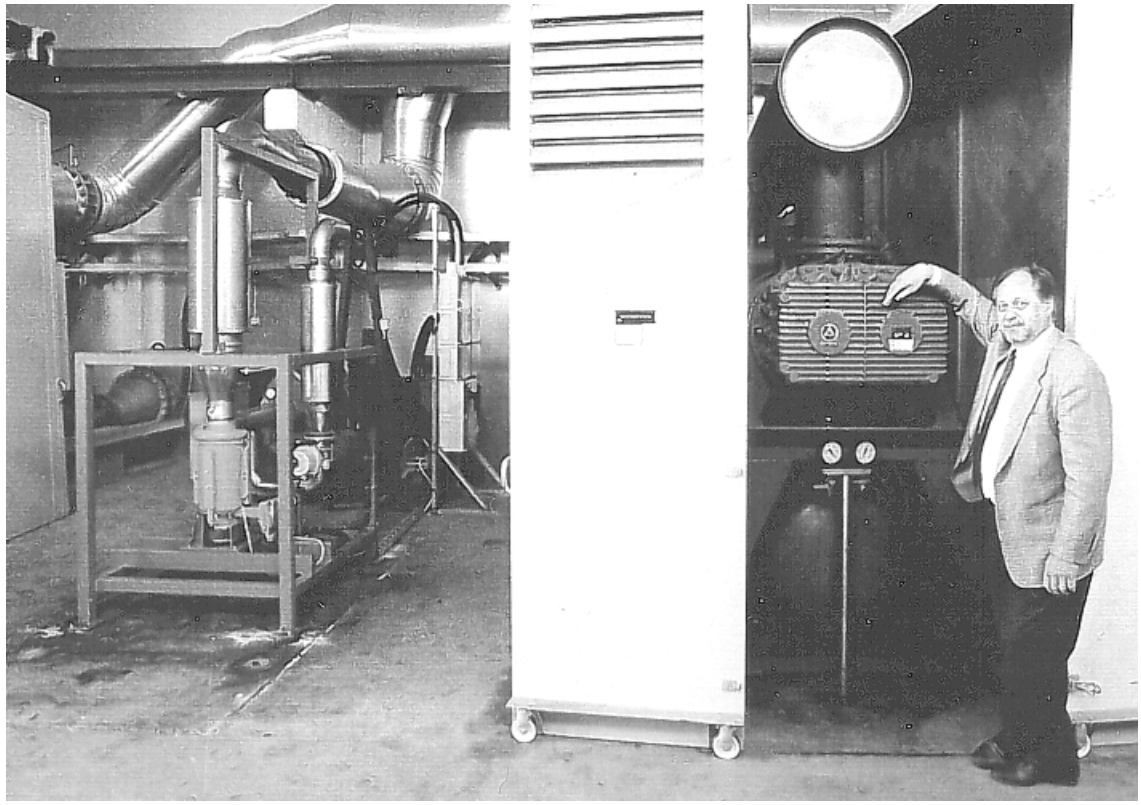

Fig. 1.2 Two approaches for the same task. On the left, a 33000 $^{1}/_{min}$ 32 kW high-speed induction motor drive with gas bearings. On the right, a rotary compressor drive.

1.2 Aim and contents of this work

The motivation and aim of this work is to find good designs for high-speed induction machines. Special attention is paid to rotors suitable for these machines. Another goal is to find supply voltage waveforms appropriate for a high-speed induction machine with a solid rotor. In order to design good high-speed machines, modeling is modified and verified.

In this thesis, comparisons of different rotor constructions are made. A trade-off situation between mechanical and electromagnetic properties is studied. In two measurement cases, different rotors for high-speed induction machines are tested. Different rotor constructions are also studied in two cases of numerical optimization. The optimization algorithm is modified in order to decrease the calculation time and provide data for the post processing of results. Different voltage supply waveforms for a high-speed induction machine are tested. Circulatory currents in a stator winding of a high-speed machine are shown to produce extra power loss and discrepancy between electromagnetic loss measured and calculated. Separate 2D FEM modeling of end ring inductance and effective length of a machine are implemented in the model of the machine.

In Chapter 2 some basic aspects in the design of a high-speed induction motor drive are discussed with references to the field of science. Effects of a high supply frequency on the selection of magnetic materials, slotting and winding are commented on. The importance of dimensioning the air gap is emphasized as perhaps the most important single design parameter. The cooling of a motor is acknowledged as an important subject since loss distribution and loss densities are different from the conventional motors. The frequency converters used and the voltage modulation are presented in the last section.

Chapter 3 concentrates on the rotors of the high-speed induction machines. Section 3.1 describes the mechanical constraints limiting the rotor design. As a starting point for a development, a commercially used copper coated solid steel rotor is presented in Section 3.2. Two alternative approaches are suggested. In Section 3.4, a laminated rotor suitable for high speeds is presented. In Section 3.5, two solid steel rotors with a squirrel cage are presented for a comparison against a copper coated solid steel rotor.

Chapter 4 presents the comparison of the laminated rotor and a copper coated solid steel rotor for a 65 kW 30600 $^{1}/_{\mathrm{min}}$ compressor motor. Section 4.1 describes the measurement setup and Section 4.2 is for the results of the comparison. The compressor itself is used to load the high-speed induction motor. The results are concluded in Section 4.3.

Chapter 5 reports the comparison of the squirrel cage solid steel rotors and a copper coated solid steel rotor for a 60 kW 60000 $^{1}/_{\text{min}}$ motor in a similar fashion. In this case, a back-to-back measurement setup is used. Two identical machines are coupled together, one working as a motor and the other as a generator. This setup provides more information and makes it easier to divide the power loss into components. The actual measurements were made at 50100 $^{1}/_{\text{min}}$.

The effect of different supply voltage waveforms on the performance of the high-speed drive is studied in Chapter 6. Comparison between pulse amplitude modulation and pulse width modulation is presented in Section 6.1. The comparison is done both theoretically and by using measurements. The same back-to-back measurement setup and the same high-speed drives are used as in Chapter 5. The results of the comparison are concluded in Section 6.2.

The modeling and optimization methods used in this study are presented in Chapter 7. Handling of 3D phenomena in a 2D modeling are discussed. End ring inductance is modeled with a separate 2D FEM model in Section 7.1. The effective length of a machine is also modeled with a separate 2D FEM model in Section 7.2. Section 7.3 presents the calculation results for the motor with the copper coated rotor tested in Chapter 5. The results of the calculations are compared against the results from the measurements.

Circulatory currents in parallel paths of a stator winding are studied in Chapter 8. They are shown to generate a considerable amount of extra loss, which is not modeled in the calculation software. Section 8.1 provides the results of individual strand current measurements for the 60 kW 60000 $^{1}/_{\text{min}}$ motor presented in Chapter 5. The circulatory current loss factors are calculated from the results. Impedance of a circulatory current loop is measured in Section 8.2. Using information gained in the sections above, an estimation model for the loss factor is defined in Section 8.3. The model is used to estimate the values of the loss coefficient in the operation points measured in Chapter 5. Taking into account the circulatory current effect, it is shown in Section 8.4 that the model discussed in Chapter 7 gives relatively accurate results. Circulatory currents and voltage modulation are discussed in Section 8.5.

Chapter 9 presents two optimization cases and proposes an improvement to optimization algorithms used with time consuming numerical models. The improvement based on discretization and use of a solution history is presented in Section 9.1. Section 9.2 presents the first optimization case, where a squirrel cage solid steel rotor is optimized. The optimized rotor design is compared against the designs measured in Chapter 5. In the second case, a general topology of a rotor suitable for a high-speed induction machine is studied. This optimization case with results and discussion is presented in Section 9.3. The Summary of the work is given in Chapter 10.

2 CONSTRUCTION OF A HIGH-SPEED MOTOR DRIVE

A high-speed motor has to be designed so that it works well with a high supply frequency provided by an inverter. Mechanical constraints have to be considered carefully, when designing a rotor for high rotational speeds. Friction loss becomes more significant and losses in general are generated in a smaller volume than in a conventional motor. Cooling of a motor has to be adjusted accordingly. The distribution of losses inside the motor also changes and this changes the optimal design.

The answers to these design problems will introduce some differences in the design of a high-speed induction motor, when compared with conventional designs of the same power level. Some of the changes in the design and reasons for them are discussed herein. Being a major issue in this study, the rotor construction is discussed in more detail in Chapter 3. It is emphasized that the effects of some changes are strongly interconnected and a single change cannot be considered without looking at the whole design for a high-speed induction machine.

The high-speed electric machines are fed with an inverter. In voltage source inverters, DC-voltage is modulated in order to have a correct amplitude and frequency for the voltage. In the last section of the chapter, a short introduction to voltage modulation is presented.

2.1 Laminations for high frequencies

An alternating magnetic field induces eddy currents in conductive parts like iron cores and windings. The eddy currents oppose the change of the flux and try to push it out. Thus the magnetic field and flux can only penetrate a certain amount into a conductive material. The inner part of the material cannot be used as a path for the flux. To illustrate this, a concept called a penetration depth δ is used. It is defined as a distance from a surface of a conductive material plane where an amplitude of an electromagnetic incident wave penetrating into the material is decreased by factor e^{-1} or to around 37 % of its original value. This penetration depth is given by the following equation:

$$\delta = \sqrt{\frac{2}{\omega \mu_0 \mu_r \gamma}} = \sqrt{\frac{1}{\pi f \mu_0 \mu_r \gamma}}, \tag{2.1}$$

where ω is the angular frequency and f is the frequency of the incident wave. μ_0 is the permeability of vacuum, μ_r is the relative permeability of the material and γ is the conductivity of the material.

Some penetration depth values are calculated for materials in Table 2.1. The penetration depths for the electric steel sheets are also calculated using Eq. 2.1. In the motors studied, 0.35 mm non-oriented steel sheets have been used.

According to the table, the 0.2 mm sheet would be a good choice for a stator of a high-speed motor supplied with 500 – 1000 Hz fundamental voltage and current. From the point of view of losses, the 0.2 mm sheet is clearly better than the 0.35 mm sheet, although the difference becomes smaller at lower frequencies. At 500 Hz, the specific total loss for the sheets was 27 $^{W}/_{kg}$ against 17 $^{W}/_{kg}$ in favor of the 0.2 mm sheet. Even thinner sheets are available nowadays, as high frequency applications are becoming more common.

The losses are not the only issue in the selection of electric sheets, however. The selection of a lamination is a trade-off situation. The loss values of the sheets clearly suggest the use of thinner laminations. On the other hand, cost and ease of manufacture suggest thicker sheets. Continuing from this, Soong *et al.* (2000) also state the importance of a heat treatment to achieve the proper lamination characteristics. Grain size, elongation and yield strength of the material can be adjusted with different treatments. A large grain size is appropriate to minimize the hysteresis losses in laminations for 50 Hz machines. In a high-speed motor, eddy-current loss become dominant and so a small grain size is more appropriate. With a correct heat treatment, a trade-off between hysteresis and eddy-current loss can be found and the total loss is minimized. The heat treatment also affects

Table 2.1 Penetration depth in different materials.

		copper	steel[1)]	0.35 mm electric steel sheet[2)]		0.20 mm electric steel sheet[3)]	
Conductivity γ [$^{MS}/_{m}$]	@20 °C	59.6	2.58	1.92[4)]		1.61	
Relative permeability μ_r	@1 T	1	602@50Hz	6153@50Hz	3362@1000Hz	5092@50Hz	4461@800Hz
Penetration depth δ [mm]	@10 Hz	21	4.0	1.46		1.76	
	@50 Hz	9.2	1.8	0.65		0.79	
	@500 Hz	2.9			0.28		0.27
	@1000 Hz	2.1			0.20		0.19
Specific total loss [$^{W}/_{kg}$]	@1 T	-	-	1.02@50Hz	86@1000Hz	0.97@50Hz	44@1000Hz

[1)] Imacro, permeability taken from the virgin curve

[2)] Bochum V270-35A, permeability for peak magnetic polarization vs. peak magnetic field strength

[3)] Bochum HF-20, permeability for peak magnetic polarization vs. peak magnetic field strength

[4)] Typical value for steel grade M270-35A of European Standard EN10106 (Surahammars Bruk 1998)

the strength and ductility of the material. Basically, these two properties are only important at the rotor laminations. There the goal would be to achieve maximum yield strength while keeping the necessary level of ductility in order to avoid a cracking of a material.

The manufacture of the lamination stack has effects on the characteristics of the sheet (Boglietti 1999, Smith and Edey 1995). Punching of the sheets, for example, decrease the electromagnetic properties of the sheet by inflicting high stress, altering the grain structure and removing the insulation coating. The teeth of a high-speed stator or a rotor may be small and so the relative area of the detoriating sheet can be large. More expensive manufacture techniques like precision punching or laser cutting may have to be used. Soong *et al*. (2000) and Pyrhönen and Kurronen (1993) have used laser cutting instead of punching.

Stacking of the sheets also has an effect on the electromagnetic properties. Mechanical stress may have a similar kind of detoriating effect as punching. The stacking process must also address the question of material homogeneities and the type of magnetic field variation that the stack is subject to. In AC motors, mainly non-oriented sheets are used in the stator stacks. Because there are small non-homogeneities due to the rolling of the sheets, the sheets are stacked so that the rolling direction of the sheets varies throughout the stack. In the motors studied in this work, for example, every $1/30^{th}$ part of the stack is rotated 60 degrees from the previous part. Another issue is the type of the magnetic field variation. Bertotti *et al*. (1991) demonstrates that the loci of a time-varying magnetic field is very different in different locations of a stator; alternating in places like inside the teeth, rotating in places like the yoke end of the teeth and elliptical in places like yoke. This raises a question as to whether oriented sheets should be used as proposed by Boglietti *et al*. (1988). They suggest that single oriented sheets could be stacked orthogonally so as to resemble a stack of bi-oriented sheets. This Cross Magnetic Structure (CMS) is said to produce less iron loss than a stack of non-oriented sheets.

Table 2.1 also showed the data for the solid steel used in the rotors studied. The steel has high conductivity and low permeability compared to the sheets. If measured, the specific total loss would be high. If a solid steel rotor is used, the solid steel has to carry torque producing currents and the magnetic flux. In this sense, high conductivity and permeability would be ideal. This kind of material would produce the highest torque per volume but also high loss density. However, if the rotor had a copper coating or bars to carry the current, lower conductivity steels can be used mainly as a flux path and the copper sections will carry the current for less resistive loss. The rotor of a high-speed motor is considered in more detail in Chapter 3.

2.2 Stator windings for high-speeds

Perhaps the most important thing in the design of the high-speed motor is to have a smooth sinusoidal air gap flux at the surface of the rotor. Otherwise, the harmonic components will induce a considerable amount of loss on the rotor. This is especially so if solid rotors are used. This issue is discussed a lot in literature and the solutions proposed can be divided into two groups. One group of solutions tries to make the magnetomotive force (mmf) produced by stator windings as sinusoidal as possible. Thus, the aim is the reduction of the winding harmonics. The other group of solutions tries to make the air gap permeance as smooth as possible. Solutions from both groups can be used at the same time in order to reduce the harmonic content of the air gap flux. The solutions aiming for the reduction of permeance harmonics are discussed in the next section.

Conventional induction motors usually have a single layer winding in the power range of the motors studied. A high-speed motor is more sensitive to the winding harmonics and a smoother mmf waveform is required. This can be done either by increasing the number of slots or by using a chorded two layer winding. In principle, the more slots the better, provided that there is enough room for the teeth and that the slots do not become too small. The reduction in loss at the rotor side usually covers the increase of iron loss at the stator side. Some of the winding harmonics have the same winding factor value as the fundamental component. These so-called slot harmonics are pushed higher in the harmonics spectrum when the number of the slots is increased. This can be seen in Table 2.2. The leakage factor at the bottom of the table describes the harmonics content of the mmf. It can be seen that the quality of the mmf improves with the increase in slots.

The stator design can also be improved by selecting a short pitch double layer winding. The pitching decreases the harmonic contents of the mmf and the air gap flux effectively. Perhaps the only drawback is the decrease of the slot filling factor due to main voltage insulation needed between two phases in a same slot. The winding factor for the fundamental mmf is also reduced slightly. Pyrhönen and Kurronen (1994) were quite satisfied with the results when changing from a 24 slot full pitch winding to a 5/6 pitch chorded winding.

Fig. 2.1 illustrates the 36 slot full pitch (one layer) and a 5/6 pitch (double layer) windings for one phase. Table 2.2 shows the winding factors ξ_v for 24 and 36 slot windings with a full pitch or a 5/6 pitch. It can be seen that the quality of the mmf is improved with chording. The winding factors are calculated using the following formula (Richter 1951) :

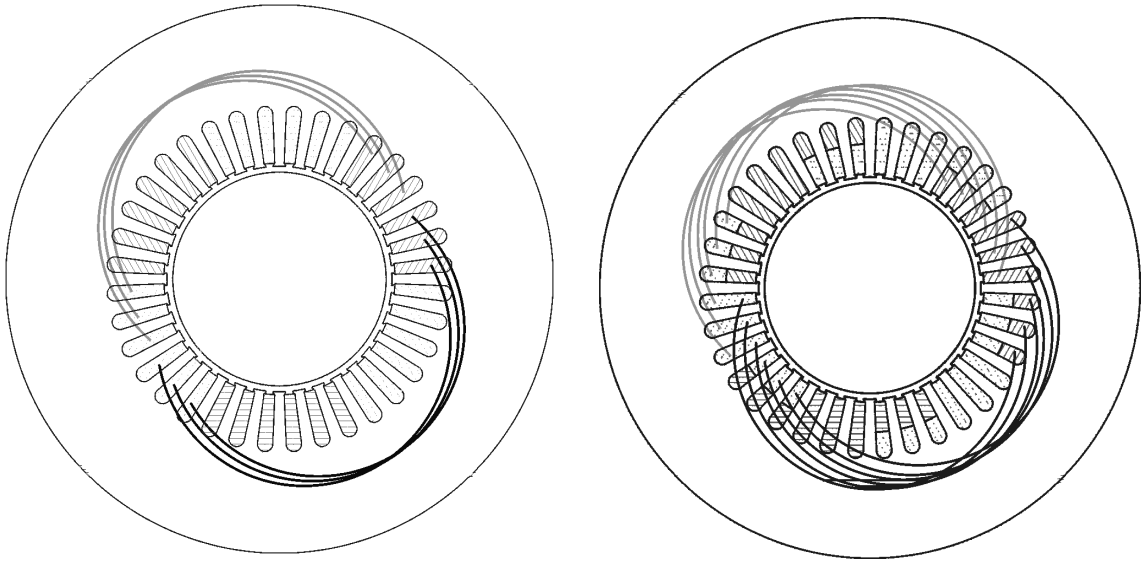

Fig. 2.1 On the left, one phase of a full pitch (one layer) winding for a 36 slot stator. On the right, one phase of a 5/6 pitch (double layer) windings for the same stator.

Table 2.2 Winding factors ξ_ν for three phase windings with one pole pair up to a harmonic number 37. Slot harmonics are shown in italics. m=3, p=1

ν	Q=24 W/τ=1	Q=24 W/τ=5/6	Q=36 W/τ=1	Q=36 W/τ=5/6
1	0.958	0.925	0.956	0.924
5	0.205	0.053	0.197	0.051
7	0.158	0.041	0.145	0.038
11	0.126	0.122	0.102	0.098
13	0.126	0.122	0.092	0.089
17	0.158	0.041	0.084	0.022
19	0.205	0.053	0.084	0.022
23	*0.958*	*0.925*	0.092	0.089
25	*0.958*	*0.925*	0.102	0.098
29	0.205	0.053	0.145	0.038
31	0.158	0.041	0.197	0.051
35	0.126	0.122	*0.956*	*0.924*
37	0.126	0.122	*0.956*	*0.924*
$\sigma_{\delta,\nu\le 1000}$	0.0088	0.0062	0.0051	0.0029

$$\xi_\nu = \sin\left(\nu\frac{\pi}{2m}\right)\frac{\sin\left(\nu\frac{\pi}{2m}\right)}{q\sin\left(\nu\frac{\pi}{2mq}\right)}\sin\left(\nu\frac{\pi}{2}\frac{W}{\tau}\right), \tag{2.2}$$

where m is the number of phases, q is the number of slots per pole per phase, W is the coil span, τ is the pole pitch and ν is the order of harmonic:

$$\nu = 2km + 1, \qquad k \in \mathrm{N} \tag{2.3}$$

The leakage factor σ describing the harmonics content of the mmf is:

$$\sigma = \sum_{\nu\neq 1}\left(\frac{\xi_\nu}{\nu\xi_1}\right)^2 \tag{2.4}$$

The high frequency currents and stray flux may cause considerable skin effect and eddy-current loss in the windings. To avoid this, random wound windings consisting of thin conductors are used. Mekhiche *et al*. (1999) have used Litz wire. This kind of a filamentary conductor is used in high frequency transformers and inductors. Litz wire yields low power loss but it can be more expensive than conventional enamel coated conductors.

Another design problem related to windings is that rotor dynamic limitations often suggest quite short but wide constructions for the rotor and for the stator accordingly. For a two pole motor, this means relatively long end windings resulting in relatively higher ohmic loss and leakage inductance. A four pole motor would be better in this sense but it would mean a double supply frequency, higher iron loss, increased skin effect and higher switching loss for the inverter. Consequently, another trade-off situation must be solved herein.

2.3 Air gap and slot opening

In addition to reduced winding harmonics, a decrease in the permeance harmonics is needed in order to have a smooth sinusoidal air gap flux at the rotor side. Perhaps the most important single parameter in the whole design of a high-speed motor, the air gap, affects the air gap permeance variation a lot. A long air gap is needed to dampen the harmonic components of the magnetic flux seen by the solid rotor surface. As mentioned in previous section, the harmonics can induce most of the losses at the rotor side.

For an induction motor, the long air gap is a problem because the rotor has to be magnetized from the stator side. This means a high magnetization current, increased ohmic loss in stator windings

and a low power factor. However, a common opinion seems to be that the increased need of magnetization is more than compensated for by the reduction in rotor loss.

Andresen *et al.* (1986) made a test for a 7 kW 50 Hz induction motor. The initial air gap, 0.35 mm, was selected according to rules commonly used. During the measurements, the authors reduced the diameter of the rotor by grinding in two steps. The resulting air gap was increased to 0.5 mm and finally up to 0.67 mm. Sinusoidal voltage supply was used to run the motor at 50, 100 and 150 Hz. The results at a nominal torque showed that larger air gaps yielded much less power loss for the motor as the frequency was increased. Total loss at 150 Hz dropped by a third, when the air gap was increased from 0.35 mm to 0.67 mm. At 50 Hz and especially at no-load, the differences were small. This was due to increased winding loss compensating the decreased additional iron loss.

The results apply in similar fashion also for the inverter fed induction machines operating at even higher frequencies. Thus, the selection of an air gap is mainly based on balancing the loss components so that the sum of the losses is minimized (Patent US 5473211). Also, the air gap affects the cooling if the cooling flow is forced through the air gap. This is the case in the motors considered. The loss balance is discussed in the next section.

Table 2.3 shows the air gap δ_g of the motors studied in this work and of some high-speed induction motors reported in the literature. The ratio of δ_g per the rotor diameter D_r, the rotor type, nominal power, nominal speed and the reference are given. It can be seen that the air gap is roughly ten times higher in a high-speed motor compared to a conventional one. Still, good motors with good efficiency values are reported and it seems that motors with a large air gap are the solution for high-speed applications.

The problem of magnetization of a high-speed motor could be avoided by using a permanent magnet rotor. On the other hand, the mechanical design of the permanent magnet rotor needs special care, as the rotor is not as robust as solid steel rotors. These different motor types respond to a different trade-off between electromagnetic and mechanical requirements and so both approaches can be justified.

The other way to decrease the permeance harmonics is to minimize the effect of the stator slot opening by making it as small as possible (Takahashi *et al*. 1994, Lähteenmäki 1997). Magnetic or semi-magnetic slot wedges close the slot opening totally and smoothen the permeance fluctuation to a greater degree (Kaga *et al*. 1982). The down side is the increased leakage reactance. In addition to the solutions mentioned, Pyrhönen and Kurronen (1994) have tested a new kind of tooth tip shape

Table 2.3 Air gap characteristics of some high-speed induction motors and a conventional induction motor. The air gap is 'iron-to-iron' airgap.

δ_g/D_r [%] [1)]	δ_g [mm] [1)]	Rotor type	Power [kW]	Speed [$^1/_{min}$]	Reference
5.7	4.00	solid coated	60	100000	Saari and Arkkio 1994
5.0	4.50	solid coated	60	60000	Lähteenmäki and Soitu 2000[2)]
5.0	4.50	solid coated	50	30600	Lähteenmäki *et al.* 1999[2)]
2.8	2.50	solid caged	50	50000	Lähteenmäki and Soitu 2000[2)]
2.5	1.27	laminated	21	50000	Soong *et al.* 2000
2.4	2.15	laminated	50	30600	Lähteenmäki *et al.* 1999[2)]
1.1	0.95	solid solid slitted solid caged	12	13500	Pyrhönen and Huppunen 1996
1.0	1.00	solid solid coated solid double coated	12	24000	Pyrhönen and Kurronen 1994
0.8	0.40	solid solid double coated	0.7	24000	Sharma *et al.* 1996
0.4	0.80	laminated	37	1500	conventional motor

[1)] Some data not mentioned in the references; derived from other data or requested from the authors

[2)] Case in Chapter 4 is presented in Lähteenmäki *et al.* (1999) and case in Chapter 5 in Lähteenmäki and Soitu (2000)

which enforces the fringing effect at the slot opening, thus smoothing the flux distribution. The possible downsides of this approach are the difficulties and expenses in manufacture.

2.4 Losses and cooling of a high-speed motor

The loss balance of a high-speed motor is different if compared against a conventional motor. Because the phenomena behind the loss components are frequency or speed dependent in different ways, the relative shares of the loss components change with the change of speed. The following quotient of total loss P_L per output power P_{out} illustrates this (Jokinen and Arkkio 1996):

$$\frac{P_L}{P_{out}} = \frac{P_{Cu} + p_h n + p_e n^2 + p_f n^3}{C V_{rt} n}, \tag{2.5}$$

where P_{Cu} is the ohmic loss not depending on frequency and p_h, p_e and p_f are the loss coefficients for hysteresis, eddy-current and friction loss. C is the utilization factor, which describes how much torque per volume unit can be taken out from the rotor of a volume V_{rt}. Letter n stands for the speed.

It is seen that the relative share of ohmic loss decreases and the shares of eddy-current and friction loss increase as a function of speed. The equation gives a slightly simplified behavior and does not hold for a large change of speed. However, it illustrates well the idea of a loss distribution being a function of speed. The change in the distribution gives a clue that the design of the motor should also change as a function of a frequency.

Saari (1995) gave an example of difference in loss distribution between a conventional and a high-speed induction motor. The total losses of the 37 kW induction motors are shown in Fig. 2.2. There were less resistive stator losses in the high-speed motor because of lower winding resistance. The core losses were reduced with an increased air gap and thinner electric steel sheets. There were over four times more friction, cooling and bearing losses in the high-speed motor, resulting in a higher total loss.

Using design parameters given in Saari's work, it can be calculated that the volumes of the stator and rotor in the high-speed motor were only 23 % and 5 % of the volumes in the conventional motor. This example shows well that the loss density of a high-speed motor is higher. High loss densities affect the ideal topology of the motor. Totally enclosed fan cooled (TEFC) motors are not feasible, since a major part of loss is friction and cooling losses generated in the air gap region. The hot air at the air gap must be taken out so that it does not start heating the stator and rotor. Thus, in the motors studied by Saari and in the motors studied in this work, a forced open circuit air-cooling is used. The air is circulated through the air gap and end windings space as shown in Appendix B.

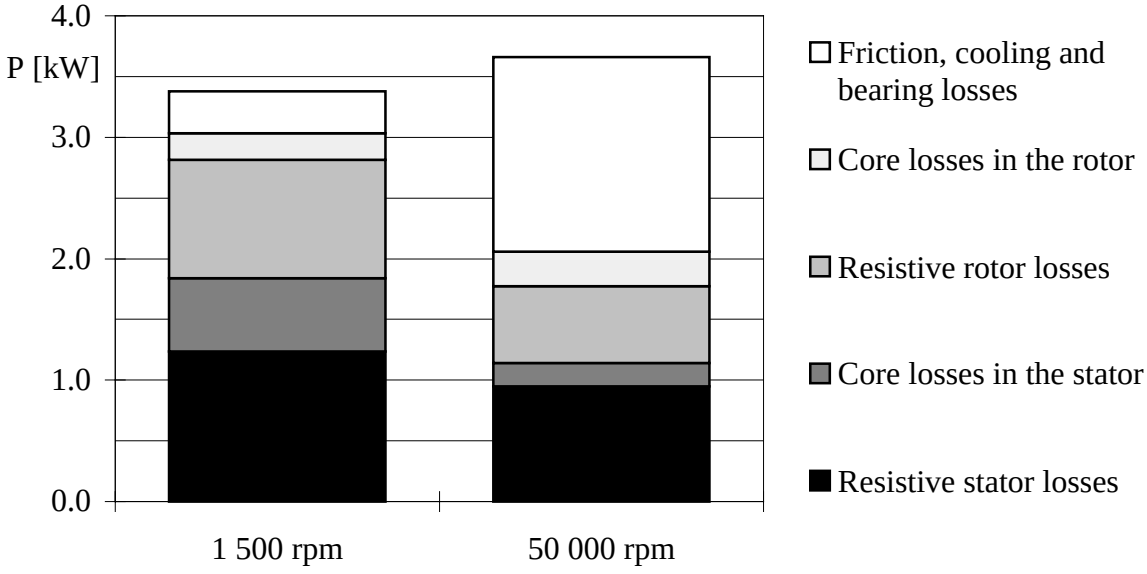

Fig. 2.2 Power losses of the 37 kW normal and high-speed electrical motors (Saari 1995). The high-speed motor is equipped with a copper coated sold steel rotor.

Cooling of the stator could need axial or radial cooling ducts for coolants but in the motors studied this was not necessary. The fact that the stator was actually divided into two parts by a radial duct was primarily because of the need to have cooling air circulation for the rotor. The cooling fan is attached to the other end of the shaft. The fan either blows or sucks the air through the motor. From the temperature rise point of view it is better to suck the air through the motor, since then the loss corresponding to the pressure drop over the motor is not warming up the motor.

It is worth remembering that different motor constructions may benefit from different kinds of cooling arrangements. Different coolants and cooling flow topologies can be chosen. In some cases, direct cooling of a rotor is considered costly and efficient stator cooling is used instead (Boglietti *et al*. 1992). Fuchs and Frank (1983a, 1983b) go on to design a 75 kW 40000 $^{1}/_{\mathrm{min}}$ homopolar motor in order to avoid direct cooling. This is a good example, showing that the selection of a cooling system and a motor type go hand in hand. The approach chosen by Fuchs and Frank is different from the approach chosen in the project (including this work). The choice between different approaches is a complicated issue that may be difficult to formulate exclusively. The problem of choice comes down to the definition and weighting of the objectives, which is strictly speaking never the same for two different projects.

Hydrogen or helium could be used as a closed circuit coolant because of reduced friction and cooling loss and increased heat transfer (Gilon 1994, Saari and Arkkio 1995). Other cooling systems like cooling of the stator with water or R134a could be combined for maximum performance (Mekhiche *et al*. 1999).

2.5 Voltage modulation for the high-speed induction motor

The following description introduces the subject briefly. The idea is to illustrate the type of frequency converter used in this work and the basic idea in the pulse amplitude and pulse width modulation. More information can be found e.g. from Mohan *et al.* (1995).

On the input or supply network side of the frequency converter, there is a three phase choke and diode bridge rectifier. Together with an intermediate or DC-link capacitor, the AC-voltage of the supply network is rectified into a DC-voltage. On the output or load side, there is a three phase IGBT inverter bridge changing the DC-voltage back into AC-voltage of some amplitude and frequency. A schematic diagram of the converter can be found in Fig. 5.2 in Section 5.1.

The DC-voltage U_{d} produced by a diode bridge rectifier depends mainly on the amplitude of the AC-voltage in the supply network U_{ac}. In an ideal case, U_{d} is

$$U_{\mathrm{d}} = \frac{3\sqrt{2}}{\pi} U_{\mathrm{ac}} \tag{2.6}$$

If the DC-link is not loaded, the voltage over the capacitor can be slightly higher, charged to the peak-to-peak value of the diode bridge rectifier:

$$U_{\mathrm{d}} = \sqrt{2} U_{\mathrm{ac}} \tag{2.7}$$

The voltage source inverters (VSI) in general change U_{d} into an AC-voltage of some amplitude and frequency. This is done using gate turn-off (GTO) thyristor or insulated-gate bipolar transistor (IGBT) bridges, for example. The output frequency is inherently determined by the inverter bridge control. For the output voltage, there are more possibilities.

In the pulse amplitude modulation (PAM), the output line-to-ground voltage waveform consists of one pulse per half a cycle. For a three phase system, the length of a phase-to-phase pulse is 120 electrical degrees as shown in the bottom graph of Fig. 2.3. In the case of star connected stator winding, these pulses form a four-step phase voltage and a two-step phase-to-phase voltage. The voltage level is adjusted by changing the amplitude of the pulse. In the frequency converter, the height of the pulse is determined by the DC-link voltage. In the frequency converter used, the diode bridge rectifier cannot adjust U_{d}. The amplitude of pulses is always $\pm U_{\mathrm{d}}$. Using Eq. 2.6, the amplitude of the fundamental of the output voltage U_1 is

$$U_1 = \frac{\sqrt{6}}{\pi} U_{\mathrm{d}} = \frac{6\sqrt{3}}{\pi^2} U_{\mathrm{ac}} \tag{2.8}$$

Thus, another method other than PAM must be used to adjust the output voltage in this case. The common solution is to also use the inverter bridge for the voltage control. In the pulse width modulation (PWM), the output voltage waveform consists of many pulses per half a cycle as shown in Fig. 2.4. The voltage level is adjusted by changing the width of the pulses. The height of the pulses is constant. The maximum voltage corresponds to the situation when there is only one pulse per half a cycle and Eq. 2.8 applies.

There are different ways to select or to modulate the voltage pulse waveforms in PWM. In this work, the VSI's use a synchronized carrier, sine-triangle comparison with added 3$^{\mathrm{rd}}$ harmonic. The actual number of pulses per half a cycle depends on the pulse number N_{p} defined as the ratio of switching frequency f_{sw} and the output frequency f_{s}

$$N_{\mathrm{p}} = \frac{f_{\mathrm{sw}}}{f_{\mathrm{s}}} \tag{2.9}$$

The switching frequency is the frequency at which the inverter bridge can connect the output line to positive or negative DC-link voltage and back. In case of synchronized modulation, N_{p} must be an integer. For the carrier comparison method used, N_{p} must be odd and dividable by three in order to have quarter and half wave symmetric voltage:

$$N_{\mathrm{p}} = 3k \qquad k = 1,3,5,... \tag{2.10}$$

The amount of the 3rd harmonic added to the sine wave is 1/6 of the sine in the VSI used in this work. The modulating function $g(t)$ for one inverter bridge is then

$$g(t) = g_{\mathrm{a}}\left(\sin(\omega t) + \frac{1}{6}\sin(3\omega t)\right), \tag{2.11}$$

where g_{a} is the modulation index. Adding of the 3rd harmonic results in having a flat top modulation function. The 3rd harmonic does not cause any currents in a symmetric three phase system. g_{a} is defined as a ratio of amplitude of the modulating signal per the amplitude of the triangular carrier signal. The output voltage is linearly dependent on g_{a}, when $g(t) \leq 1$. The amplitude of the carrier signal is constantly 1. It can be seen that adding of 3rd harmonic increases the linear operation area for the fundamental part of $g(t)$.

Fig. 2.4 shows an example of this type of PWM modulation. More information on this and other PWM techniques is given in Holz (1994), in which the modulation method used here is called a synchronized carrier modulation implemented with suboscillation method.

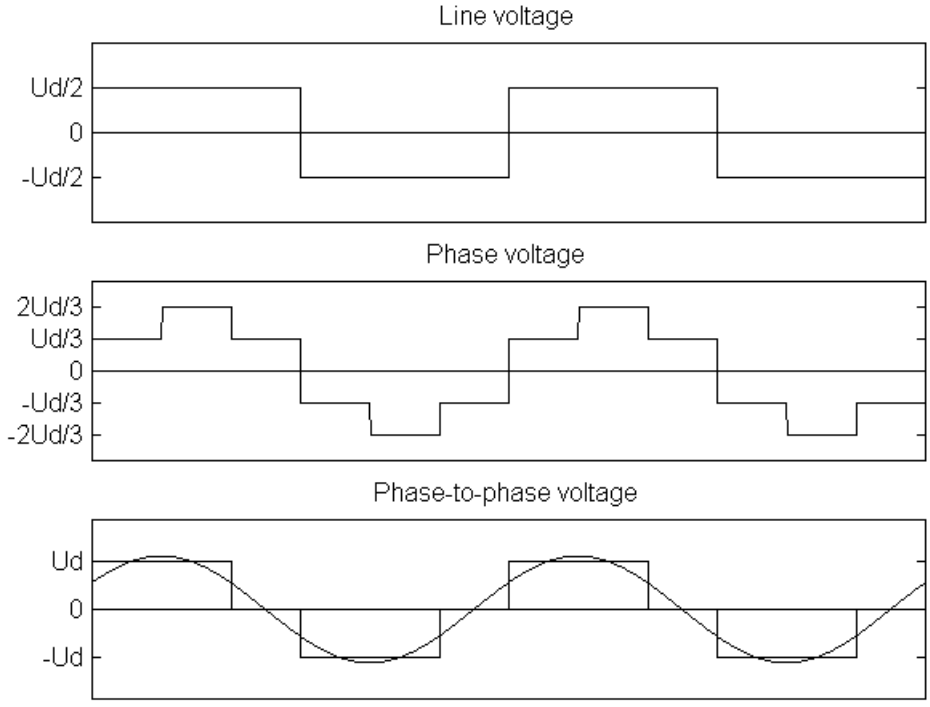

Fig 2.3 Output voltages produced by PAM for a star connected three phase winding. Fundamental of phase-to-phase voltage also plotted.

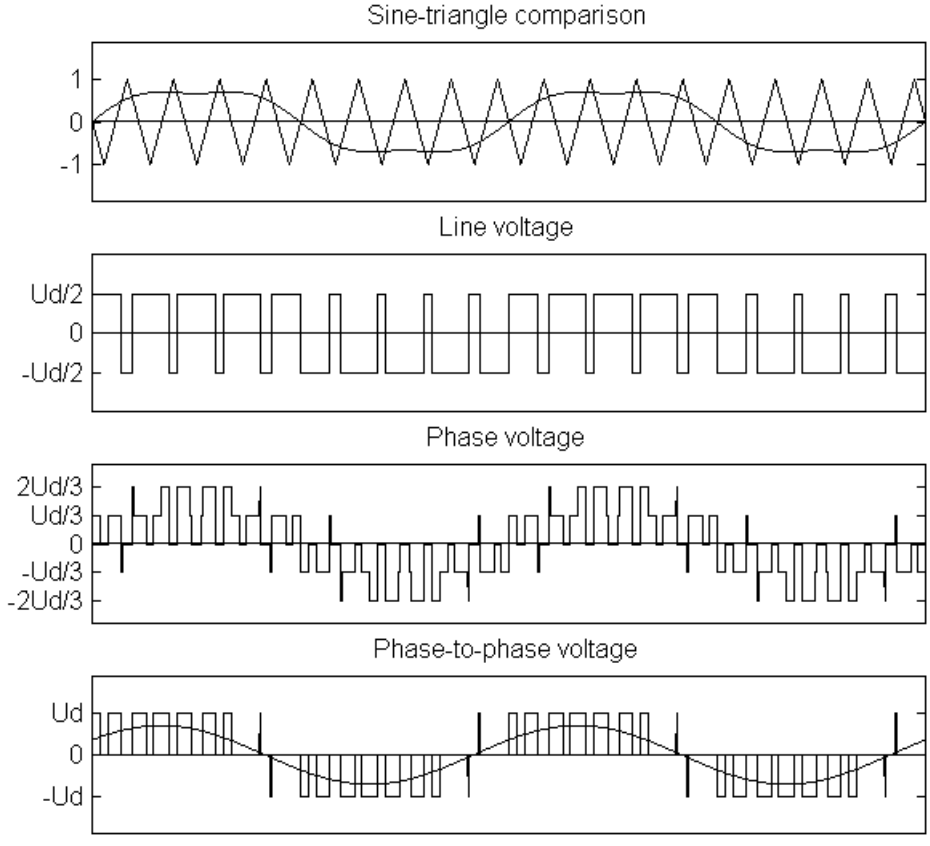

Fig. 2.4 Output voltages produced by PWM for a star connected three phase winding. Fundamental of phase-to-phase voltage also plotted. $N_p = 9$ and $g_a = 0.8$.

3 ROTOR CONSTRUCTIONS

Starting from Francois Aragon's experiments in 1824, electromagnetic induction and applications were studied and experimented with by Faraday, Ferraris and Tesla among others (Lindell 1994). Ferraris built several types of induction motors with a copper cylinder rotor in the 1880's. He came to the conclusion that a maximum efficiency of 50 % could be achieved at 50 % slip. Tesla put his copper winding, or a cage, on a solid iron cylinder. In this way efficiencies higher than 50 % were achieved. In the 1891 Electrical Exhibition in Frankfurt, Germany, both Dolivo-Dobrowolski and Brown introduced three phase induction motors with efficiencies of around 90 %. Coming to the 20^{th} century, induction motor construction was principally the same as it is today. At some time, the lamination technique used in dynamos and transformers was adopted for the rotors of induction machines as well.

In order to have a good efficiency, the rotor of an induction motor should usually provide the following two basic functions.

- High permeability flux path is needed so that most of the magnetic field energy generated is usable at the air gap for the production of the torque.
- The rotor has to have low resistivity flow paths for the electric currents induced so that the ohmic losses relating to torque producing currents are low.

$\Rightarrow$ Ferromagnetic materials have the high permeability needed but they lack the low resistivity if compared to other metals. This problem is usually solved so that the two functions are performed by different parts of the rotor.

This kind of functional division calls for electromagnetic anisotropy in the rotor. Usually, the anisotropy is realized with mechanical design. The so-called core part is made of laminated ferromagnetic material and the current circuit part is made of high conductivity metal, usually copper or aluminum. The current part is usually referred to as a cage winding or a squirrel cage in an ordinary induction motor. Another way to realize the anisotropy would be the use of anisotropic materials or material matrixes as suggested by Ito *et al.* (1988) .

Laminating the ferromagnetic core has some benefits. Firstly, it increases the resistivity seen by eddy-currents. The torque producing currents are forced to use the low resistivity squirrel cage and

the anisotropy is thus enforced. More importantly, hindering the eddy-currents in the magnetic flux path ensures that the flux can penetrate the rotor as planned. Eddy-currents try to push the inducing magnetic field out of the rotor and the magnetic flux would then be pressed near to the surface of the rotor. Magnetic saturation would occur and inner parts of the core and the squirrel cage would become useless. The effect of resistivity on penetration depth and laminations in general was briefly touched on in Section 2.1.

In a relatively low slip operation the use of the solid core would not be a problem. In synchronous machines, there is no slip and the rotor core can be made of solid material because only the harmonics induce eddy currents there. But for high-speed induction machines, even a low slip operation means relatively high frequencies. Another problem with a solid rotor is the harmonics as they can be the main source of loss in the rotor. For the harmonics, the slip is always higher than one, yielding small penetration depth. The harmonic flux components concentrate on the surface of the rotor and if the surface is not laminated or slitted or of high resistivity, high eddy-current loss will occur.

The reduction of harmonic loss is studied and reported by many authors. In sections 2.2 and 2.3, the way in which the harmonic loss could be minimized by changing the stator and air gap parameters of the machine design was studied. On the rotor side, similar effort has been put in order to solve the problem. A more conventional method is the slitting or grooving of the rotor surface. The surface impedance of the rotor is increased and hence saturation together with eddy-current loss decreases. A more fundamental approach can be read from Rajagopalan and Balarama Murty (1969). The slitting is often done axially along the air gap, as was done in a solid rotor by Pyrhönen and Huppunen (1996). An example of a circumferentially grooved rotor is presented by Ikeda *et al.* (1990)

The downside in the axial slitting is that at very high speeds the friction between the rotating rotor and the air increases. This means increased friction loss which can outweigh the gains in reduced harmonic loss. The importance of friction loss could be seen in Fig. 2.2. However, if the slitting is seen as a good thing to do, the increase in friction loss can be eliminated by using retainer rings, i.e., smooth cylindrical sleeves. This technique is often used in homopolar high-speed motors (Fuchs and Frank 1983a). The sleeves are also used to strengthen the mechanical construction. This often becomes important in high-speed permanent magnet motors, where the permanent magnets could need an additional support (Takahashi *et al.* 1994).

In order to avoid slitting, other methods have been studied. It could be said that the slits or grooves are guiding the fundamental flux component into the rotor, whereas the harmonic flux components

and eddy-currents traveling on the rotor surface see increased impedance. The same effect can be achieved by using different materials. Pyrhönen and Kurronen (1994) used aluminum-iron alloys to coat a solid rotor. The surface impedance became high and eddy-current loss was reduced. The result was even better when a copper layer was put between the aluminum-iron layer and the solid core. With the copper layer the resistance seen by fundamental currents was reduced. This yields a lower slip relative to the torque, which is essential in a high-speed machine in order to have a non-saturated and efficient operation. This result was also attained by Sharma *et al.* (1996), when they tested copper, iron-cobalt and iron-nickel layers on a solid steel rotor.

In conclusion, laminated squirrel cage rotors for high-speed induction motors are preferred because of better electromagnetic characteristics. With solid rotors, the efficiency tends to be poor and the machines would need to be larger or increased cooling would be required. However, in high-speed applications, the mechanical properties of solid materials are well in place. In fact, at a very high power vs. speed range the historical concept of a solid rotor motor may be the only possible solution. The mechanical constraints of the rotor are discussed next and the literature review in Table 3.1 will show that solid steel rotors are adopted widely in high power high speed applications.

3.1 Constraints for a high-speed rotor

In the following, the major constraints for a high-speed rotor are presented on a general level. An accurate modeling of these phenomena requires specialization in the field not presented here. Some references are given for the models used in this research project.

The constraints limiting the design of a high-speed rotor could be divided into mechanical and thermal constraints. These constraints affect the choice of materials used in rotors as well as the right length/diameter ratio. The thermal constraints relate to the loss components inside the rotor and in the air gap. They also relate to the choice of the cooling system. The mechanical constraints often dominate the design. They give limits to the size of the rotor, affect the choice of materials and set requirements for the quality of manufacture and manufacture techniques. Mechanical as well as thermal constraints are affected by the application. A good compressor or a spindle tool design may look different because of different boundary conditions given. The different, often contradictory constraints for a rotor affect each other so they have to be considered simultaneously in the design process. Fig. 3.1 illustrates how the different constraints put pressure on the topology of the rotor.

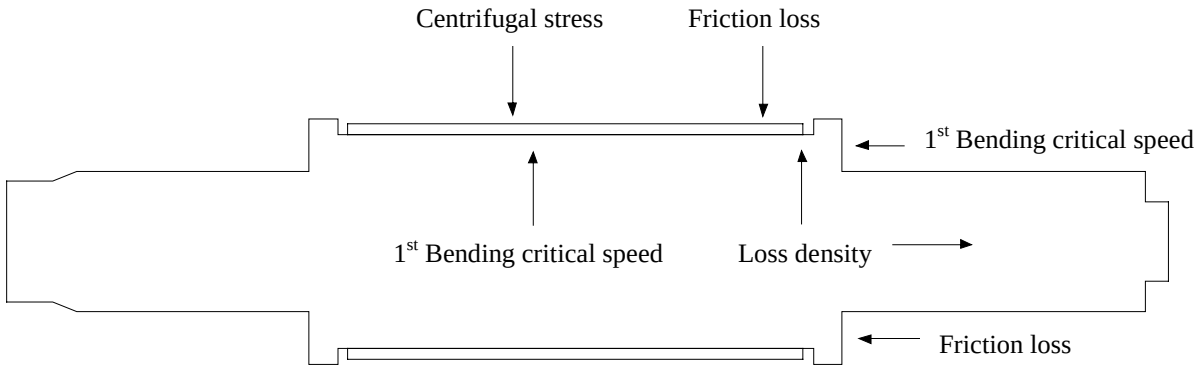

Fig. 3.1 Pressure put on the rotor designed for subcritical operation by physical constraints.

3.1.1 Centrifugal forces

Centrifugal forces arise when a rotor is rotating around its axis. The forces induce stress to rotor materials. At a particular speed, the stress reaches the level where mechanical deformations are no longer reversible. To avoid this, the rotor design has to be such that the stress is below that level in every point in the structure. Some safety margins are set, since the materials always have some inhomogeneities and irregularities. Reichert and Pasquarella (1995) present the following formulae for calculating maximum diameter D_r for rotors:

$$D_r \leq \sqrt{\frac{8\sigma_{max}}{\rho\pi^2 n^2 (3+\nu_p)}} \quad \text{for a solid rotor and} \tag{3.1}$$

$$D_r \leq \sqrt{\frac{4\sigma_{max}}{\rho\pi^2 n^2 (3+\nu_p)} - \frac{1-\nu_p}{3+\nu_p} d_r^2} \quad \text{for a laminated rotor,} \tag{3.2}$$

where σ_{max} is the maximum stress allowed, ρ is density, ν_P is Poisson's number and d_r is the inner diameter of the lamination stack. n is speed in revolutions per second. Rearranging Eq. 3.2 yields

$$v_c = \pi D_r n \leq \sqrt{\frac{4\sigma_{max}}{\rho\left[(1-\nu_p)\left(\frac{d_r}{D_r}\right)^2 + (3+\nu_p)\right]}}, \tag{3.3}$$

where v_c is the circumferential speed. Using Eq. 3.3 with parameter values set for typical laminated sheets – σ_{max} = 400 MPa, ρ = 8000 $^{kg}/_{m3}$, ν_P = 0.3 – and assuming a d_r half of D_r, maximum circumferential speed of 240 $^{m}/_{s}$ is given. Considering the fact that the lamination stack has to also

support the squirrel cage winding, an upper limit around 200 $^{m}/_{s}$ can be accepted. This result is reported by Viggiano and Schweitzer (1992) based on their own research and literature study. They also demostrate that squirrel cage rotors can tolerate higher centrifugal forces if closed slots are used instead of open slots. With closed slots, the stress is more evenly distributed inside the lamination stack.

Rearranging Eq. 3.1 with parameter values for MoCn 315 solid steel used in the high-speed rotors – σ_{max} = 590-690 MPa, ρ = 7800 $^{kg}/_{m3}$, ν_P = 0.3 –, an upper limit of around 460 $^{m}/_{s}$ can be accepted. Selecting metals with even higher values for σ_{max}, circumferential speeds up to 550 $^{m}/_{s}$ could be used (Jokinen and Arkkio 1996).

The results above indicate that solid rotors are capable of standing much higher circumferential speeds. The possibility of increasing the diameter of the rotor or the rotational speed can be capitalized as a higher power/speed ratio. Eq. 3.2 shows that the performance of a laminated rotor can be improved by decreasing the inner diameter d_r.

A modern way to calculate the stresses inside the rotor construction is to use numerical analysis, finite element modeling (FEM), for example. The effect on slotting and squirrel caging can be taken into account more accurately. Examples of use of FEM can be found from Viggiano and Schweitzer (1992), Mekhiche *et al.* (1999) and Soong *et al.* (2000).

3.1.2 Bending critical speeds of a rotor

As is the case with a musical instrument's string, there are natural frequencies that are not much attenuated by the rotor structure. Mechanical unbalance is an important source in triggering these vibrations. At a critical speed, the rotational frequency of the rotor and the unbalance coincides with the natural frequency of the rotor and the rotor starts to vibrate excessively.

The first two critical vibration modes have low frequency values and at those frequencies the rotor vibrates almost as a rigid body. These frequencies are often referred as rigid body critical speeds. These speeds are passed easily because the magnetic bearings can dampen these vibrations. Only a low frequency, low amplitude control force is required. The rest of the critical vibration modes are referred to as the bending modes. The critical speeds corresponding to these modes are not easily passed because a large amount of high frequency control force is needed.

Viggiano and Schweitzer (1992) give a rough estimate for the first bending critical speed ω_c for a laminated rotor:

$$\omega_{\mathrm{c}} = \sqrt{\left(\frac{d_{\mathrm{r}}}{D_{\mathrm{r}}}\right)^4 \frac{3ED_{\mathrm{r}}^2}{\rho l_{\mathrm{r}}^4}}, \tag{3.4}$$

where E is the Young's modulus and l_{r} is the length of the rotor. It can be seen that a short, thick rotor has higher critical speed. Eq. 3.4 shows that the performance of a laminated rotor can be improved by increasing the inner diameter d_{r}. This is contradictory to the result related to the centrifugal stresses and a trade-off between these performance characteristics must be made.

The lamination stack has a low bending stiffness, i.e., a low E if any. The squirrel cage can have some stiffening effect as will be reported in Section 3.4. Some stiffness can be achieved by mechanical stiffeners or frames but these approaches are not reported in literature considering high-speed machines. If a subcritical operation for the motor is required, the laminated rotor has to be made smaller compared to a solid rotor construction. This is because a low stiffness decreases the natural frequency values.

A mechanical unbalance in a rotor causes radial forces and vibrations when the rotor rotates around its rotational axis. It also triggers the bending vibrations near the critical speeds. As far as the unbalance is considered, a solid rotor performs better. The balance does not usually change as a function of temperature and time. The laminations tend to move around somewhat because of the centrifugal stresses and bending of the rotor, especially at high rotational speeds.

Active magnetic bearings can be used as a tool in the mechanical balancing of a rotor. This aspect is studied in detail by Lantto (1999). In the same study, unbalance compensation with active magnetic bearing control is also presented. This unbalance compensation is used in the bearing control of the high-speed machines in Chapters 4 and 5.

Lantto (1997) presents a rotordynamic model based on FEM suitable for high-speed rotating systems. The verification of the model showed a good accuracy in comparison to the measured and calculated results.

Considering the constraints of centrifugal forces and critical bending modes together, it is seen that the possible power/speed range is smaller for the laminated rotor than for the solid steel rotor (Jokinen and Arkkio 1996). This holds true if the utilization factors of both constructions are approximately the same. If a solid rotor is well designed, having a squirrel cage or a coating for a low resistivity current paths, this is a quite a safe assumption to make.

3.1.3 Rotor loss and friction loss

In addition to the mechanical constraints, the rotor design is affected by friction loss and the loss generated inside the rotor. Usually the rotor is cooled by heat convection from the rotor surface to the surrounding air and then to stator. If a certain amount of rotor loss P_r is to be transferred, the minimum limit for the rotor dimensions is approximated by the equation (Reichert and Pasquarella 1995):

$$D_r l_r \geq \frac{P_r}{\pi \alpha \Delta T}, \tag{3.5}$$

Where D_r and l_r are the diameter and length of the rotor, α is the effective heat transfer factor and ΔT is the temperature difference between the rotor and the stator. If a forced cooling system is used, α and ΔT can be defined between rotor and air in the air gap.

On the other hand, friction loss caused by the rotating surface of the rotor also depends on the rotor dimensions. The friction loss grows rapidly as a function of circumferential surface speed or a diameter of the rotor. To start with, the friction loss of a rotating rotor with radius r_r can be estimated using the following equation (Saari 1998):

$$P_f = k_f C_f \rho \pi \omega^3 r_r^4 l_r, \tag{3.6}$$

where k_f is a roughness coefficient of the rotor surface, C_f is a friction coefficient and ω is angular velocity of the rotor. From the point of view of loss, it would be better to have a long slim rotor. But this is contradictory to the result relating to critical speeds. There, a short thick rotor is preferred.

Rotor loss components are often calculated numerically with FEM. Ohmic loss, eddy-current loss and hysteresis loss components are given by a coupled solution of electromagnetic fields and circuit equations (Arkkio 1987). State-of-art software uses 3D modeling but 2D modeling is still widely used. The calculation of friction and cooling loss is often performed using analytical formulae based on experimental research. Computational Fluid Dynamics (CFD) could be used for more accurate modeling of friction and cooling loss (Shanel *et al.* 2000).

With all the loss components modeled, the temperature rise of the motor parts can be calculated. Lumped parameter thermal networks (Saari 1998) give reasonable results with little computational effort. Coolant flows can be included in the network with flow controlled temperature sources (Jokinen and Saari 1997). For more accurate modeling, a thermal FEM could be used. The thermal and electromagnetic FEM can also be coupled together (Driesen *et al.* 2000).

3.2 Solid rotors with a coating for high speed induction machines

Copper coated solid steel rotors used in this study are produced by High Speed Tech Oy Ltd. The company manufactures these for high-speed induction motors in the range of 70 to 250 kW and 50000 to 18000 $^{1}/_{\text{min}}$, respectively (Lantto 2002).

The copper layer covers the whole rotor from the end ring to the end ring, acting both as an infinite number of bars and as the end rings. It is the main circuit path of the fundamental currents. Some part of the fundamental current circulates in the solid steel part of the rotor cross section.

The idea of the construction is to have the current carrying conductors placed in such a way that the mechanical properties of the rotor are as good as possible. Strength of 100 MPa can be achieved in the bonding between a smooth copper layer and a solid steel part. For a thin copper coating this is more than adequate and the limit of centrifugal forces tolerated is not set by the bonding but by the yield strength of the solid steel part.

While prioritizing the mechanical strength, some magnetization properties are lost as a trade-off. The air gap from stator iron to rotor iron is much higher than in constructions where the copper is in bars. This causes a higher magnetization current and higher ohmic losses in the stator winding. But an increased air gap also means a decreased harmonics content of a magnetic flux seen by the rotor. The air gap surface is smooth (in Eq. 3.6, $k_{\text{f}} \approx 1$) in order to avoid excessive friction loss.

The cross section of the motor is illustrated later in Fig. 3.2 as seen by a mesh generator of the 2D finite element analysis software used for calculations. In the calculation, the copper coating is divided into bars.

3.3 Challenge of a rotor design

In conclusion, solid rotors yield better mechanical characteristics but a laminated construction generally gives better electromagnetic characteristics. It follows that a laminated rotor should be used whenever mechanically possible. This raises two questions: How can we improve the mechanical properties of laminated rotors and how can we improve the electromagnetic properties of solid rotors? Answers to these questions have been one of the main issues in the project that this study is a part of. Two solutions are proposed in the next two sections and they are compared against the commercial solution discussed in the last section. They have been reported separately in Lähteenmäki *et al.* (1999) and in Lähteenmäki and Soitu (2000). Table 3.1 contains some high-speed induction motors found in literature. They are ranked in descending order with respect to the circumferential speed. It can be seen that there are no laminated constructions found above the 200

Table 3.1 High-speed induction motors found from literature, ranked in descending order of circumferential speed v_c.

v_c [m/s] [1)]	D_r [mm] [1)]	Rotor type	Power [kW]	Speed [$^1/_{min}$]	Reference
367	70	solid coated	60	100000	Saari and Arkkio 1994
283	90	solid coated	60	60000	Lähteenmäki and Soitu 2000
236	90	solid caged	50	50000	Lähteenmäki and Soitu 2000
193	330	solid caged	2610	11160	Wood *et al.* 1997
185	118	laminated	100	30000	Viggiano and Schweitzer 1992
182[2)]	348	laminated	6000	10000	Schmied 1990
168[2)]	80	laminated	35	40000	Siegwart *et al.* 1990
144	90	solid coated laminated	65	30600	Lähteenmäki *et al.* 1999
134	51	laminated	21	50000	Soong *et al.* 2000
126	200	laminated solid caged	200	12000	Ikeda *et al.* 1990
124	99	solid solid coated solid double coated	12	24000	Pyrhönen and Kurronen 1994
63	50	solid solid double coated	0.7	24000	Sharma *et al.* 1996
62	88	solid solid slitted solid caged	12	13500	Pyrhönen and Huppunen 1996
16	198	laminated	37	1500	conventional motor

[1)] Some data not mentioned in the references; derived from other data or requested from the authors

[2)] Given in Viggiano and Schweitzer (1992)

$^m/_s$ limit. However, there are some solid rotor constructions reported under that limit. This shows that the circumferential speed is not the only constraint to consider but that other constraints may also indicate the beneficial use of a solid rotor construction.

3.4 A laminated rotor for a 65 kW 30600 $^1/_{min}$ compressor motor

As a part of the project, a new type of rotor was tested for a 65 kW 30600 $^1/_{min}$ compressor application. This laminated rotor has a thin lamination layer containing a squirrel cage. The laminated rotor was compared against the commercially used copper coated solid steel rotor

presented in Section 3.2. The idea (Patent FI 100749) and the actual design of the rotor are not part of this work. The cross sections of the motors are illustrated in Fig. 3.2. The pictures are made by a mesh generator of the 2D FEM software. In the calculations, the copper coating of the coated rotor is divided into bars.

The idea behind the design of an improved laminated rotor is to combine the mechanical strength of a solid rotor with the electromagnetic performance of a laminated rotor. The rotor is partly laminated so that a squirrel cage can be fitted within the lamination whilst there is still enough room for the magnetic flux to go around the bars.

26 round cage bars were installed in the holes in the lamination stack, i.e., the rotor has closed slots. The ratio d_r/D_r was 0.66. Thickness of the laminated sheets was 0.35 mm. Emphasis was put on manufacturing the combined lamination and cage system so that it would have some mechanical stiffness. The electromagnetic characteristics are close to the ones of an ordinary squirrel cage rotor with closed slots. A part of the fundamental current circulates in the solid part of the rotor cross section. When the conductivity of the solid material is good, it acts as an extra bar. The lamination confines the harmonic components of the flux and only a small amount of loss is induced in the solid part. The amount of copper in the rotor cross section was the same in both of the rotors, but there was 27 per cent less copper at the end rings of the laminated rotor.

In the application, the circumferential surface speed of the rotors was 144 $^{m}/_{s}$ at the nominal speed. Hence, the centrifugal stress was not a problem. The problem comes from the bending critical speeds. The compressor wheel and the cooling fan at the other end of the shaft bring the bending critical speeds downwards.

In the application, active magnetic bearings are used. In general, magnetic bearings are not very stiff and this influences the critical speed problem. As is mentioned in Section 3.1.2, the rigid body

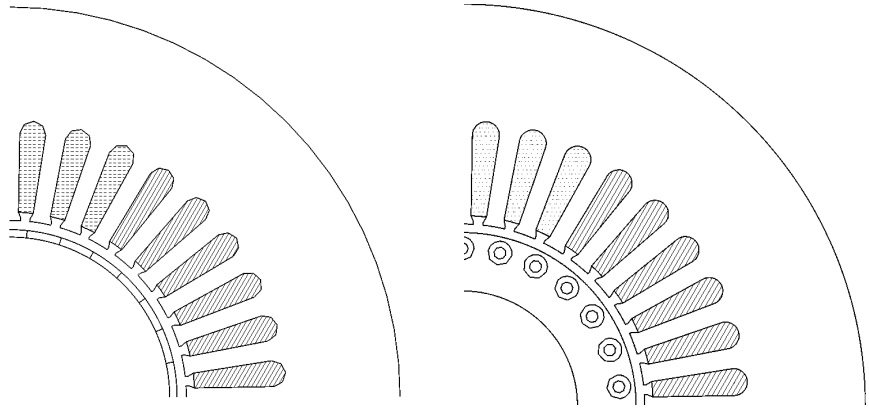

Fig. 3.2 Cross sections of the copper coated solid steel and laminated rotors.

critical speeds are passed relatively easily because the magnetic bearings can dampen these vibrations. Only a low frequency, low amplitude control force is required. The critical speeds corresponding to the bending modes are not easily passed because a large amount of high frequency control force is needed. For this reason, the high-speed applications usually operate under the first bending critical speed.

Considering the bending critical speeds, the important parameter is the material elasticity. As shown in Eq. 3.4, the rigidity of the rotor depends on the elasticity and the density of the materials, together with the geometry. The Young's moduli E for the steel used and for copper are 210 GPa and 120 GPa, respectively. The bending rigidity of the lamination stack is very low compared to these. In calculations, a good approximation for the lamination stiffness is $E = 0$. For this reason, the height of the lamination stack has to be kept small. This applies to all the laminations of the rotor, the electric machine lamination and the possible laminations of the magnetic bearings and position sensors.

The free-free natural frequencies of the two rotors were measured using an acceleration sensor with 102.4 μs sampling. The sensor was fastened to a rotor. The rotors were suspended on a non-stiff low-attenuating media in order not to distort the modes and the frequency values. An impulse was given and the vibration amplitude was recorded with the acceleration sensor. Different suspension methods, impulses and sensor positions were tested. All the tests gave the same results. Fig. 3.3 shows a picture of the measurement process. From the sensor data recorded, the vibration spectrum was calculated. Fig. 3.4 shows the sensor output in time domain and the corresponding fast Fourier transformation spectrum for the laminated rotor system including the compressor and cooling propellers. The spectrum has clear peaks for the two free-free natural frequencies.

The rotors were measured with and without the compressor and cooling propellers. A rotordynamic FEM software based on work of Lantto (1997) was used to calculate the free-free natural frequencies.

Table 3.2 shows the measured and calculated results for the first two bending modes. The measured result for the laminated rotor system, 530 Hz, indicated that the 510 Hz nominal operating speed was very near the first bending critical speed. The ratio of the nominal speed and the critical speed is 0.96. Viggiano and Schweitzer (1992) presented ratios of 0.6, 0.93 and 0.94 for three different cases. In the real operation, the natural frequencies increase somewhat as a function of a rotational speed. Hence, in reality the margin is a bit larger than 0.96. The solid steel rotor had much higher critical speeds and higher nominal speeds could have been used in this respect.

Fig. 3.3 Measurement of the bending critical speeds of the laminated rotor. On the right, an acceleration sensor is attached. The rotor lies on an air bubble matrix.

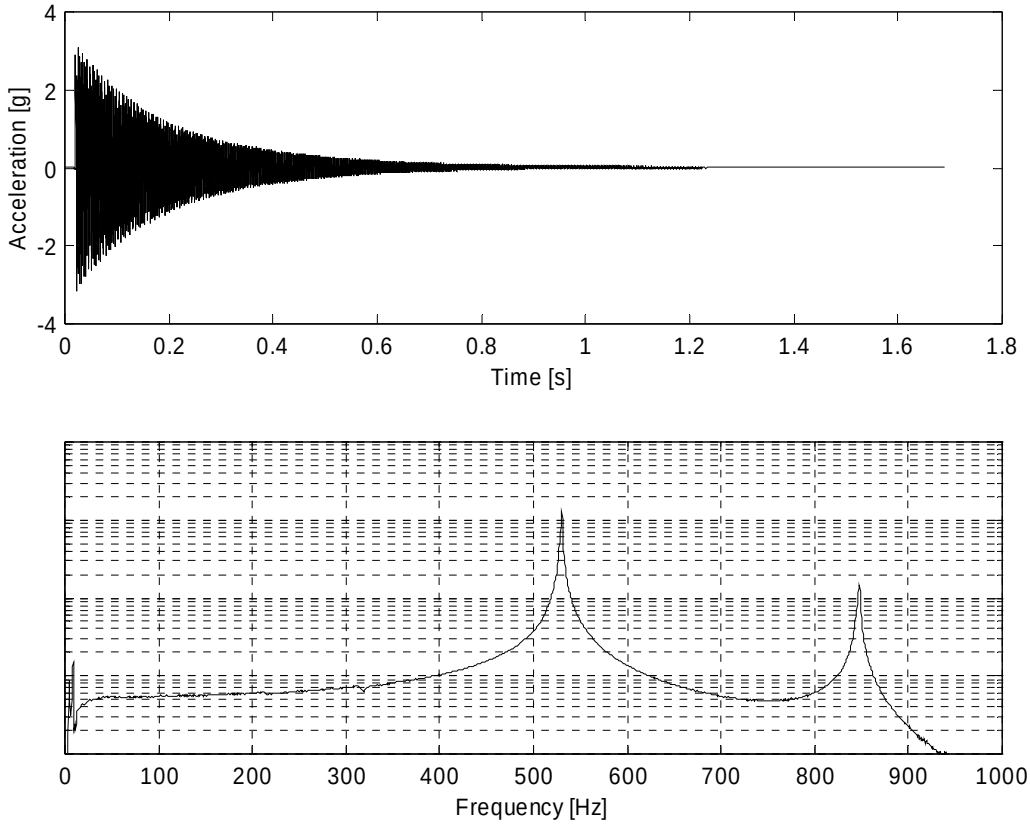

Fig. 3.4 The output signal from the acceleration sensor and the corresponding spectrum.

Table 3.2 The free-free natural frequencies (FFNF) measured and calculated.

	Measured FFNF [Hz]		Calculated FFNF [Hz]	
	1st zero speed	2nd zero speed	1st zero speed	2nd zero speed
Solid rotor	1040	2270	1040	2282
Solid rotor system	828	1520	837	1527
Laminated rotor	678	1495	526 – 678[1)] – 998	1391 – 1657[1)] – 2122
Laminated rotor system	530	847	457 – 530[2)] – 788	1164 – 1258[2)] – 1528

Solid steel: E = 210 GPa, ρ = 7800 $^{kg}/_{m3}$, ν_P = 0.3

Copper: E = 120 GPa, ρ = 8930 $^{kg}/_{m3}$, ν_P = 0.33

Lamination: E = 0 GPa, ρ = 7600 $^{kg}/_{m3}$, ν_P = 0.3

Compressor wheel: E = 0 GPa, ρ = 2630 $^{kg}/_{m3}$, ν_P = 0.33

[1)] 1st FFNF fitted $\Rightarrow$ E = 40 GPa for lamination stack and squirrel cage combined. FFNF values: 0 – 40 – 210 GPa

[2)] 1st FFNF fitted $\Rightarrow$ E = 22 GPa for lamination stack and squirrel cage combined. FFNF values: 0 – 22 – 210 GPa

As Table 3.2 shows, the measured and calculated results for the solid steel rotors were almost the same. Based on this, the effective stiffness of the combined lamination and cage was approximated. The stiffness was set as a free parameter and it was adjusted so that the first natural frequency matched the measured result. A comparison of the measured and calculated results indicates that there is some stiffness achieved by a careful manufacture. However, the calculated stiffness was different in the cases of a rotor alone or the rotor with the compressor and cooling propellers. This would indicate that the stiffness of the combined lamination stack and the squirrel cage is not constant. In this case, the error in the estimation of the second natural frequency raised doubts about correct modeling.

The laminated rotor was then compared against the commercially used solid steel rotor with a copper coating. The stator was the same and only the rotors were changed during the comparison. As the effective air gap for the laminated rotor was only 48 % of the air gap for the solid steel rotor, a lower stator current and a better power factor was expected. The actual compressor was used as a load machine. The results of the comparison are presented in Chapter 4.

3.5 Solid rotors with a squirrel cage for a 60 kW 60000 $^{1}/_{min}$ motor

As a part of the project, a new type of rotor was tested for a 60 kW 60000 $^{1}/_{min}$ motor. The rotor has a squirrel cage mounted at the surface of the solid steel rotor. Two such rotors were made. One rotor has 16 bars and the other 26 bars. The rotors were compared against the commercially used copper coated solid steel rotor presented in Section 3.2. The actual design of the rotors are not part of this work. The cross sections of the motors are illustrated in Fig. 3.5.

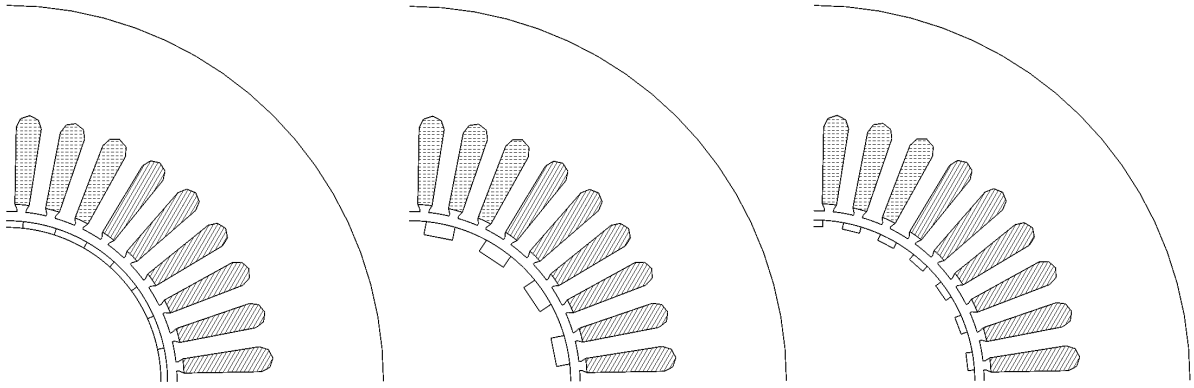

Fig. 3.5 Cross sections of the copper coated and the squirrel cage solid steel rotors.

The idea behind the design of the squirrel cage solid steel rotors is to combine the mechanical strength of a solid rotor and the electromagnetic performance of a squirrel cage rotor. A drilling of slots to the solid steel was considered difficult so the squirrel cage was constructed at the surface of the rotors, i.e., the rotors had open slots. The down side of the open slot design is the permeance harmonics and additional loss in the stator teeth. A minor advantage is a lower leakage inductance of a rotor bar.

Mounting of copper as bars is more difficult than the making of a coating, however. A good contact between steel and copper is hard to achieve, especially at the sharp corners of the slots. As a consequence of the problem, the shape of the slot and the amount of the copper are limited. Deep bars are denied and increasing the number of bars will decrease the total amount of copper. This is a problem since a fair number of deep bars would be likely to produce an electromagnetically optimal construction. This problem can be seen also in Fig. 3.5, where a 26 bar rotor could only have 60 % of the copper compared to that in the other rotors. The amount of copper was even further reduced because of a bit of careless machine tooling. This reduction of copper had an unfortunate effect on motor performance, as can be seen later on.

The methods used to measure and to calculate the bending critical speeds are the same as for the other case presented in the previous section. Mechanical characteristics of the squirrel cage solid steel rotors are almost identical to the copper coated rotor. The bending stiffness is about the same, as is seen from Table 3.3. Fig 3.6 shows the output of the calculation software. The mode shapes of the first two free-free natural frequencies are plotted together with the rotor geometry for the coated rotor.

The picture shows how the bending modes split into a forward and backward mode. The frequency of the forward mode is a bit higher than that of the zero speed mode. The forward mode rotates in

Table 3.3 The free-free natural frequencies (FFNF) measured and calculated.

	Measured FFNF [Hz]		Calculated FFNF [Hz]	
	1st zero speed	2nd zero speed	1st zero speed	2nd zero speed
Coated solid rotor	1887	3019	1919	3006
16 bars solid rotor	1898	3038	1907	3014
26 bars solid rotor	1917	3090	1923	3023
Solid steel:	E = 210 GPa, ρ = 7800 $^{kg}/_{m3}$, ν_P = 0.3			
Copper:	E = 120 GPa, ρ = 8930 $^{kg}/_{m3}$, ν_P = 0.33			
Lamination:	E = 0 GPa, ρ = 7600 $^{kg}/_{m3}$, ν_P = 0.3			

the same direction as the rotor and the rotor unbalance. As the unbalance is the main excitation source of the vibrations, backward modes can be ignored. In case of the copper coated rotor, the actual 1st bending critical speed calculated is then 2031 Hz compared to the zero speed free-free natural frequency of 1919 Hz.

Because the squirrel cage type construction had not been tested before, some precautions were made to avoid any mechanical breakdowns. A mechanical integrity at 50000 $^{1}/_{min}$ with an operation temperature of 150 °C was confirmed. Thus, the comparisons were made at 835 Hz or 50100 $^{1}/_{min}$ supply frequency, not at the rated speed of 60000 $^{1}/_{min}$. The reduced speed corresponds to the circumferential speed of 235 $^{m}/_{s}$ instead of the rated speed of 283 $^{m}/_{s}$. In both cases the circumferential speed is still above the 200 $^{m}/_{s}$ limit considered safe for the laminated rotors. The maximum load at the new operation point was adjusted according to the temperature rises of the stator and rotors.

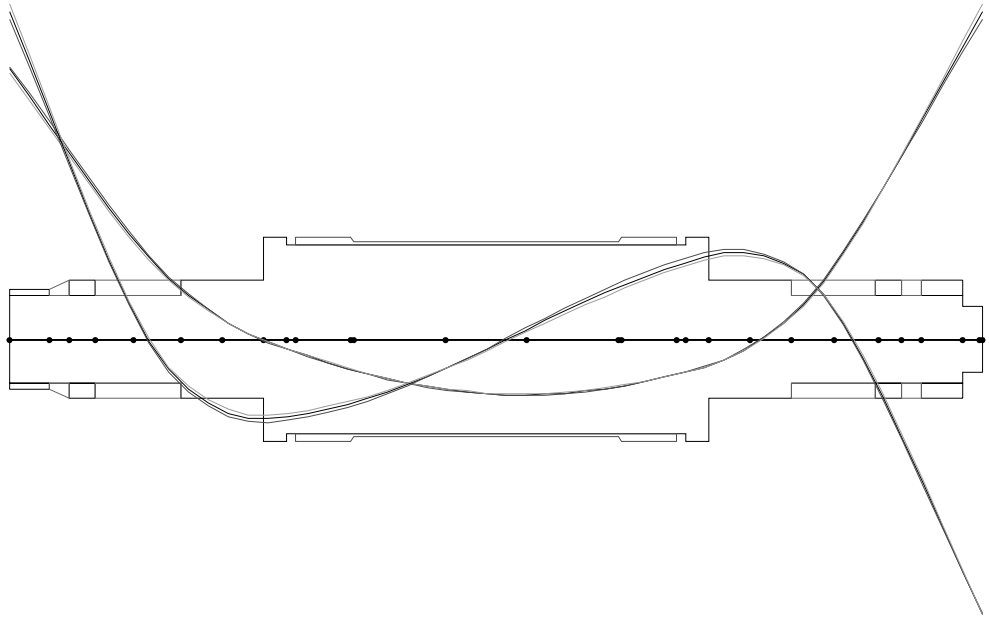

Fig 3.6 The mode shapes of the first two free-free natural frequencies.

In comparison of the rotors, the stator was the same and only the rotors were changed. The loading of the motors was done using a procedure known as the back-to-back test. Two machines were coupled together, one running as a motor and the other as a generator. The DC-links of the inverters were connected so that the power circulated through the machines and inverters. Only the losses were taken from the electric network. The load was varied by running the motor with a higher supply frequency than the generator. Thus, the slip and the load of the machines were determined by the frequency difference of the inverter outputs.

Electromagnetic characteristics of the squirrel cage solid steel rotors are closer to a laminated squirrel cage rotor. The air gap from iron to iron is about the same as that of a laminated high-speed construction. As the iron-to-iron air gap for the squirrel cage rotors was only 56 % of the air gap for the coated rotor, a lower stator current and a better power factor was expected. The results of the comparison are presented in Chapter 5.

Fig 3.7 The copper coated solid steel rotors for the 65 kW 30600 $^{1}/_{min}$ compressor motor on the right and for the 60 kW 60000 $^{1}/_{min}$ motor on the left.

4 COMPARISON OF ROTORS FOR 65 KW 30600 $^{1}/_{MIN}$ COMPRESSOR DRIVE

In this chapter, a copper coated solid steel rotor and a laminated rotor are compared. These rotors were introduced in Sections 3.2 and 3.4. The laminated rotor was designed to combine the mechanical properties of a solid steel rotor and the electromagnetic properties of a laminated squirrel cage rotor. The comparison was made for a 65 kW 30600 $^{1}/_{min}$ compressor motor. The compressor and the induction motor are integrated so that the compressor wheel and the rotor of the induction motor are on the same shaft. The compressor and the rotors tested are shown in Fig. 4.1.

4.1 Measurement setup

The comparison was made using the same three-phase stator for both rotors. The motor was fed from VACON CX 90 (90 kW, 210 A) voltage source inverter (VSI). The load was adjusted using an airflow measurement orifice. The orifice is a chamber with several small air holes leading to it. It is mounted at the inlet of the compressor. By closing a certain number of air inlets, the pressure drop across the compressor and the airflow volume can be adjusted. This loading method only yields quite a discrete set of measurement points because the number of holes was limited to 20 and the operation region of the compressor included only a part of the adjustment range available. The no-load measurements were done without the compressor wheel.

Power	65 kW
Voltage	400 V
Current	150 A
Supply	VSI
Speed	30600 $^{1}/_{min}$
Stator winding	3 phase, full pitch
Stator connection	DD
Stator slots	36
Poles	2
Insulation class	F
Cooling	Forced air cooling
Bearings	AMB
Load	Air compressor

Fig. 4.1 A photograph and data of the 65 kW 30600 $^{1}/_{min}$ high-speed compressor. On the left, a copper coated solid steel rotor and on the right a laminated rotor.

The compressor drive has an active magnetic bearing system. It includes the actual bearing magnets, power electronics and control electronics. An unbalance compensator mentioned in Section 3.1.2 is a part of the control electronics. Loss measurement for the AMB system was made during the other comparison presented in the next chapter.

Fig. 4.2 shows a schematic diagram of the measurement setup. The input current, voltage and power were measured with a Norma 6000-series power analyzer. Shunts were used in the measurement of currents. The DC link voltage, the current and voltage in the DC resistance measurement were measured with Fluke multimeters. The reading of one PT100 thermoelement in stator winding was also stored. The accurate speed information of the rotor was given by a rpm sensor of the magnetic bearing system. The rpm sensor is a commercial product based on Hall sensors.

The average temperature of the winding was measured using DC resistance measurement. The measurement was conducted so that at the end of a load test, the inverter was disconnected from the motor mains and the DC supply was connected immediately after. The resistance was measured for two minutes while the rotor was coasting down. In this way, an accurate value of the temperature was obtained with only a marginal interpolation to the instant of the disconnection. Fig. 4.3 shows an example of a measurement result. Some measured data points are taken away between 40 and 60 seconds. There, the DC measurement was distorted by low frequency AC signals induced by the stopping rotor. As can be seen from the figure, the temperature drops rapidly. Thus, the measurement is best done instantaneously and not after waiting for the rotor to stop.

The shaft power of the compressor and induction motor could not be measured. Hence, absolute values for efficiency could not be calculated. However, the comparison of the rotors could be performed using relative values and other indicators for losses and performance.

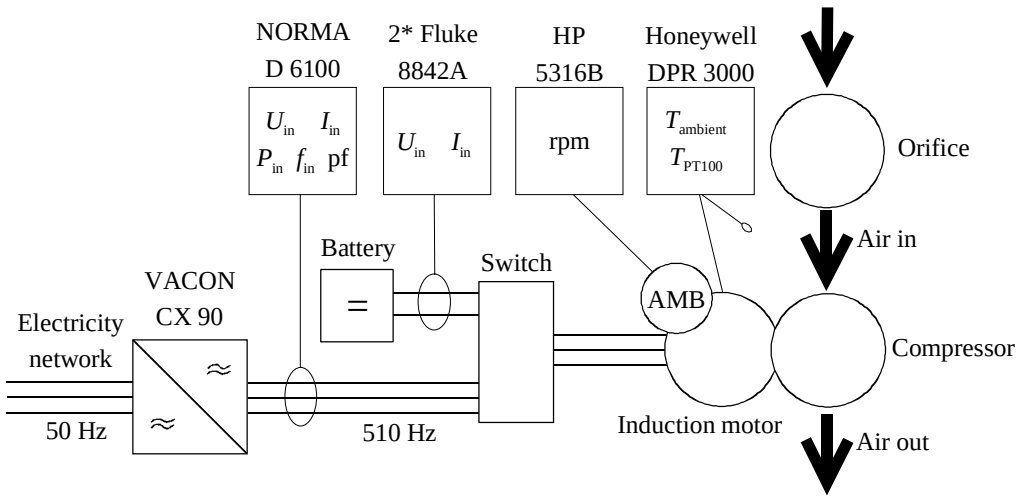

Fig 4.2 Schematic diagram of the measurement setup. NORMA uses three-watt meter method. Current is measured with shunts.

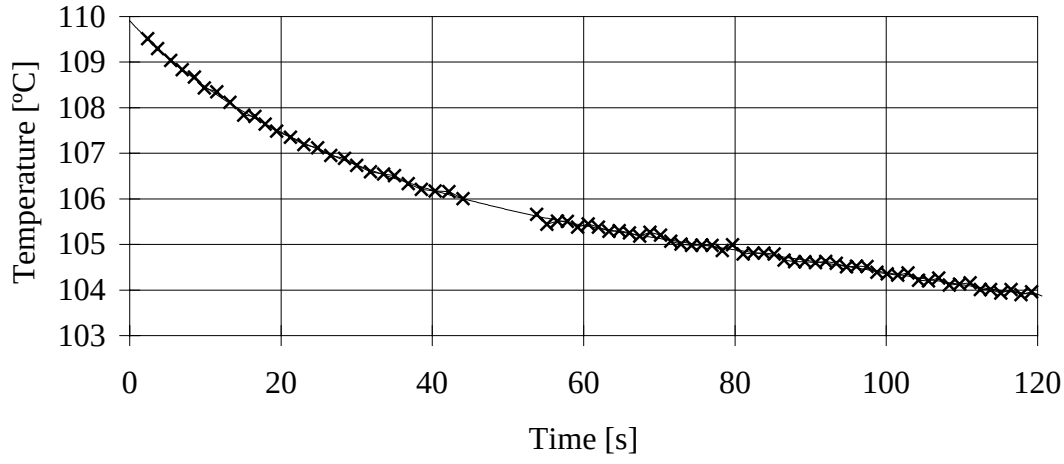

Fig 4.3 The result of an average temperature measurement for the stator winding.

4.2 Comparison and results

Three characteristics were chosen as a basis for a comparison: The input current, the temperature rise of the stator and the slip. Because the shaft power was not known, the comparisons were made as a function of the input power. Operation characteristics of the motor were measured at different supply frequencies, magnetization levels and loads. The comparison gave quite similar results in every case. Thus, only the measurements done for nominal speed and magnetization are presented.

4.2.1 Temperature rise in the stator winding

The temperature rise of the stator winding was identified as one of the characteristics to be compared. A lower temperature rise in the stator winding indicates lower losses, at least at the stator side of the motor. Also, a lower temperature makes it possible to increase the utilization of the motor, i.e., to get more power out from the same motor size. This argument is based on the assumption that the temperature rise of the rotor is not a problem with either of the rotors.

For each load point, the average temperature of the stator winding was measured after the temperatures of the motor had reached a steady state. This was followed by thermocouples and the PT100 thermoelement. Ambient temperature was measured with mercury thermometer.

The average temperature rise of the stator winding is plotted in Fig. 4.4. There is a major difference between the two rotors. At the input power of 65 kW the temperature rise with the copper coated rotor is 97 K. At the same input power, the temperature rise with the laminated rotor is only 84 K. In order to meet the requirements for insulation class B (IEC Standard 34-1 1994), 62 kW can be fed into the motor with a laminated rotor. Comparing input powers at the temperature rise of 80 K, the laminated rotor would give 39 % increase in the utilization factor for class B.

4.2.2 Input current

A lower input current indicates lower magnetization current and better efficiency at partial loads. A smaller frequency converter could be selected in some cases. Because the resistive loss in the stator winding is the main loss component to determine the temperature rise in the winding, the input current and the temperature rise are assumed to go hand in hand.

This can be seen in Fig. 4.5, which shows that the input current of the laminated rotor is 11 per cent lower at the input power of 65 kW. The difference is over 50 per cent at no-load. Thus, the laminated rotor is superior to the copper coated rotor in this respect. This is mainly due to a smaller air gap in the case of the laminated rotor as stated in Section 3.4.

4.2.3 Slip of the rotor

The slip of the rotor was chosen as a third characteristic for the comparison. The slip s does not relate to the total loss of the rotor but it gives the minimum load loss P_{tl} needed to produce the electromechanical power P_{m} from the airgap power P_{δ}. The operation principle of an induction machine dictates that the loss related to the torque producing components of power is the air gap power times the slip:

$$P_{\mathrm{m}} = P_{\delta}\left(\frac{\Omega_{\mathrm{m}}}{\Omega_{\mathrm{s}}}\right) = P_{\delta}\left(\frac{(1-s)\Omega_{\mathrm{s}}}{\Omega_{\mathrm{s}}}\right) = P_{\delta} - sP_{\delta} = P_{\delta} - P_{\mathrm{tl}}\,, \tag{4.1}$$

where Ω_{m} and Ω_{s} are the mechanical and synchronous speeds of the rotor. P_{tl} is a resistive loss mainly generated in the copper coating or in the squirrel cage. The slip depends on the impedance of the rotor. The smaller the impedance or resistance, the smaller the slip and the load loss P_{tl}:

$$s = \frac{P_{\mathrm{tl}}}{P_{\delta}} \propto \frac{R_{\mathrm{r}} I_{\mathrm{r}}^2}{P_{\delta}} \tag{4.2}$$

Fig. 4.6 shows that the comparison of slip goes against the laminated rotor. At the input power of 65 kW, the slip of the laminated rotor is 52 % higher than the slip of the copper coated rotor. The rotor current in the laminated rotor seems to face a higher resistance. The amount of copper in the rotor cross section was the same in both of the rotors, but there was 27 per cent less copper at the end rings of the laminated rotor.

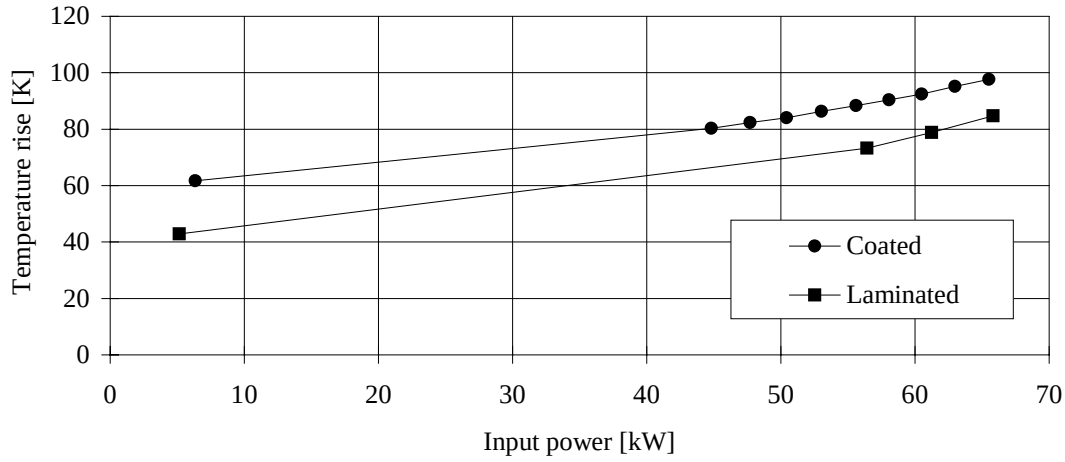

Fig. 4.4 Comparison of the measured average temperature rises in the stator windings.

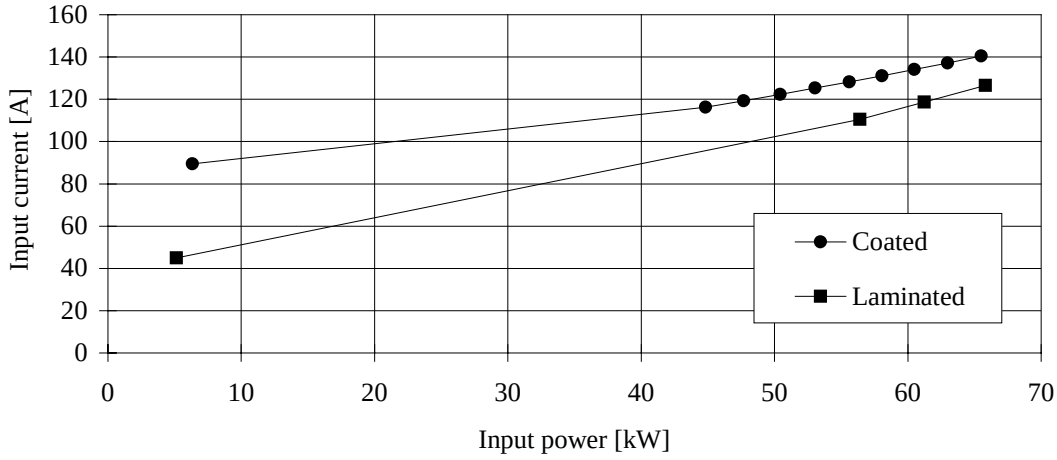

Fig. 4.5 Comparison of the measured input currents.

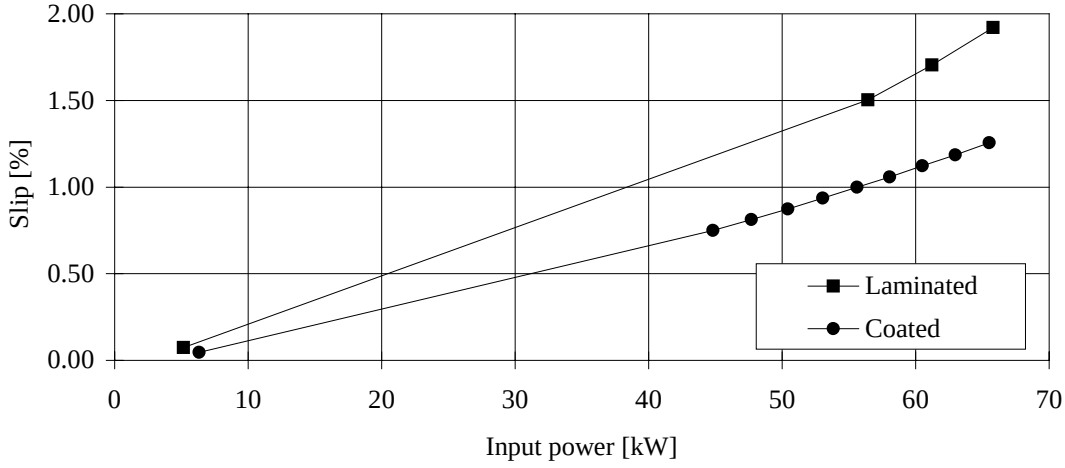

Fig. 4.6 Comparison of the measured slips.

Because of the lamination, the iron part of the laminated rotor is not utilized by the fundamental current. This increases the current density in the squirrel cage compared to the coating. A higher slip and loss indicates a higher temperature rise. A higher temperature rise further increases the resistance and the slip. Assuming that the air gap power per input power is about the same for both rotors, the above result would indicate that the laminated rotor has about 40 % more loss. This is so mainly for the fundamental component of power producing the torque. On the other hand, the harmonic loss at the surface of the copper coating and in solid iron can be considerable. Thus, the total efficiencies of the rotors are difficult to compare.

4.2.4 About the mechanical robustness

The copper-coated solid steel rotor had already proven to be a very robust construction. The robustness of the laminated rotor was then to be tested. After about 100 hours of testing and several thermal cycles there were no visible signs of detoriation. The combined lamination and squirrel cage system gave no sign of decreasing stiffness. As mentioned in Section 3.4, the 510 Hz operation frequency was close to the 1st bending critical speed. The decreasing stiffness would have led to a passing of the critical speed. This can be seen from the data in Table 3.2. The AMB system would have prevented that from happening with an alarm signal and an automatic run-down of the motor.

4.3 Conclusion

Two different rotor constructions for a high-speed induction motor were tested for a compressor application. In the application considered, the limiting characteristic for the use of a laminated rotor was the 1st bending critical speed of the rotor. In Section 3.4, the stiffness of the combined lamination stack and the squirrel cage was calculated to be 22 – 40 GPa. The measurements proved that the laminated construction has some stiffness and that the calculated result is reasonable.

The results of the measurements were in favor of the laminated rotor construction. The laminated rotor construction yields lower temperature rise for a stator, smaller input current and better power factor. The average temperature rise in the stator winding was more than 13 per cent lower throughout the measured operation region of the compressor. The input current was more than 10 per cent lower. Considering the utilization of the motor, 39 % more power could be taken out from the laminated rotor for insulation class B.

However, the laminated rotor operated at higher slip. This can indicate higher loss and temperature rise in the rotor. As the shaft power could not be measured, it is difficult to conclude anything concerning the total efficiency of the induction motor with the two different rotors. To further

improve the laminated design, more copper should be put into the squirrel cage, especially at the end rings.

Mechanical considerations properly addressed, the laminated rotor type presented here can be used in a high-speed compressor drive instead of a copper coated rotor. If the rotor is well designed, the induction motor can have significantly better operating characteristics than with a coated rotor.

5 COMPARISON OF ROTORS FOR 60 KW 60000 $^{1}/_{MIN}$ HIGH-SPEED MOTOR

In this chapter, a copper coated solid steel rotor and two solid steel squirrel cage rotors are compared. The rotors were introduced in Sections 3.2 and 3.5. The solid steel squirrel cage rotors were designed to combine the mechanical properties of a solid steel rotor and the electromagnetic properties of a squirrel cage rotor. The comparison was made for a 60 kW 60000 $^{1}/_{min}$ motor. The tests were done having two identical motors coupled 'back-to-back' with a flexible coupler. The back-to-back test setup and the rotors tested are shown in Fig. 5.1.

During the measurements, there was a specific opportunity to measure the rotor surface temperature on-line. The temperature was measured with an infrared camera via the cooling duct dividing the stator stack. Only the exhaust pipe of the cooling air had to be removed. This is done to the motor on the right in Fig. 5.1. The figure also shows a stripe of paint at the surface of the rotors, painted for the temperature measurement purposes.

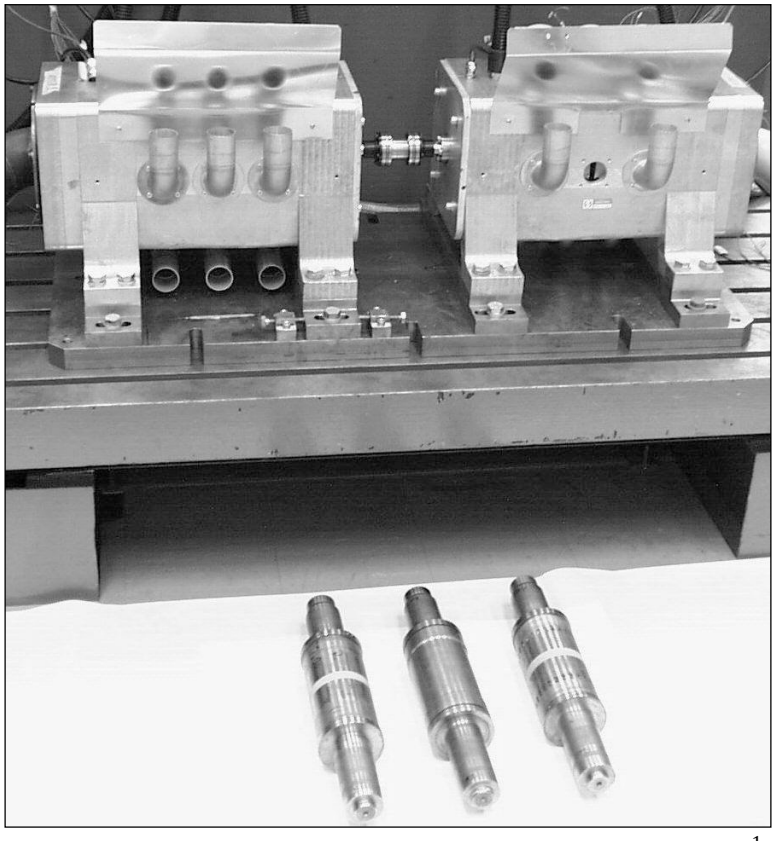

Power	60 kW
Voltage	400 V
Supply	VSI
Speed	60000 $^{1}/_{min}$
Stator winding	3 phase, full pitch
Stator connection	YY
Stator slots	36
Parallel paths	2
Poles	2
Insulation class	F
Cooling	Forced air cooling
Bearings	AMB
Load	Back-to-back

Fig. 5.1 A photograph and data of the 60 kW 60000 $^{1}/_{min}$ high-speed motors coupled with a flexible coupler. From left to right, 16 bar, coated and 26 bar rotors.

The copper coated solid steel rotor is similar to the rotor used for the 65 kW compressor drive presented in the previous chapter. The circumferential speed at 60000 $^{1}/_{min}$ is 280 $^{m}/_{s}$. As mentioned in Section 3.5, a maximum speed of 50000 $^{1}/_{min}$ was specified for the squirrel cage rotors. Thus, the comparison was made at 50100 $^{1}/_{min}$, the circumferential speed being 235 $^{m}/_{s}$. Even at this speed, the use of a laminated squirrel cage rotor is not possible. Reasons for this were discussed in Chapter 3.

5.1 Measurement setup

In the comparison, two similar high-speed motors were used. The motors were coupled and the other motor worked as a motor tested and the other as a load machine, i.e., a generator. Both machines were connected to a VACON CX 90 (90 kW, 210 A) VSI supply. The DC-links of the frequency converters were connected together. With this kind of a set-up, only the power loss was taken from the grid. The set-up was kept the same and only the rotors were changed during the comparison. Fig. 5.2 shows a schematic diagram of the measurement setup.

The AMB system was fed separately via UPS so that in an event of electricity blackout the bearing system would have stayed operational. This arrangement was done only for research purposes as in real applications the bearing system gets its power from the DC-link of the inverter. With this set-up the total power consumption of the bearing system could be measured. A set of measurement points was taken at zero speed and up to 835 Hz. The level of loading did not have any effect on the power

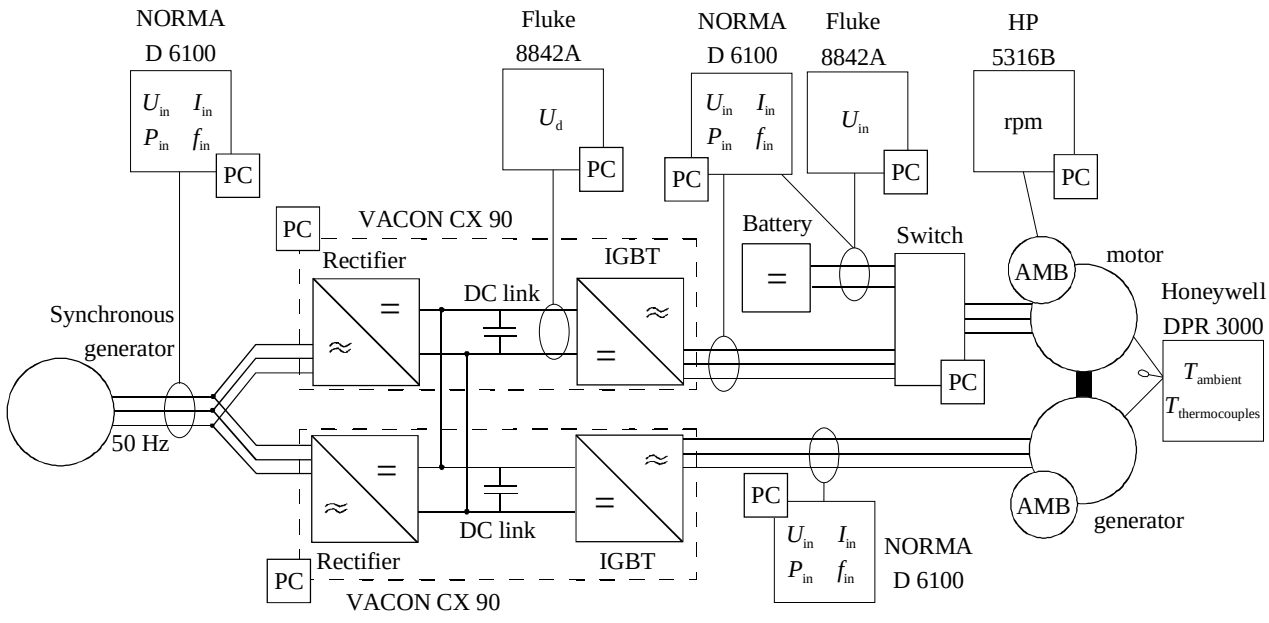

Fig. 5.2 Schematic diagram of the measurement setup. NORMAs use three-watt meter method. Currents are measured with shunts. Setup is controlled with a PC, using IEEE 488 bus.

loss. The unbalance compensator was set to start at 280 Hz. From Fig. 5.3 it can be seen that the compensator reduces the loss when turned on.

Although not visible from the figure, the control voltage and current amplitudes of the bearing magnets drop significantly. This result was presented by Lantto (1999). The AMB system provides the rotational frequency information of the motors.

Cooling of the motors was arranged by using external cooling compressors. This was done only for experimental purposes. In a commercial application, there is a cooling fan attached to the other end of the motor shaft. The cooling air is blown into the end winding regions via axial ducts in the frame. The flow of air circulates the end winding space and also comes out from the cooling duct dividing the stator stack. The cooling flow arrangement is shown in Fig. B1 in Appendix B.

The load was adjusted by reducing the supply frequency of the load generator. The rotational frequency of the coupled shaft system was in between the two supply frequencies. Thus the motor had a positive slip and the generator a negative slip value. In this way, the adjustment of the load was easy compared to using an actual load machine, as in the previous chapter.

Electric characteristics were measured using NORMA 6000-series power analyzers. One NORMA was connected to the mains of the motor and another to the mains of the generator. A third NORMA was connected to the supply of the VSI units. The difference in power readings of the motor and the generator showed directly how much power was lost in the two machines. From the readings of the third NORMA, the total power loss of the drive units could be documented, excluding the AMB loss and the cooling loss. The power analyzers also provided a Fourier analysis for the current, voltage and power. Harmonic components up to the order of 40 were measured. The sampling was synchronized to the fundamental of the voltage, using external low pass filters.

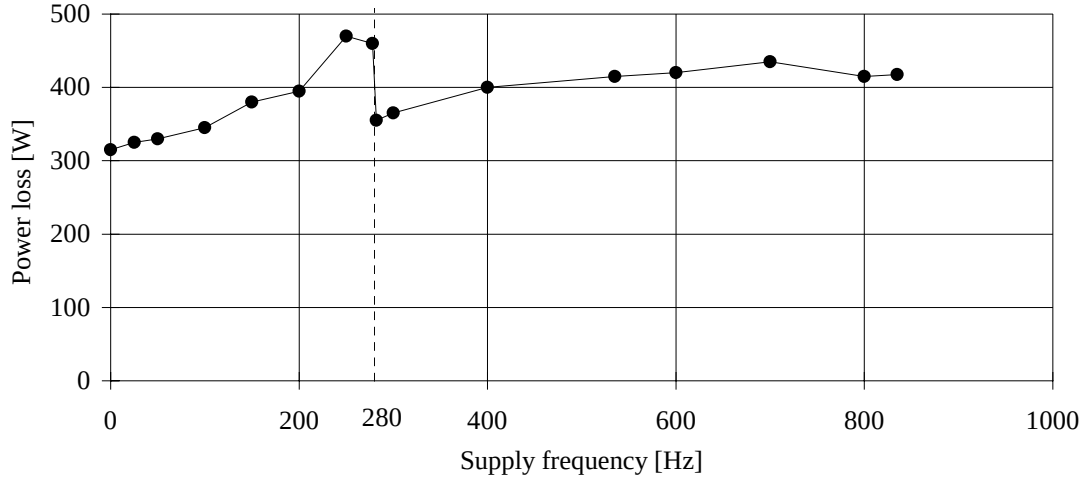

Fig. 5.3 Power loss of the active magnetic bearing system of the motor as a function of speed.

As reported in Lähteenmäki *et al.* (1999), one problem of checking the calculations against measurements is that there is no information on the temperature of the rotor. In this case however, the temperature could be measured. The stators of the high-speed machines had a cooling channel dividing the stator core into two parts. The frame and the cooling flow outlets were manufactured so that it was possible to see the surface of the rotor via the cooling channel. This made it possible to use an INFRAMETRICS 600 IR infrared camera to record the surface temperature of a rotor online. The radiometer had a liquid nitrogen cooled detector measuring the heat radiation coming from the rotors. The optics of this infrared camera were sufficient to zoom only on the surface of the rotor.

The rotors were painted at the point of the cooling duct in order to have the emittance of the rotor surface close to unity. This made the calibration of the measurement easier. Since the emittance of the paint was not exactly unity, there was some error in the results. A calibration of the measurement system showed that the readings were 2 - 3 K lower than the real temperature. However, this standard error does not affect the comparison of the different rotors. According to the specifications, the noise level of the imaging radiometer is negligible. This method of measuring the temperature of the rotor was considered very useful.

5.2 Comparison and results

The operation characteristics of the motor were measured at nominal and reduced magnetization levels. The comparison gave quite similar results in both cases. Thus, mainly the results of the 835 Hz measurements with the nominal magnetization are presented. The waveform of the supply voltage had one pulse per half cycle, i.e., a pulse amplitude modulation (PAM) was used. A synchronous generator was used as an electricity network in order to adjust PAM voltage. This was illustrated in Fig. 5.2.

The measured characteristics were input power, input current, power factor, slip and temperature rises of the stator winding and rotor surface. The average temperature of the stator winding was measured using the DC-resistance measurement explained in the previous chapter.

Efficiency could not be derived accurately because shaft power could only be indirectly derived from other measurements. For this reason, most comparison results are shown as a function of the input power of the motor tested.

Before continuing, it is emphasized that during the measurements only one 26 bar rotor was available. In the generator machine, the 16 bar rotor was used during the measurements. The results of the power loss measurements for the 26 bar rotor must be reviewed accordingly.

5.2.1 Temperature rise in the stator winding

The temperature rise of the stator winding is considered first. Lower temperature rise in the stator winding indicates smaller loss, at least at the stator side of the motor. Also, a lower temperature rise makes it possible to increase the utilization of the motor, i.e., to get more power out from the same motor size. This argument is based on the assumption that the temperature rise of the rotor is not a problem.

Fig. 5.4 shows the temperature rise of the winding with different rotors as a function of the input power. At 835 Hz, the input power of 50 kW corresponds approximately to the nominal torque and power. It can be seen that the temperature rise of the copper coated rotor is 5 per cent higher than that of the 16 bar rotor. The difference is about 8 % at no-load.

From the Figure, it can be seen that the temperature curve for the 26 bar rotor ends at around 47 kW. This is because the temperature rise of a rotor surface became a limiting factor for the loading of the motor. As mentioned in Section 3.5, the maximum allowed temperature for the squirrel cage rotors was 150 °C. At no-load, the temperature rise of the stator winding for the 26 bar rotor was similar to that of the 16 bar rotor. When loaded, the temperature rise approached the values recorded with the copper coated rotor. The difference in results of the different rotors is much smaller than in the previous case for the laminated and solid steel rotor.

5.2.2 Input current and power factor

The input current of a motor was chosen to be another characteristic to be compared. A lower input current and a better power factor mean that a smaller frequency converter could be selected in some cases. Fig. 5.5 shows that compared to the 16 bar rotor, the input current of the copper coated rotor is 10 per cent higher at 50 kW input power. The difference is over 30 per cent at no-load. Figs. 5.3 and 5.4 indicate that the squirrel cage rotor with 16 bars is somewhat better than the copper coated rotor in the way that it can be more heavily loaded in this respect. The effect of the large airgap for the copper coated rotor is the main reason for this comparison result.

Fig. 5.6 shows the difference in power factors for the different rotors. The values are quite low for all the rotors. This is due to the relatively large air gap, which is common to high-speed induction machines, as shown in Section 2.3. The iron-to-iron airgap for the copper coated rotor is 80 % larger than for the others. This is clearly seen in the results.

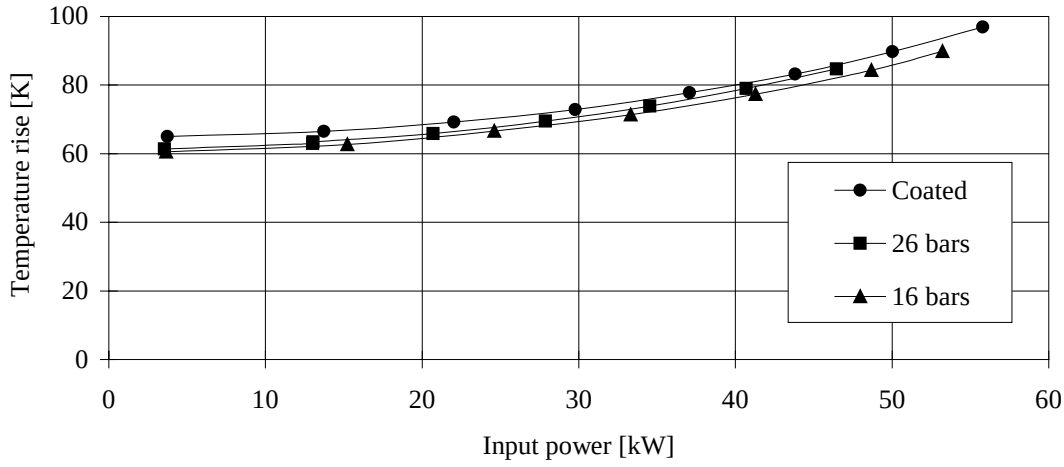

Fig. 5.4 Measured average temperature rise in the stator winding.

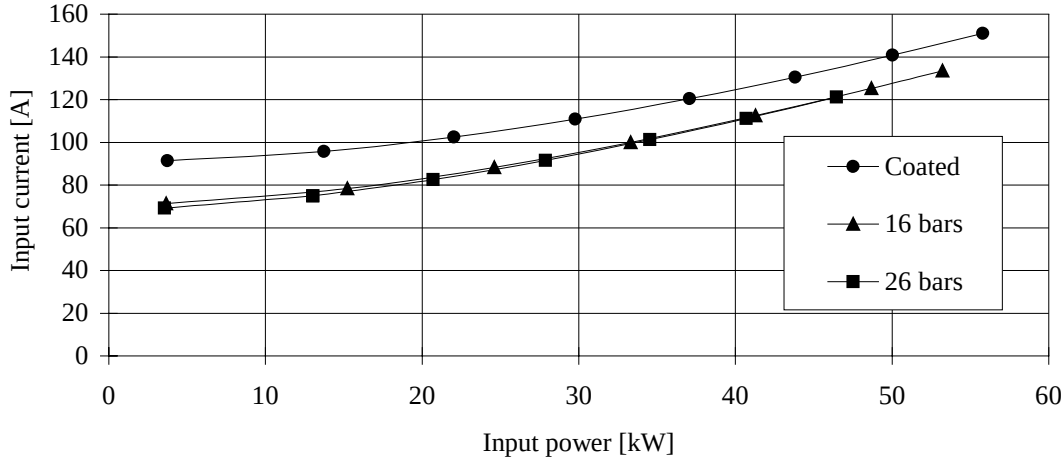

Fig. 5.5 Measured input current.

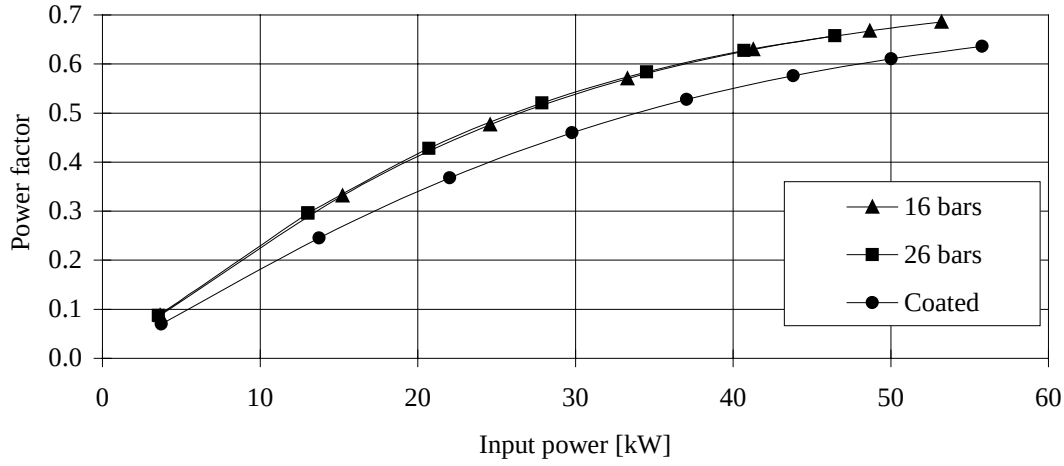

Fig. 5.6 Measured power factor.

5.2.3 Temperature rise and slip of the rotor

Figs. 5.7 and 5.8 show that the copper coated rotor outperforms the squirrel cage rotors as far as the temperature rise of the rotor and the slip is considered. The temperature of the rotor surface was coolest with the copper coated rotor. At the input power of 50 kW, the temperature rise is 6 % less than that of the 16 bar rotor. The difference is bigger if the slip is considered. The slip of the 16 bar rotor is 33 % higher than that of the copper coated rotor. This indicates that for the 16 bar rotor there is a higher power loss relative to the torque producing components of power.

As is mentioned in Section 3.5, the total amount of copper in the 26 bar rotor was accidentally reduced during the manufacture. The rotor operated with a high slip and produced an increased amount of loss. The increased loss resulted in reaching the limiting rotor surface temperature of 150 °C much earlier than with the other rotors. The difference between the coated and the 16 bar rotor can also be explained to some extent as a similar error in manufacture. This issue is further discussed in Chapter 9, where the squirrel cage design is optimized.

5.2.4 Total loss of the induction motor

Fig. 5.9 shows the total loss of both the machines as a function of the input power of the motor. It includes the electromagnetic loss and friction loss. The friction loss is a function of slip and thus the amount of friction loss differs slightly from point to point.

The figure confirms that the 26 bar rotor has the highest amount of power loss. The difference would be even greater if the generator had also had a 26 bar rotor during the test. The copper coated rotor and the 16 bar rotor performed better with no significant difference in between them.

Because a major part of the loss is friction loss, the resolution of the figure is not so good if electric loss is to be compared. However, a more accurate division of loss is possible when a back-to-back test setup is used. Friction loss itself was measured using a retardation test.

5.2.5 Division of power loss into loss components

From the measurement results, it could be seen that while the copper coated rotor and the 16 bar rotor had about the same amount of total loss, the loss distribution was different. The Copper coated rotor had more resistive loss at the stator side due to high stator current. On the other hand, the 16 bar and 26 bar rotors had more load loss. A following procedure was used to separate the measured loss between the two machines and into different loss components. The fact that both the motor and the generator are exactly the same, except with the 26 bar rotor, makes the division easier.

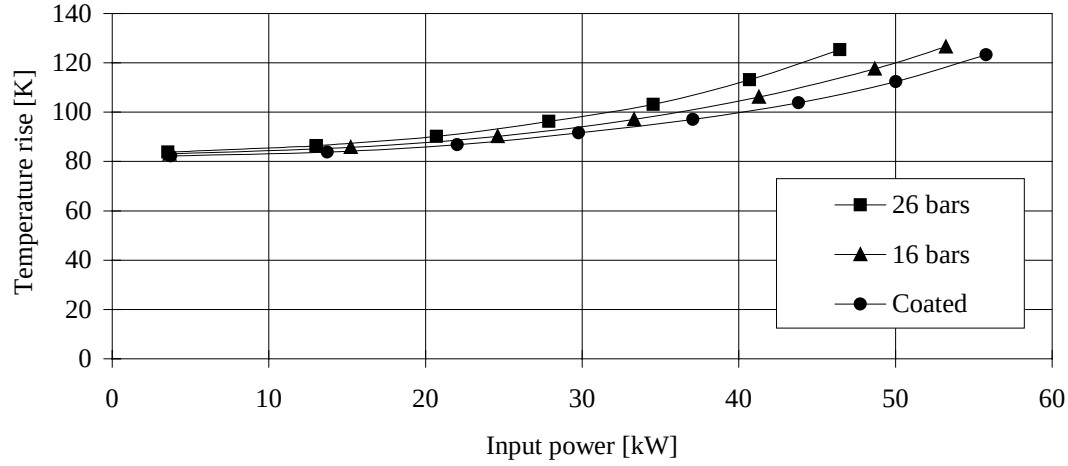

Fig. 5.7 Measured temperature rise of the rotor surface.

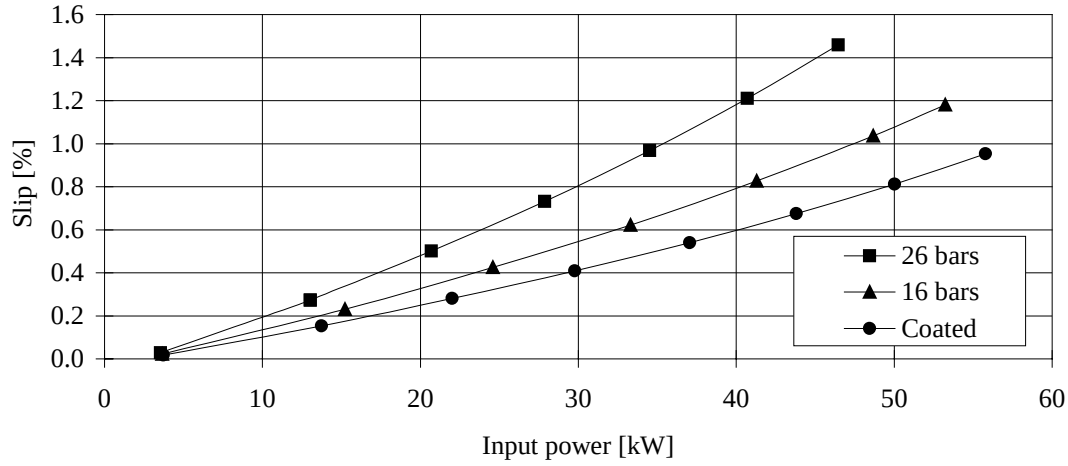

Fig. 5.8 Measured slip.

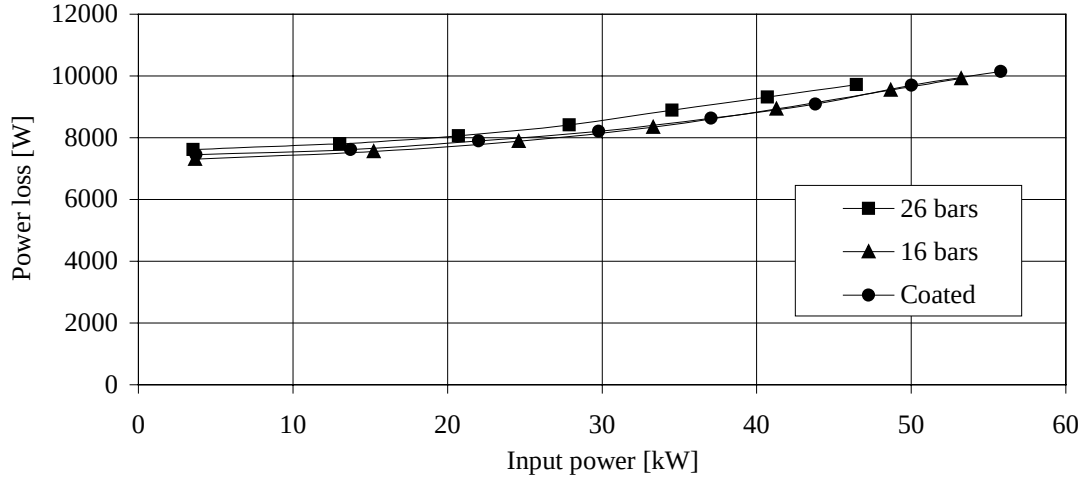

Fig. 5.9 Total loss measured. In the measurement for the motor with the 26 bar rotor, a rotor with 16 bars was used in the generator.

1. To start with, the total loss of the two motors is measured. The total loss is the difference of the input power of the motor and the output power of the generator. The AMB loss and cooling loss are excluded.

2. The resistive losses in the stator windings of the motor and the generator are calculated from the measured current and DC-resistance. The DC-resistance measurement is started immediately after each load test. A computer controlled relay system disconnects the VSI from the motor mains and connects the DC-voltage source within a fraction of a second. The DC-current is measured with a NORMA power analyzer and the voltage with a Fluke multimeter. Eddy-current effects are not taken into account in the loss value.

3. The harmonics loss fed to the machines is measured with the NORMA power analyzers. The share of resistive loss in the stator winding is already calculated in step 2. This component was only around 5 % of the harmonics loss, so most of this power loss is generated in the stator iron or in the rotor.

4. The friction loss is measured with a retardation test. The test starts with the motors running at a small overspeed and at no-load. The VSI supply is cut off and the rotors come coasting down. It takes almost half an hour for the rotors to stop from the nominal speed. The AMB system provides the rotational speed as a function of time. When the moment of inertia is known, the friction loss can be calculated.

   The retardation test could be done with and without the forced cooling. The difference in the friction loss values is the cooling friction loss. This component was only around 1 % of the friction loss in the motors studied.

5. The division of load loss and no-load loss is based on a definition that at zero slip there is no load loss. The magnetization loss is thus defined as the rest of the loss when all the loss components mentioned before are subtracted from the total loss at zero slip.

   Mainly because of the friction loss, the exact zero slip operation was not possible to achieve and the total loss at the zero slip was extrapolated.

   This magnetization loss is then divided between the motor and generator. The division is based on the calculated magnetization voltage which is the supply voltage corrected with the resistive voltage drop in the stator winding. The ratio of the losses in the motor and the generator is relative to the squares of the magnetization voltages. Because of the voltage drop in the winding, the magnetization loss actually changes a bit as a function of the load.

6. The rest of the loss is defined as a load loss. The division between the machines is related to the square of the slip, taking the rotor temperature into account. The load loss is generated in the rotor but also in the stator. The division of the loss between these parts of the motor is difficult. Eq. 4.2 can be used to calculate the theoretical load loss needed to produce the torque and the power. Fig. 5.12 shows that this minimum loss was less than half of the load loss measured.

The division of loss leads to the estimate of the shaft power. Figs. 5.10 – 5.11 show the results as a function of the estimated shaft power. Fig. 5.10 shows that the motor with a copper coated rotor has the most electric loss at no-load but the least electric loss at full load. The 26 bar rotor operates well in a no-load situation. There the reduction of the copper in the rotor does not have such a negative effect. As can be seen from Fig. 5.11, the electric efficiencies with different rotors are about the same. However, even small differences are important because the cooling of the motors is difficult.

Fig. 5.12 shows the power loss components at the individual full load points. The amount of the friction loss for the 26 bar rotor is higher than for the other rotors. The surface of the rotor was not entirely smooth. This result underlines the importance of having a smooth rotor surface.

5.2.6 Results for low magnetization level

Figs. 5.13 – 5.18 show the measurement results in case of a lower magnetization level. The magnetization was set to 85 % of the nominal value. Comparison of different rotors yielded similar results than with the nominal magnetization.

Comparing to the nominal magnetization, the temperature rises of the stator winding decreased at no-load and remained the same at full load. Stator currents decreased at no-load but increased at full load. Power factors were higher in the whole operation range.

The input and output power are limited by the temperature rise in the rotor. The 26 bar rotor had a maximum slip of 1.7 %, which means as much as 14 Hz frequency for the fundamental flux in the solid steel rotor. Only 41 kW could be fed to the motor before reaching the temperature limit for the rotor.

At no-load and at partial loads, the power loss values are lower than with the nominal magnetization. At no-load, the difference is around 10 %. At full load, the coated rotor performs slightly better than the 16 bar rotor. This is probably because of the lower slip for the coated rotor.

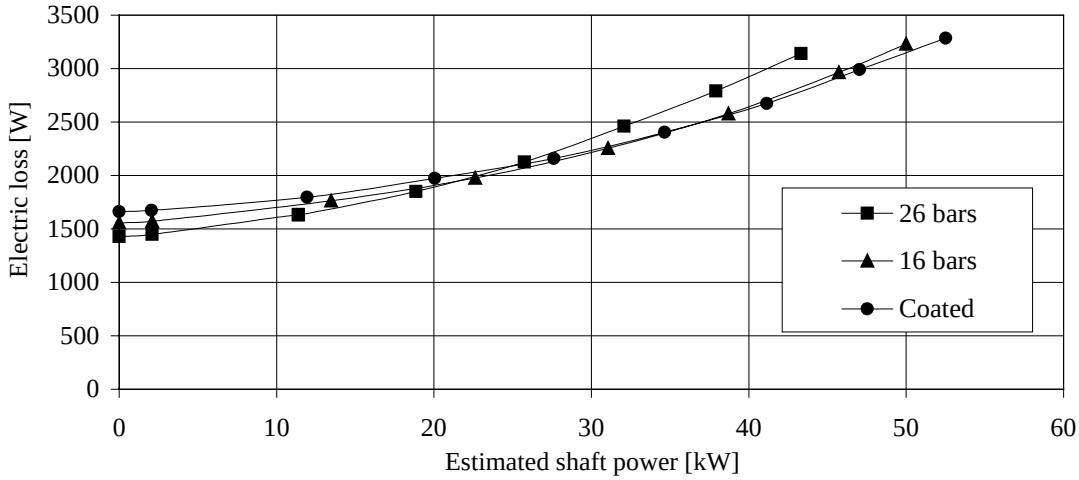

Fig. 5.10 Electric power loss.

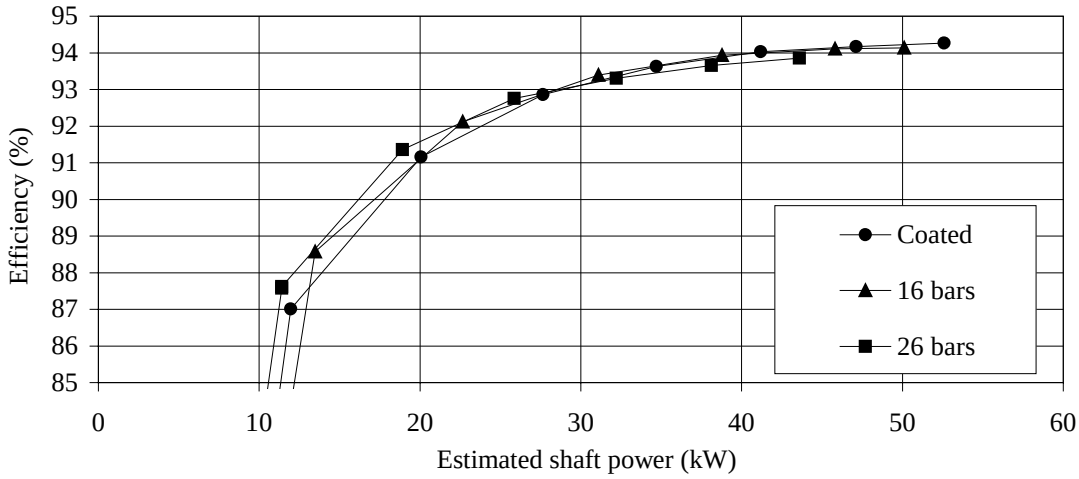

Fig. 5.11 Electric efficiency as a function of shaft power.

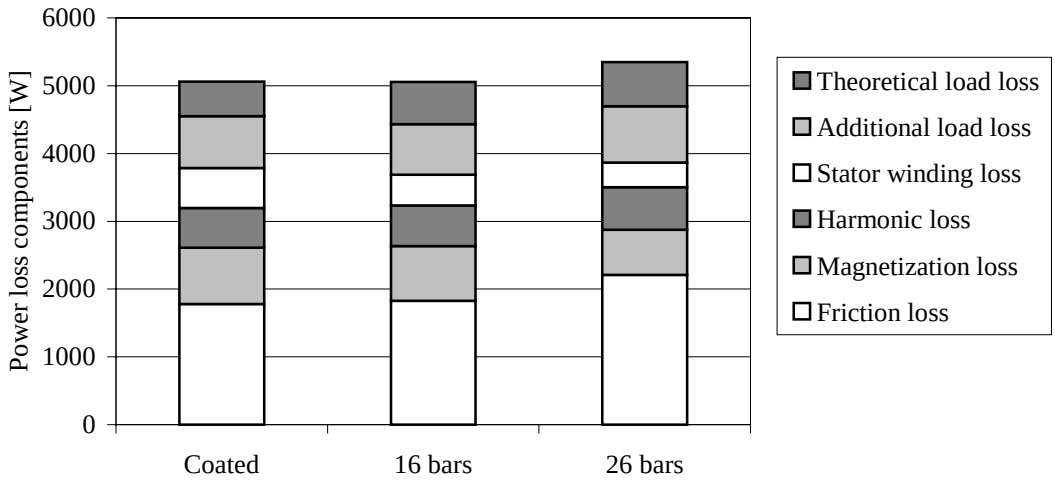

Fig. 5.12 The division of the total loss of the motor into components at full load.

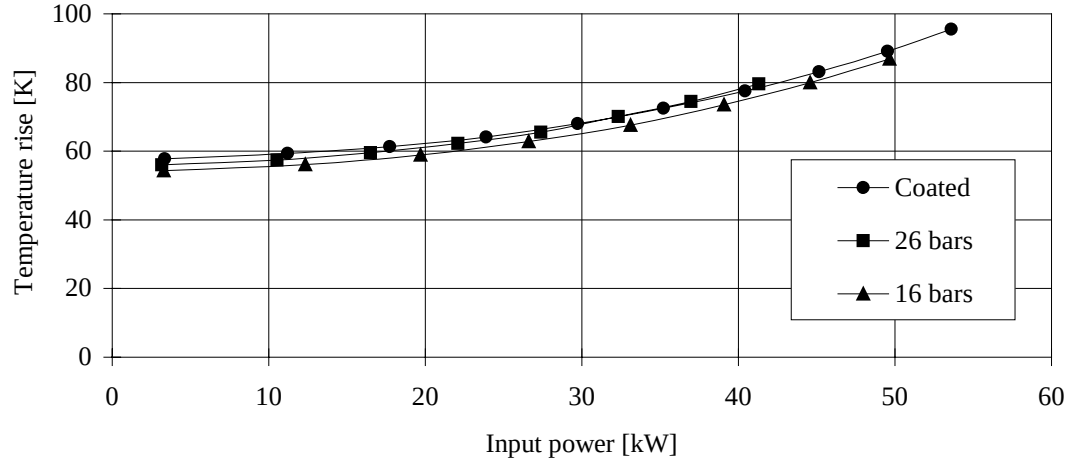

Fig. 5.13 Measured average temperature rise in the stator winding. Magnetization 85 % of nominal.

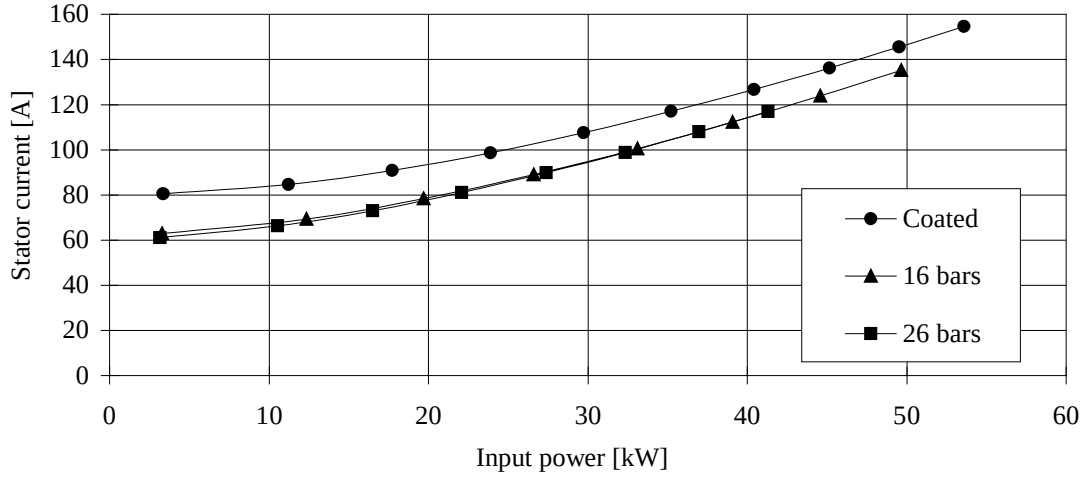

Fig. 5.14 Measured input current. Magnetization 85 % of nominal.

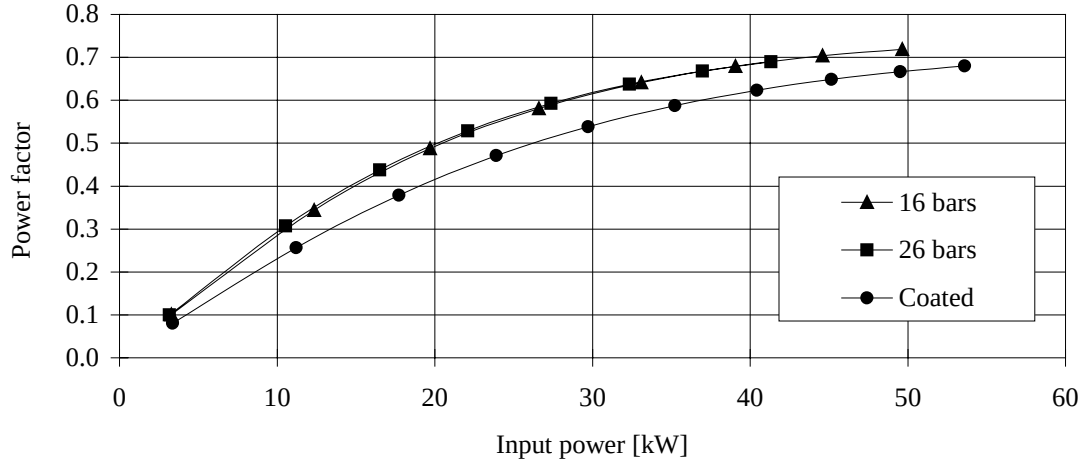

Fig. 5.15 Measured power factor. Magnetization 85 % of nominal.

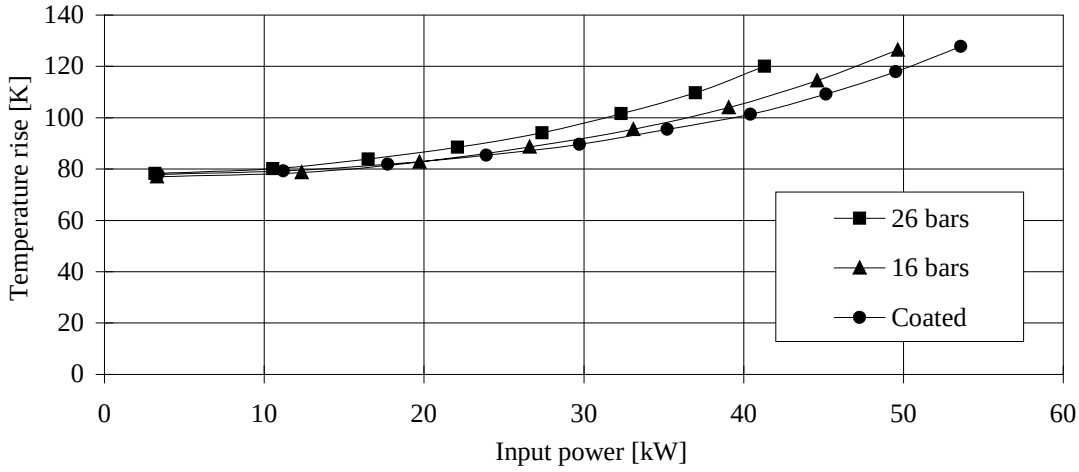

Fig. 5.16 Measured temperature rise of the rotor surface. Magnetization 85 % of nominal.

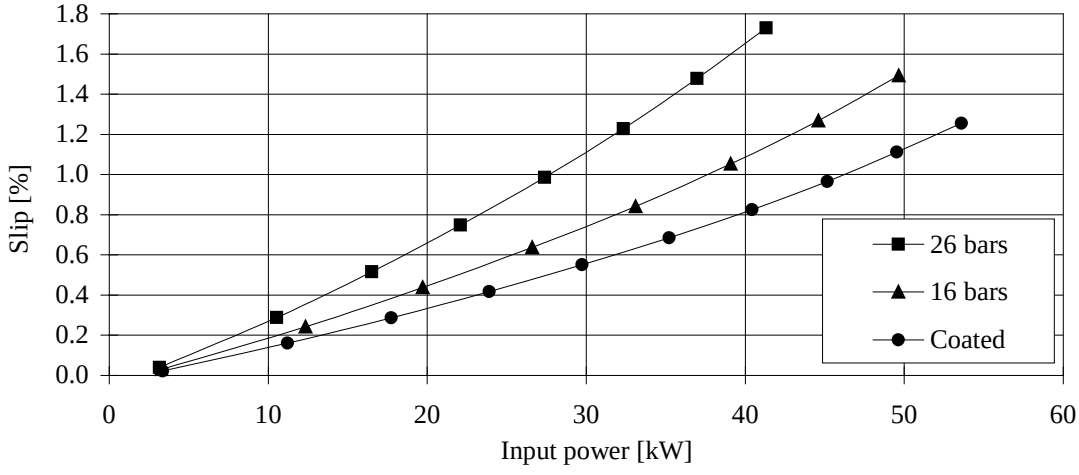

Fig. 5.17 Measured slip. Magnetization 85 % of nominal.

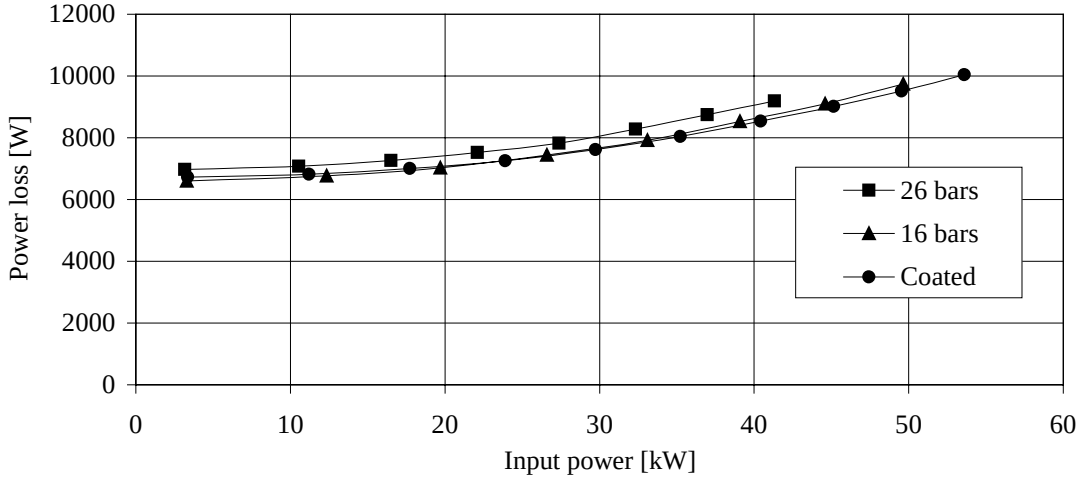

Fig. 5.18 Total loss measured. In the measurement for the motor with the 26 bar rotor, a rotor with 16 bars was used in the generator. Magnetization 85 % of nominal.

5.2.7 About the mechanical robustness

As a last operation characteristic it should be mentioned that all the tested rotors gave no sign of mechanical detoriation or fault. The 50000 $^{1}/_{min}$ and 150 °C limits for the squirrel cage rotors were adequate and higher speeds and temperature could be tested in the future.

With the squirrel cage rotors, a trade-off must be made between the maximum speed and the amount of copper in the cage. This is because the amount of copper is limited by the centrifugal forces acting on the rotor. For a certain rotational speed, the squirrel cage has to be designed so that it gives a good performance while meeting the mechanical limitations. Basically this means the selection of an optimal height, width and number for the bars. This is done in a numerical optimization case in Chapter 9.

5.3 Conclusion

Three different solid rotor constructions for a high-speed electric motor were tested. Two solid steel rotors with a surface mounted squirrel cage were presented and compared against a commercially used copper coated solid steel rotor.

The results showed that the squirrel cage rotors could increase the utilization factor and efficiency if properly designed. In the application considered, the limiting characteristic for use of the squirrel cage rotors was the mechanical coupling of copper and steel in the rotor and thus the measurements were made at 835 Hz for a 1000 Hz drive.

The squirrel cage rotors have better magnetization properties. They yielded a lower temperature rise for the stator winding, a smaller input current and a better power factor. The copper coated solid steel rotor had the smallest rotor and total loss and best efficiency at maximum load. Also, the copper coated rotor has a mechanical advantage. The full potential of the 1000 Hz drive could not be reached with the squirrel cage rotors because of the mechanical limits. Only a properly designed squirrel cage rotor will have an electromagnetic advantage at the high speed/power range.

Because the differences in performance were relatively small, it is hard to make any definitive judgment. The stator and rotor constructions were not optimized together or separately. It is perhaps safe to say that both approaches have possibilities. A properly designed squirrel cage rotor could be an electromagnetically better option, especially at a lower speed range. The coated rotor should probably be emphasized at higher speeds because it is mechanically stronger.

6 VOLTAGE MODULATION FOR THE HIGH-SPEED INDUCTION MOTOR

In this chapter, effects of different voltage modulations on the performance of the high-speed induction motor drive are studied. Preference for different voltage waveforms is derived theoretically and compared against the measurements. The back-to-back measurement setup for the 60 kW 60000 $^{1}/_{\text{min}}$ high-speed motor drive is used in the measurements. The setup was presented in Chapter 5, where a comparison of different rotors for the high-speed motor was reported. The motors studied here have copper coated solid steel rotors.

The motivation for this part of study was to see how different voltage modulations affect the power loss in the high-speed motor and the frequency converter feeding the motor. The study concentrates on the type of a frequency converter that has a voltage source inverter feeding the motor. Fig. 6.1 shows the frequency converters used to feed the high-speed machines with an appropriate voltage and frequency. Current source inverters are not considered in this study.

Three phase frequency converter	
Model	VACON NX5
Current	205 A
Voltage	380 – 500 V
Input frequency	45 - 66 Hz
Output frequency	up to 7200 Hz
Switching frequency	up to 16000 Hz
Input side	choke + diode rectifier
Intermediate link	DC-voltage capacitor
Output side	IGBT - inverter
Output signal	PWM voltage
Modulation type	synchronized carrier, sine-triangle comparison with added 3rd harmonic

Fig. 6.1 A photograph and data of the frequency converters used to supply the 60 kW 60000 $^{1}/_{\text{min}}$ high-speed machines in the back-to-back test setup. Converters in the picture are fitted side by side in the rack, power cables above connecting the DC-links.

6.1 Comparison of PAM and PWM for 60 kW 60000 $^{1}/_{min}$ drive

In comparison of modulation techniques, different performance criteria can be selected. For example, torque, speed and position precision are important in machine tools and the modulation should be optimized in that respect. In the application used in this study, the more important criteria are efficiency and utilization.

For the high-speed induction motor studied, the utilization depends on the temperature rise of the stator winding. The harmonic currents produce extra loss in the winding and the winding loss is the most important loss component for the temperature rise (Saari 1995). From this point of view, the voltage waveform should be selected so that the harmonic content of the current is the smallest. If skin effect is neglected, the power loss depends on the rms-value of the harmonic currents but not on the frequency of the harmonic components.

Iron loss due to the harmonics is frequency dependent. Much of the power loss caused by harmonics are induced in a copper coating of a coated solid steel rotor. Due to skin effect this loss is frequency dependent. Thus, if the efficiency of the motor is to be maximized, both the rms-value and the frequency spectrum of the harmonic current must be considered.

In PWM modulation, increasing the switching frequency increases the number of the pulses per half a cycle. According to the assumption that the harmonic currents mainly see the leakage reactance as a load, the higher the switching frequency the better. This is because the harmonic content of the voltage is moving upwards in frequency scale as the switching frequency goes up. Thus, the amplitude of harmonic currents decrease. The downside is then the increased switching loss that is proportional to the switching frequency. The switching loss in the IGBT bridges can become a major loss component for the frequency converter at high load and switching frequency. This will be seen in the measurement results later on.

In the next section, a theoretical comparison between different voltage waveforms is made. The comparison considers the harmonics loss in the motor. It is assumed that the loss is relative to the rms-value of the harmonic current. The comparison is not influenced by the load impedance of the motor. This is made possible by comparing the different voltage waveforms against PAM. The comparison method was used by Holtz (1994).

After the theoretical comparison, the results of the actual measurements are reported. At this point, the main issues are the utilization and power loss of the motor and the power loss in the inverter. The relation between harmonics current and harmonics loss for the different waveforms is studied.

Having the maximum switching frequency of 16000 Hz, output frequency of 835 Hz and Eq. 2.10 in Section 2.5, the following waveforms were compared: PAM and PWMs for 3, 9, and 15 pulses per half a cycle (pphc). Because the frequency converter used could not adjust the DC-link voltage, PAM was realized by changing the supply voltage of the converter. The voltage waveforms are presented in Fig. 6.2.

6.1.1 Theoretical comparison

The rms harmonic current I_h supplied to the stator windings of the motor is

$$I_h = \sqrt{\frac{1}{T}\int_T \left[i(t) - i_1(t)\right]^2 dt} \tag{6.1}$$

where i_1 is the fundamental current. The harmonic current depends on the voltage waveform as well as on the load impedance. In order to eliminate the load impedance from the comparison, a distortion factor d is used:

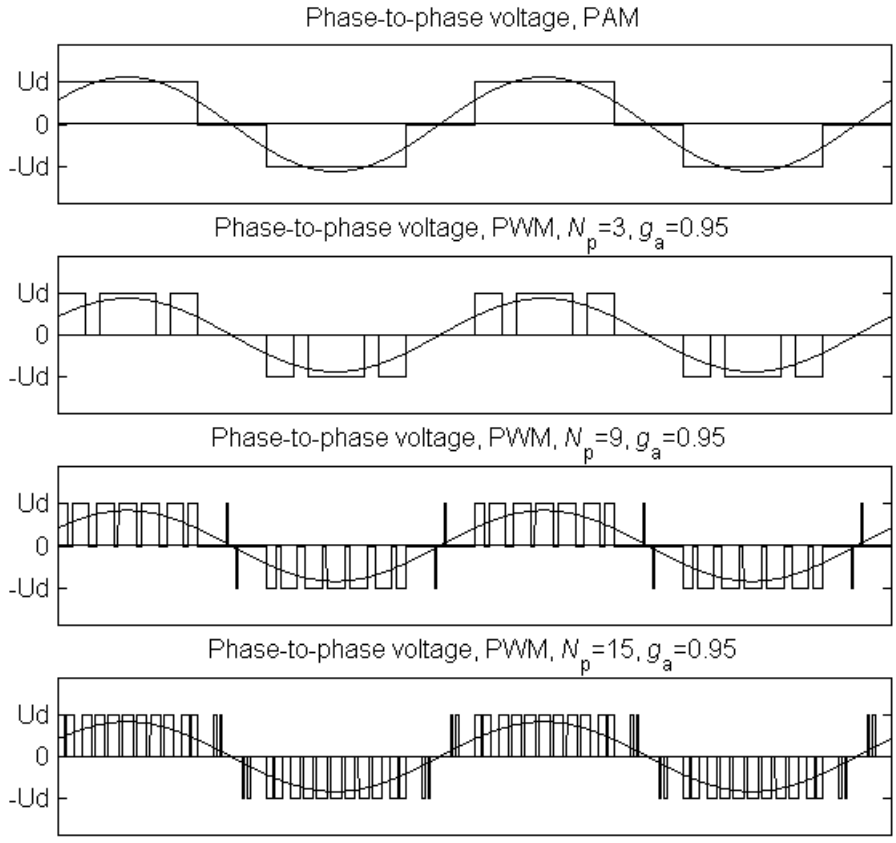

Fig 6.2 Output voltages produced by PAM and PWM for a star connected three phase winding. Fundamental of phase-to-phase voltage also plotted.

$$d = \frac{I_{\mathrm{h}}}{I_{\mathrm{h,PAM}}}, \tag{6.2}$$

where $I_{\mathrm{h,PAM}}$ is the harmonic current for PAM waveform. If discretized harmonic current spectrum is known, as is the case with synchronized modulation, we get

$$d = \sqrt{\sum_{\nu \neq 1} h_\nu^2}\ , \tag{6.3}$$

where h_ν is the ν^{th} order normalized component of the current spectrum

$$h_\nu = \frac{I_\nu}{I_{\mathrm{h,PAM}}}\ \ , \ \ \nu = 2,3,.... \tag{6.4}$$

The power loss considered here is proportional to the square of the harmonic current. The square of d is called a loss factor, showing the relative goodness of the modulated voltage as far as the power loss is considered. Fig. 6.3 shows the loss factor for the compared voltage waveforms as a function of the modulation index g_{a}. According to the definitions, d and d^2 for PAM are always equal to one. It can be seen that PWM waveforms having 15 and 9 pphc outperform PAM at higher values of g_{a}, which is the most likely operation region of the inverter. The voltage waveform having 3 pphc is significantly worse at any but maximum values of g_{a}.

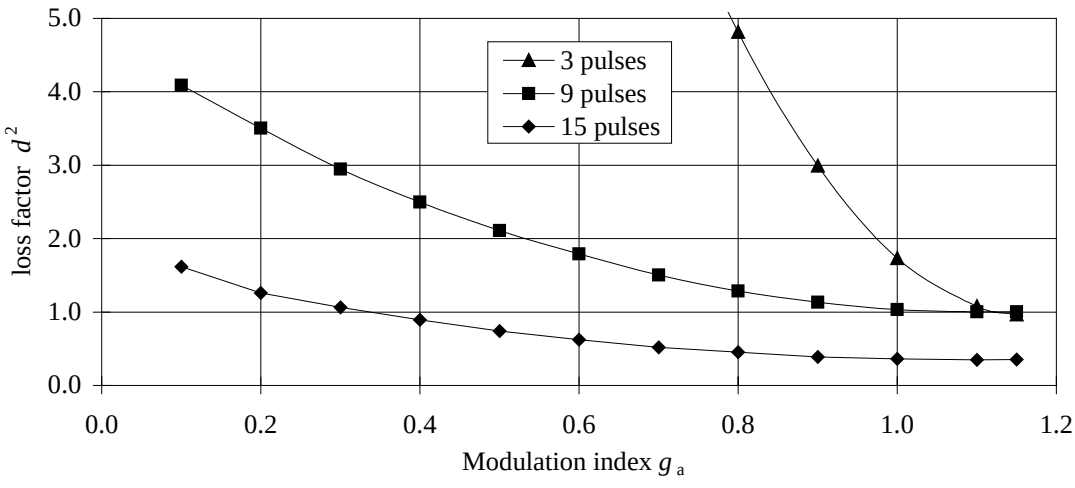

Fig. 6.3 Loss factor as a function of modulation index. PAM yields loss factor of 1.

6.1.2 Thermal measurements

Thermal measurements for the high-speed motor were performed in the same way as was reported in Chapter 5. To be precise, the nominal shaft power at 50100 $^{1}/_{\text{min}}$ is 50 kW but here the input power of the same amount is selected as a reference point. Operation points in which both the motors are supplied with the same frequency is considered as a no-load point. At those points, the input power is consumed as magnetization and friction loss. The current and phase-to-phase voltage waveforms measured are shown in Figs. 6.4 – 6.7.

Fig. 6.8 shows that from the utilization point of view PAM gives the best performance. 8 % more power can be fed to the motor at the temperature rise of 100 K compared to PWM having 15 pphc. This temperature rise is close to the 105 K limit for insulation class F (IEC Standard 34-1 1994). At the nominal power of 50 kW, the temperature rise for the PWM having 15 pphc was 5 K higher than for PAM.

Other PWM waveforms performed worse and PWM having 3 pphc could be considered unacceptable. The result was interesting because the theoretical examination predicted better performance for the PWMs having 9 or 15 pphc.

Temperature rise of the rotor surface was measured in the same way as was reported in Chapter 5. Fig. 6.9 shows that these results are consistent with the temperature rises measured for the stator winding. Here the difference between PAM and PWM having 15 pphc was only marginal. It is worth mentioning that temperature rises even this high are not limiting the utilization of the motor. The copper coated rotor can take temperatures of around 180 °C according to the manufacturer of the rotor.

Both temperature rise measurements show that the differences between the waveforms do not depend on the load. This indicates that the differences are due to the different harmonic loss components. This is as it should be.

The temperature of the inverters IGBT bridge was also recorded using the monitoring feature of the frequency converter. The temperature was measured by the inverter module itself. The results in Fig. 6.10 show well the influence of switching losses on the temperature. The temperature was near the maximum level of 85 °C when using PWM having 15 pphc. The switching frequencies for PWMs with 15, 9 and 3 pphc and for PAM were 12525, 7515, 2505 and 835 Hz, respectively.

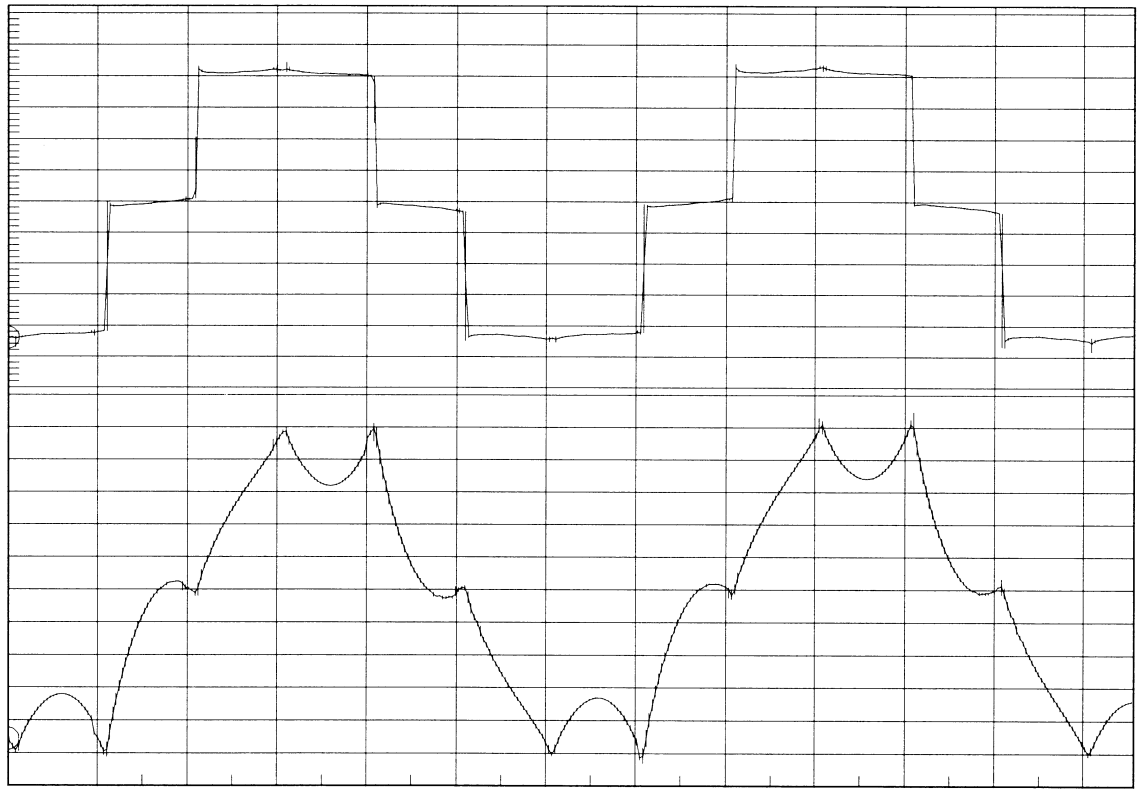

Fig. 6.4 Phase-to-phase voltage and phase current measured for PAM.

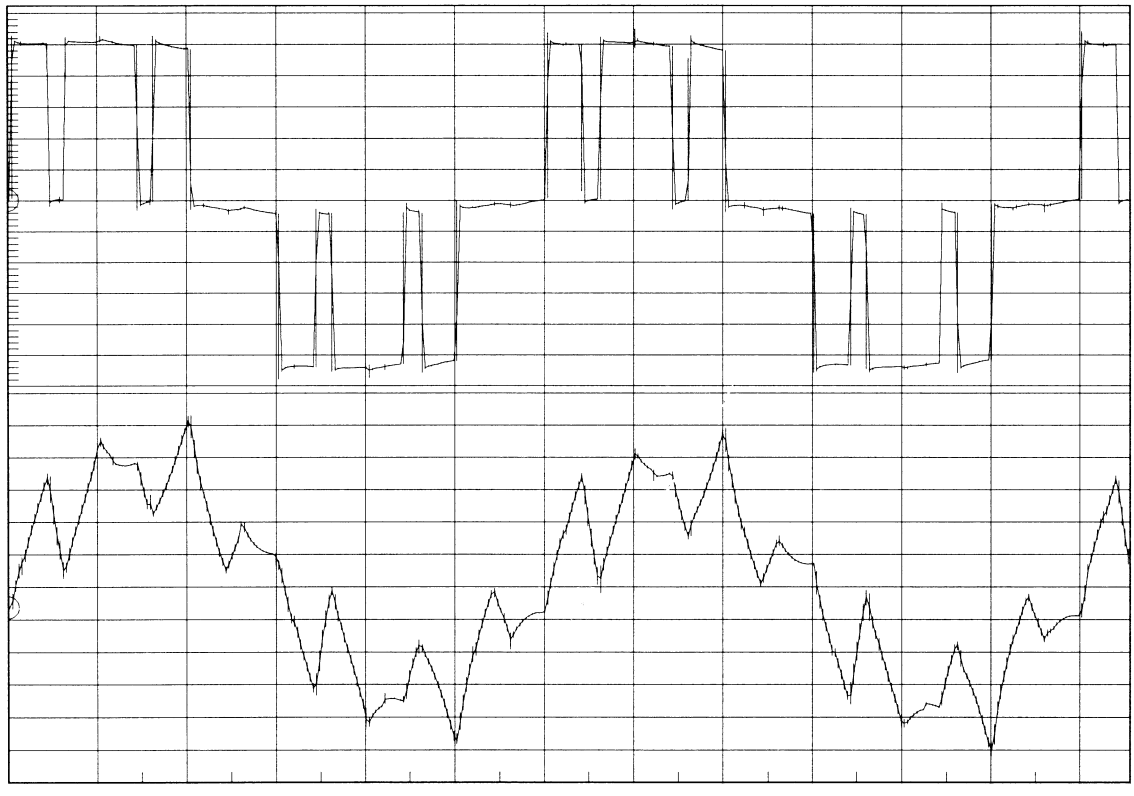

Fig. 6.5 Phase-to-phase voltage and phase current measured for PWM having 3 pphc.

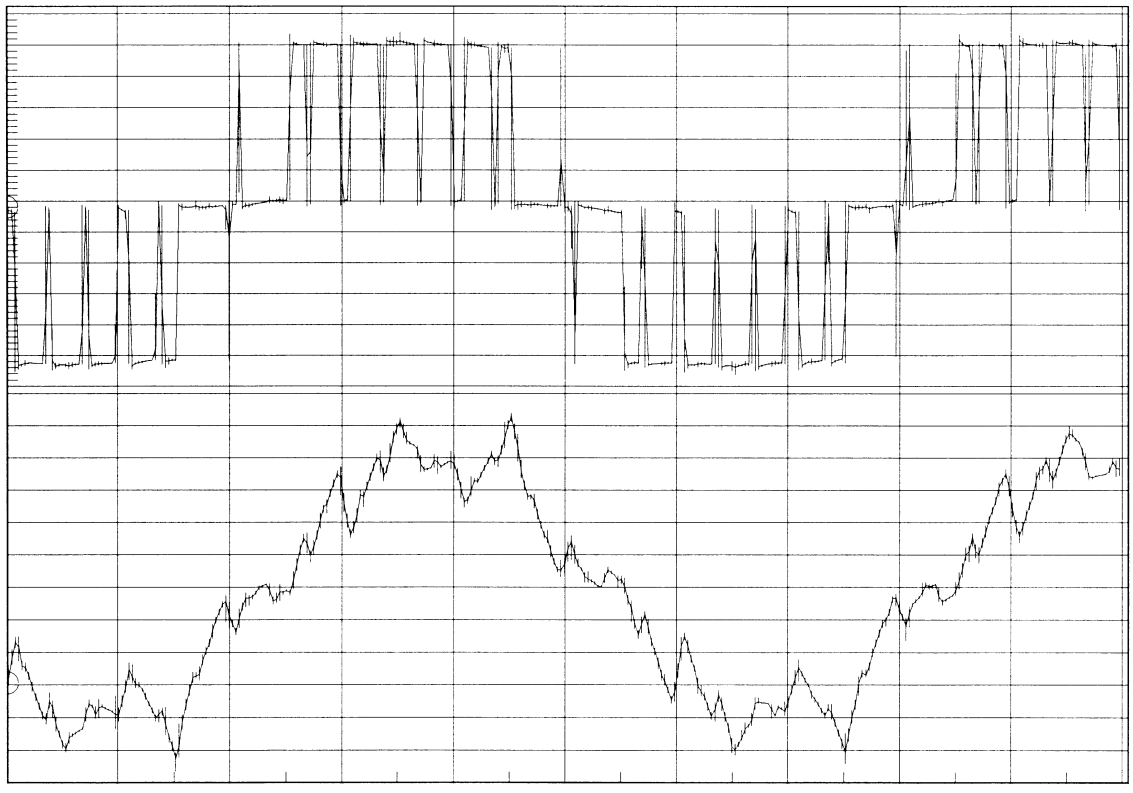

Fig. 6.6 Phase-to-phase voltage and phase current measured for PWM having 9 pphc.

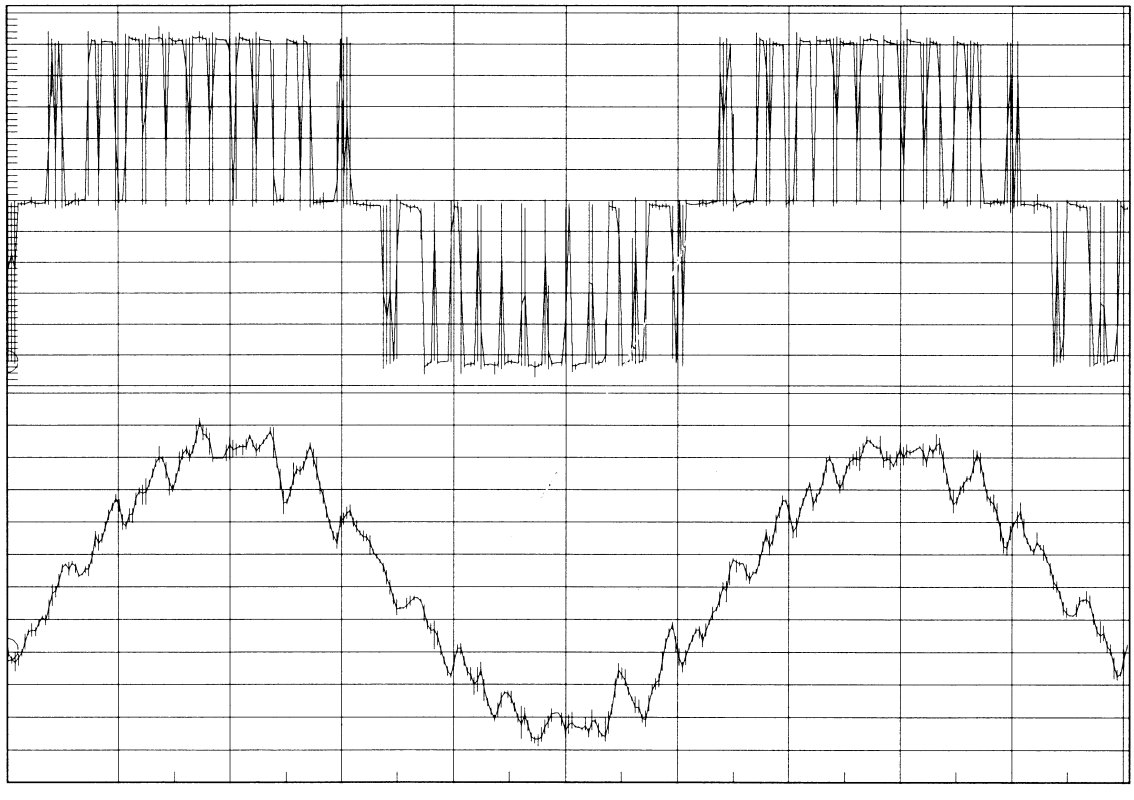

Fig. 6.7 Phase-to-phase voltage and phase current measured for PWM having 15 pphc.

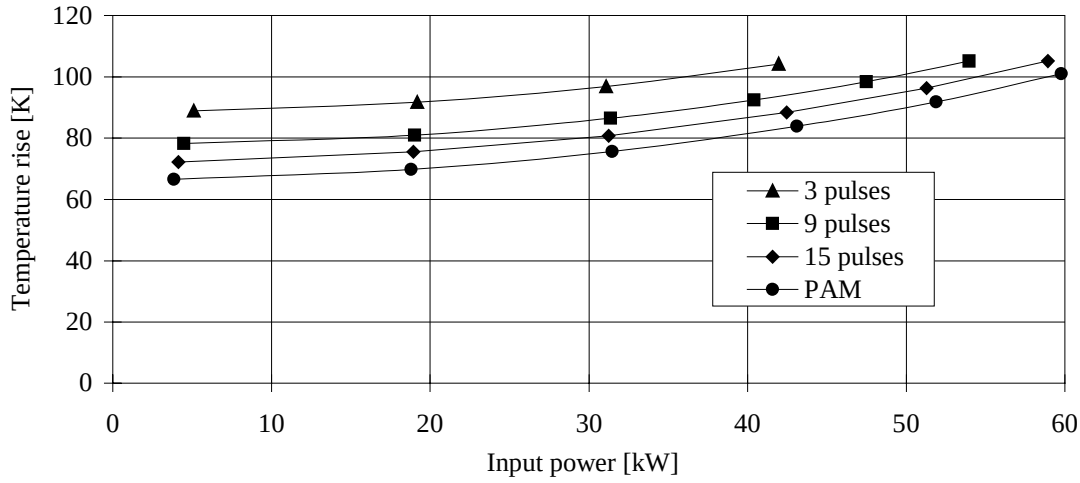

Fig. 6.8 Measured average temperature rise in the stator winding.

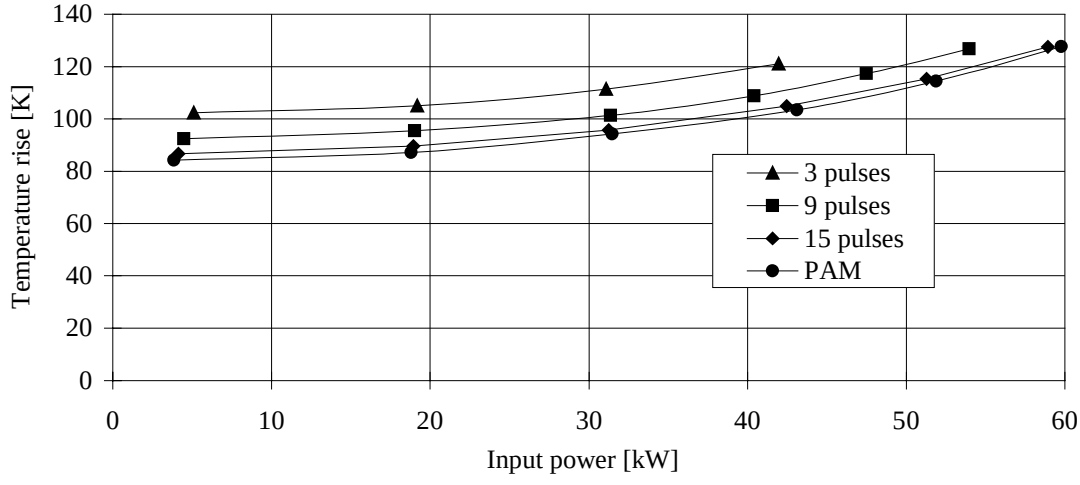

Fig. 6.9 Measured temperature rise of the rotor surface.

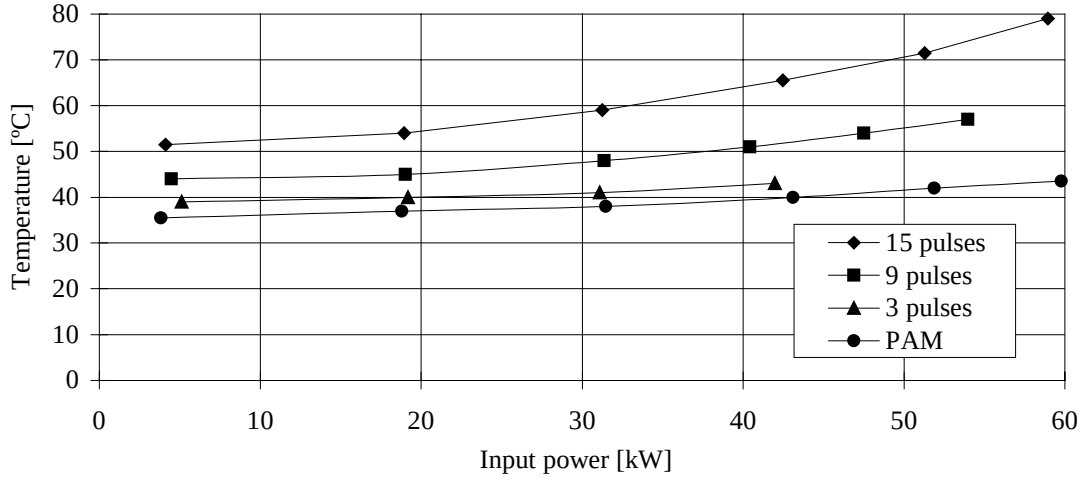

Fig. 6.10 Temperature of the IGBT module in the inverter for the motor.

6.1.3 Power loss measurements

In the power loss measurements, the losses were measured for both drives together. Knowledge of the actual shaft power would be needed in order to divide the losses in the machines between motor loss and generator loss. While the division of losses in back-to-back measurement was discussed and implemented in Chapter 5, no division is made here. Only the measured results are presented without any assumptions. The results are presented as a function of the input power of the motor.

Fig. 6.11 shows the total loss for the motor and the generator combined as a function of the input power of the motor. Again, PAM performs better than the PWM waveforms. The result is in agreement with the temperature rise measurements for the motor shown in Figs. 6.8 and 6.9. At the nominal power of 50 kW, the motor-generator system has 4 % more loss with PWM having 15 pphc than with PAM. Also here, the differences in the results are not a function of load.

Fig. 6.12 shows the total loss of the frequency converters combined. The result is in accordance with the temperature measurement for the IGBT bridge in the previous section. The loss increases as a function of switching frequency. At the nominal point of 50 kW, the PWM having 15 pphc produces as much as 121 % more loss in the converters than PAM. This is a serious draw-back of the good quality PWM waveforms. At no-load the difference is 94 %. Power loss for the converters without load was 400 W.

Fig. 6.13 shows the total loss of the induction motor drives combined. It is the power loss taken from the electricity network and measured with a single NORMA power analyzer. The result shows that PAM is superior to the PWM waveforms in this respect. At the nominal power point, PAM produces at least 17 % less power loss than the PWM waveforms. At no-load, the use of PAM reduces the loss at least 19 %.

It is worth mentioning that the total loss also includes the friction loss, which is around 3700 W for the machines combined. Considering only the electromagnetic losses of the drives, the difference between PAM and the PWM waveforms is even larger. Then the reduction is at least 23 % at the nominal load and 26 % at no-load.

It is interesting to see that at the nominal load, the PWM having 9 pphc yields less power loss than the PWM having 15 pphc. The increase in switching loss eats up the benefits of a better voltage waveform. At no-load point, these PWM waveforms produce the same amount of loss.

Fig. 6.14 shows the calculated values for the electric loss in the motor, using a model presented in Chapter 7. The results are well in line with the total loss measured for the machines in Fig. 6.11.

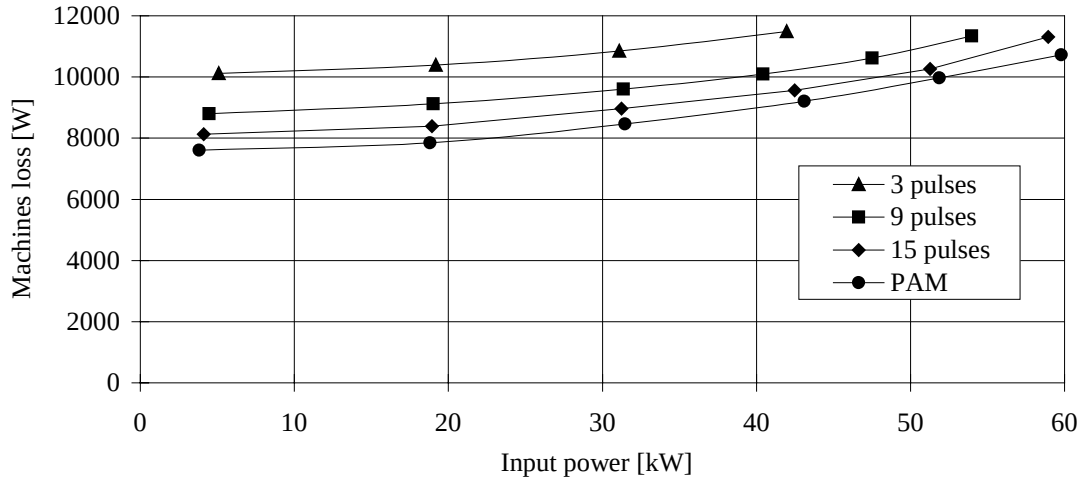

Fig. 6.11 Measured power loss of the machines.

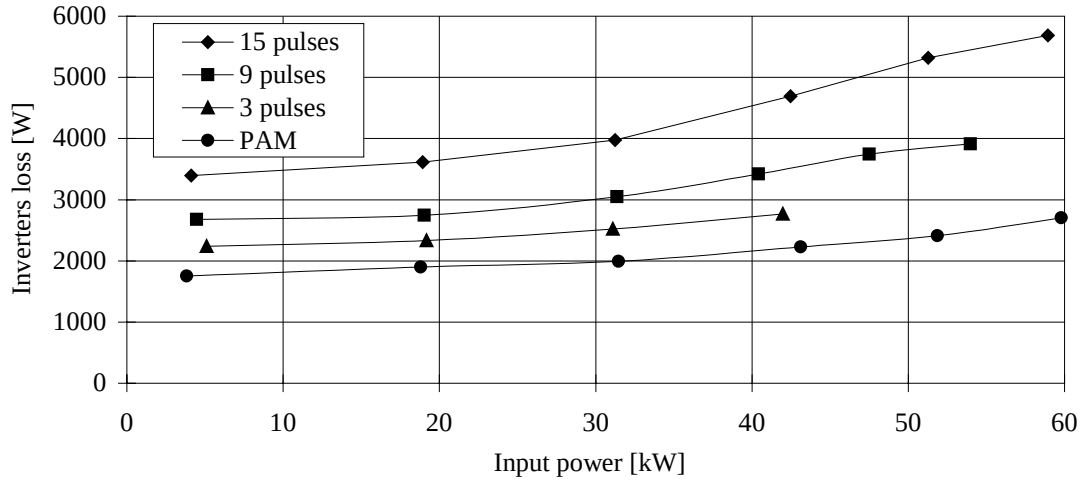

Fig. 6.12 Measured power loss of the frequency converters.

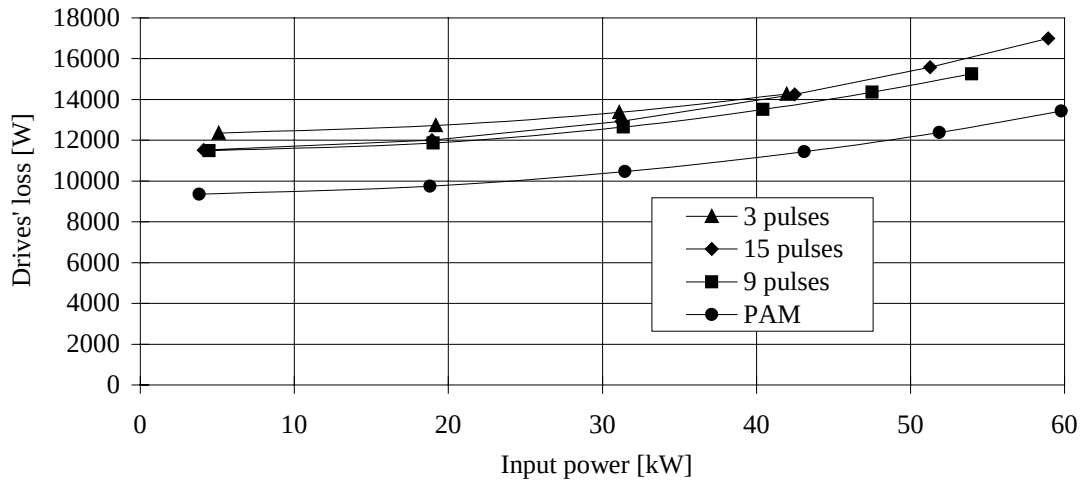

Fig. 6.13 Measured power loss of the drives.

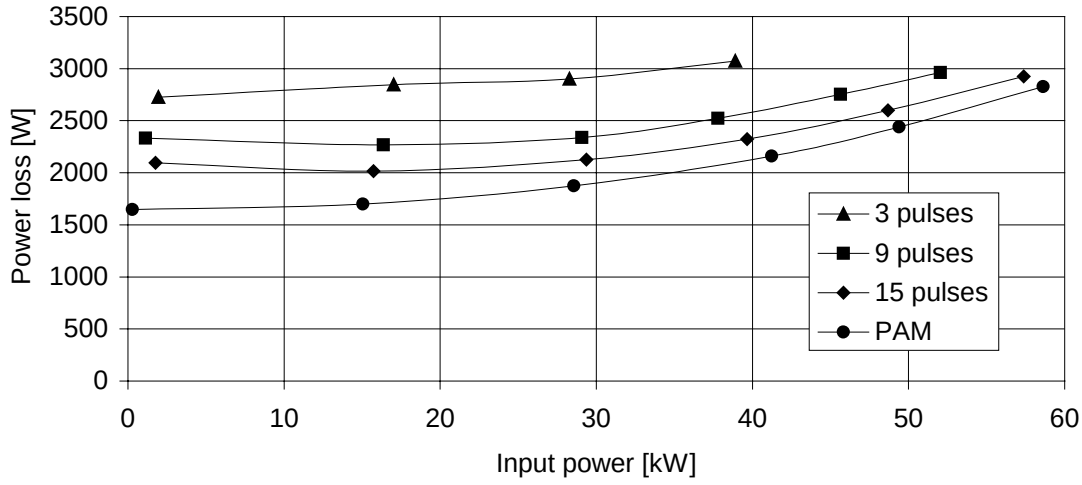

Fig. 6.14 Calculated electric loss of the motor.

6.1.4 Harmonics measurements

In the harmonics measurements, the harmonic content of input current and loss were measured for the high-speed motor. NORMA power analyzer measured the harmonic content of the input voltage, current and power up to the 40th order of harmonics. The power analyzer calculates the harmonic components from the sampled values using discrete Fourier transformation. The measurement was synchronized to the fundamental frequency. The component values were averaged values over 1024 periods of fundamental.

Fig. 6.15 shows the total harmonic distortion (THD) of the input current. THD is defined as

$$\mathrm{THD} = \frac{\sqrt{\sum_{\nu=2}^{\infty} I_\nu^2}}{I_1} \quad , \tag{6.5}$$

where I_1 is the fundamental current. The results are in accordance with the theoretical comparison. The PWM waveform having 15 pphc yields the lowest THD values and the PWM having 3 pphc the highest. The distortion factor d for PAM and the PWM having 9 pphc are close to each other as could be seen from Fig 6.3, where the square of d was plotted. The value of the modulation index was $g_a \approx 1$ for the PWM waveforms at the operation point measured. Measured data for input power, fundamental current and harmonics current are given in Table 6.1.

Fig. 6.16 shows the measured harmonic loss produced by the harmonic currents. The harmonics loss is the sum of harmonic loss components measured by the power analyzer. This time, the results do not agree with the theoretical comparison. The measured loss for PWM waveforms is

considerably higher than expected. The PWM waveform having 15 pphc and PAM produce about the same amount of loss even if d^2 and the THD measured for PAM are higher. The PWM waveforms having 3 and 9 pphc are inferior to PAM, but the difference is bigger than it should. On the other hand, the result agrees well with the temperature rise measurements for the motor.

The above result is presented in another way in Fig. 6.17. There the amount of harmonic loss P_h is divided by the square of the corresponding harmonic current I_h. Thus, the effective harmonic resistance R_h measured is defined as

$$R_\mathrm{h} = \frac{P_\mathrm{h}}{I_\mathrm{h}^2} \quad , \tag{6.6}$$

It can be seen that for the PWM waveform having 15 pphc the effective resistance is about three times higher than for PAM. The resistance goes up clearly as a function of the switching frequency.

The switching frequency f_sw or pulse number N_p determines the harmonic spectrum of the PWM waveform. Increasing N_p will move the harmonic content of the spectra upwards in the frequency scale. The idea is that a higher frequency voltage will see a higher impedance, and a lower amount of current and loss is induced. This applies well if the ohmic loss is considered.

On the other hand, hysteresis and eddy-current loss and the loss due to the circulatory currents in the stator winding increase as a function of the frequency. As is shown in Section 2.4, the relative importance of ohmic loss decreases proportional to the speed of the electric machine. The relative importance of hysteresis loss is constant and the importance of eddy current loss increases proportional to speed. The measurement results imply that the increase of this phenomenon severely decrease the benefits of having higher switching frequency and pulse number in high-speed motors.

Table 6.1 Measured data for input power, fundamental current and harmonics current.

3 pphc			9 pphc			15 pphc			PAM		
P_in [W]	I_1 [A]	I_h [A]	P_in [W]	I_1 [A]	I_h [A]	P_in [W]	I_1 [A]	I_h [A]	P_in [W]	I_1 [A]	I_h [A]
5091	88.0	46.8	4469	88.1	33.6	4112	87.9	20.7	3831	88.0	32.2
19178	95.4	46.8	19022	95.7	33.5	18933	96.0	20.8	18808	96.2	32.3
31088	107.4	46.7	31366	108.6	33.6	31235	108.6	20.6	31467	109.4	32.5
41971	121.7	46.7	40419	120.4	33.5	42471	123.8	20.7	43111	125.1	32.6
			47505	130.9	33.6	51275	137.3	20.7	51874	138.6	32.7
			53972	141.2	33.7	58935	150.2	20.6	59788	152.1	32.8

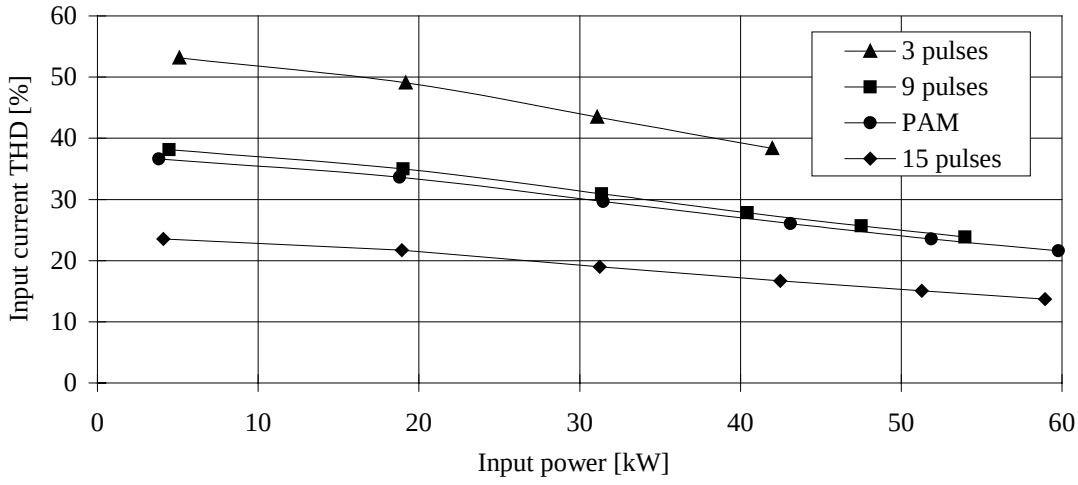

Fig. 6.15 Measured total harmonic distortion of input current for the motor.

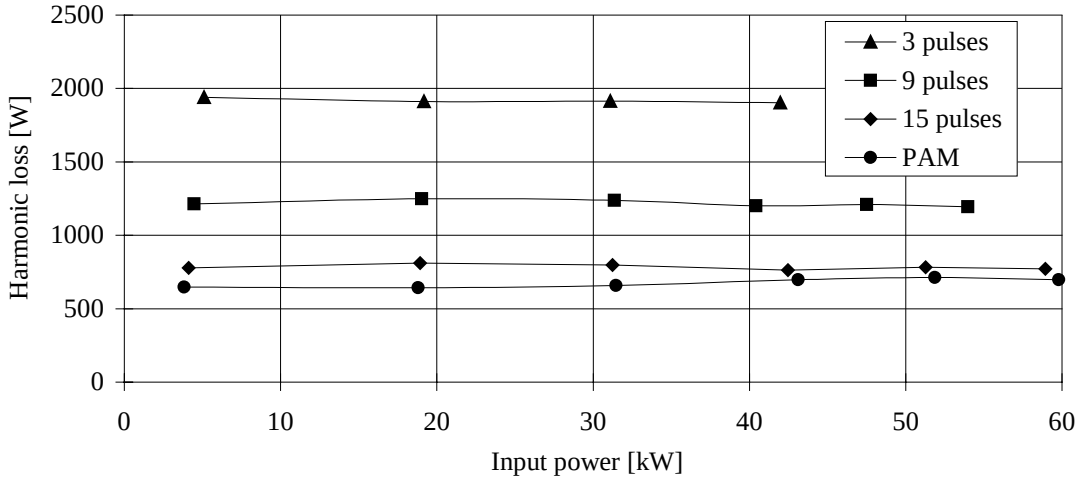

Fig. 6.16 Measured harmonic loss for the motor.

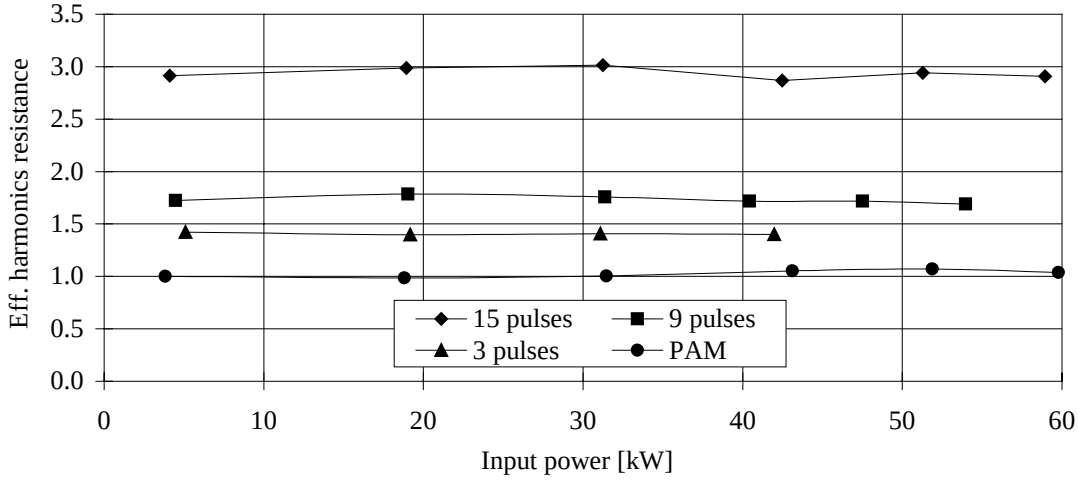

Fig. 6.17 Effective harmonics resistance relative to the resistance for PAM at no-load.

In order to improve the performance of the PWM inverter, some modifications must be made. One option would be to optimize the pulse waveform. This would be done by determining the switching instants for the individual pulses in order to have the lowest harmonic loss (Zach 1989). The switching instants for each pulse number and modulation index could be stored in the memory of the modulator. The optimization could be started using the same theoretical approach as presented in Section 6.1.1. More accurate results would require the use of a full model for the motor and possibly also for the inverter. This could be a challenging task because the model should include, for example, the effect of circulatory currents in the stator winding.

The PWM waveform having 9 pulses per half a cycle could be selected for the optimization. According to the results, it seems to generate a reasonable compromise between the inverter and motor loss, yielding a decent loss level for the drive system.

Another way to improve PWM and also PAM waveforms would be to put a LC filter between the inverter and the induction machine. This approach is used by Huppunen and Pyrhönen (2000) for a 12 kW 13500 $^{1}/_{\text{min}}$ high-speed solid rotor induction motor. The losses of the motor would decrease without increasing the losses in the frequency converter. Another advantage stated in the study is that the filter can compensate some of the reactive load of the induction motor. This may have a beneficial impact on inverter sizing.

6.2 Conclusion

The results of the measurements show that the idea of moving the harmonic content of voltage and current upwards in spectral scale by increasing the switching frequency does not apply well for the high-speed induction machine. The currents of higher harmonic order produce more loss than the same amount of lower order harmonics. This result, together with the consideration of inverter and drive loss, implies that PAM should be preferred as a voltage waveform for high-speed induction machines.

7 MODELING HIGH-SPEED MACHINES

In this chapter, some problems encountered in the modeling are discussed. Some modifications are made in order to make the models more appropriate for high-speed machines. In Section 7.3, the calculation results for the 60 kW 60000 $^{1}/_{\mathrm{min}}$ motor are reported and compared against the results of the measurements done in Chapter 5.

The modeling of a high-speed machine is a challenging task because different physical phenomena must be considered simultaneously. Because of high loss densities in the machines, the correct modeling of losses and cooling is essential. Thus, the electromechanical model should be somehow coupled to the thermal model. The electromechanical as well as the thermal models are presented shortly in Appendixes A and B.

In addition, a rotordynamic model has to be used to confirm the feasibility of the rotor design. For a detailed description of the rotordynamic FEM model used, the work of Lantto (1997) is referred.

The high-speed induction motors considered in this study are relatively short in length and large in diameter. This causes problems if a 2D FEM is used since the 3D effects are considerable. The 2D FEM assumes that the currents in the motor flow only in axial direction and the magnetic flux flows on a cross section plane of the motor. This is not the case in the real motor and the 3D effects have to be considered in more detail.

7.1 Modeling of the end region inductances

In the 2D FEM available, the 3D end region effects of the stator winding are included in the circuit equations. The resistance for the stator phases includes the resistance of the end winding regions. The leakage reactance X_{s} of the stator end winding is calculated using an empirical equation (Richter 1951):

$$X_{\mathrm{s}} = \frac{Q}{m} q \left(\frac{N_{\mathrm{u}}}{a} \right)^2 \omega \mu_0 l_{\mathrm{s}} \lambda_{\mathrm{s}} , \tag{7.1}$$

where Q is the number of the stator slots, m is the number of phases and q is the number of slots per pole per phase. N_{u} is the number of turns in series in a coil and a is the number of parallel paths. $l_{\mathrm{s}}\lambda_{\mathrm{s}}$ can be rewritten as (Jokinen 1982):

$$l_s \lambda_s = 2 l_e \lambda_e + l_w \lambda_w , \tag{7.2}$$

where l_e and l_w are the lengths of a coil end and a circular part of the end winding. λ_e and λ_w are empirical coefficients depending on the type of the winding system.

The end ring resistance and inductance of the squirrel cage are considered in a similar manner. In the case of a coated rotor, the coating is divided into bars and end ring parts and the same model can be used. The resistance of an end ring is calculated based on its dimensions and conductivity. In the initial FEM model, the inductance of the end ring was calculated using empirical equations for a thick cylindrical coil in air with a constant current density in the coil. These equations were presented by Foelsch (1936) with an error of less than 0.3 %:

$$L_{er} = \mu_0 N_c^{\,2} a_c \lambda_f , \tag{7.3}$$

where N_c is the number of turns and a_c is the average diameter of the coil. For the end ring, N_c equals one. λ_f is a coefficient depending on the dimensions of the coil. A total of eight equations for λ_f are needed to cover all the dimensions with the accuracy mentioned above.

For the high-speed rotors considered, this however does not give accurate results. The end rings are mounted on the surface of a solid ferromagnetic iron. Thus, the real values for the end ring inductance are higher than those given by Eq. 7.3. Also, the Foelsch method supposes that the current is constant in amplitude and direction around the coil. In reality, there is something close to a sinusoidal current coverage around the end ring.

To get another approximation for the end ring inductance, a separate 2D FEM calculation was made using free 2D FEM software called FEMM (Meeker 1999). In this case, a differential piece of an end ring was modeled in a planar coordinates system. Fig. 7.1 shows a quarter cross-section of the motor with a copper coated solid steel rotor. The magnetic field is induced by the end region currents in the stator and the rotor. The bottom boundary has the Neumann boundary condition and the right boundary has the Dirichlet boundary condition set. The rotor is situated at the bottom. The copper coating lies at the surface of the rotor. The end ring part of the coating is darkened. The other half of the stator stack, divided by the cooling duct, is on the right and the stator end winding is next to it in the center. On the left, there is a solid iron stator of the axial magnetic bearing.

Considering the small slip and the lamination of the stator core, the conductivities of the stator and rotor parts were zeroed. Only in the stator of the axial bearing can some eddy currents be seen flowing. No skin effect for the end ring or saturation of the iron parts was modeled. In the calculation for the inductance, only the end ring current was used to determine the self-inductance.

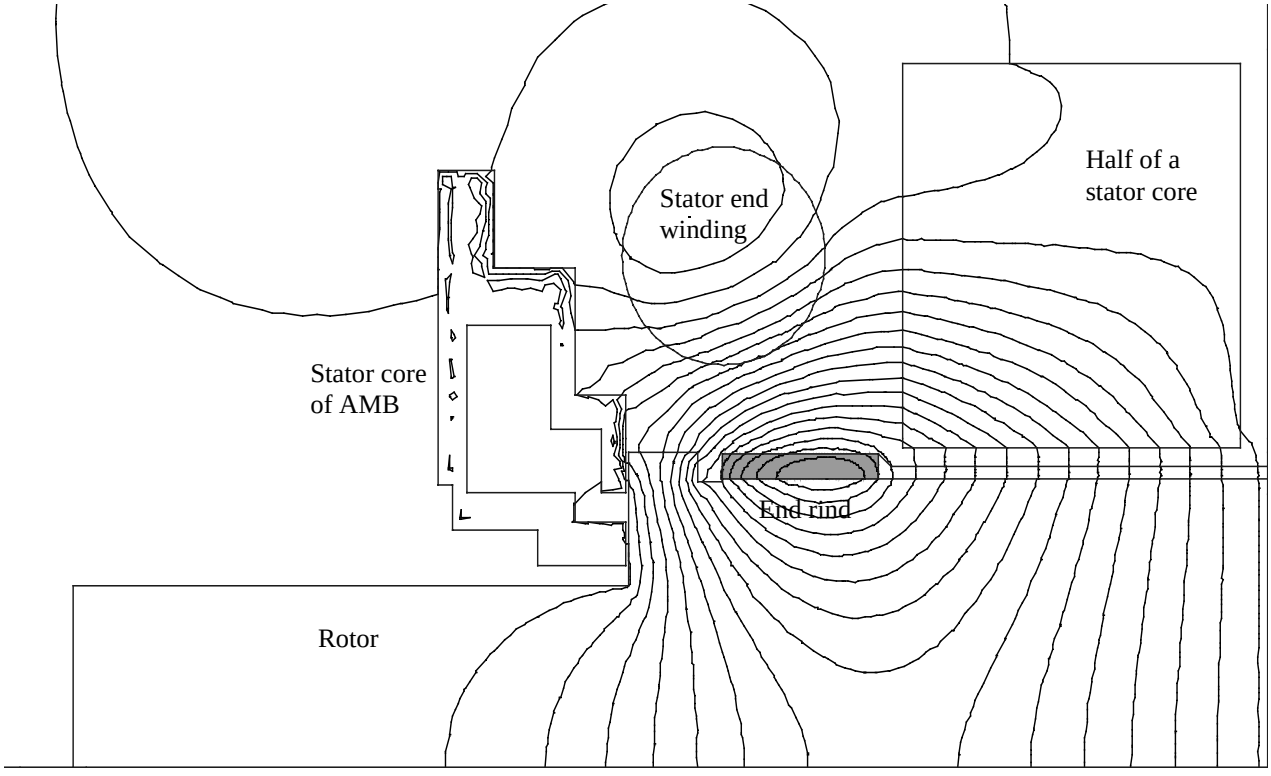

Fig. 7.1 A picture of a 2D FEM model to approximate the end ring inductance.

The inductances given by the 2D FEM were about four times bigger than calculated from Eq. 7.3 for the rotor constructions compared in Chapter 5. The model is not accurate but increasing the value of the inductance from the values given by Foelsch's method can be justified. Using a higher value for the end ring inductance decreases the possibility of overestimating the motor characteristics. This is one example showing that for an accurate modeling a true 3D FEM should be used.

7.2 Modeling of the flux fringing in the air gap

The flux fringing in the air gap is another problem for a 2D FEM model. The model assumes that there are no axial flux components, if the 2D plane is set as a cross section of the motor. In reality the flux fringes, especially at the air gap region. Thus the modeled flux density needed to calculate the electromagnetic torque is incorrect. Also, the magnetizing current goes wrong because of the incorrect air gap reluctance. Usually, this problem is solved by calculating an effective core length. The length of the motor is increased so that the average flux density is correct. The filling factors of core parts are decreased so that the flux density in the iron stays as it is.

Often, such a rule of thumb is used so that the length of the motor is increased with the value of the air gap at the each end of the core (Richter 1951). For example, a stator core of 100 mm with an air

gap of 1 mm would yield an effective length of 102 mm. More accurate solutions are discussed in the literature. Flack and Knight (2000) discuss several methods that can be used to model the radial ventilation ducts for large induction motors, from Carter's correction factor approach to full 3D models. The results were interesting as they pointed out that an analytical equation based on Carter's correction factor could yield almost the same results as a 3D FEM.

In the high-speed motors considered in this study, the flux fringing effect is strong. This is because the motors are relatively short compared to the air gap. For the copper coated rotor, this is especially important, as the iron-to-iron air gap is even larger. This was seen in Table 2.3. In addition, the use of a radial cooling duct in the stator doubles the flux fringing regions.

Usually, the effective length is calculated so that the average flux density of the fringed flux, normal to the stator and rotor surface, corresponds to the constant flux density in the region where the flux has only the normal component:

$$l_{\mathrm{eff}} = \frac{\int_{3\mathrm{D}} (\boldsymbol{B}\cdot\boldsymbol{n})\,dl}{\int_{2\mathrm{D}} B\,dl}\, l_{2\mathrm{D}}\,, \tag{7.4}$$

where $\boldsymbol{n}$ is the unit vector normal to the integration path. This definition for the effective length should give a good estimation for an air gap permeance and the magnetization reactance.

Estimation of torque per slip characteristic is important for solid steel rotors. A low slip operation is needed in order to avoid extensive saturation and iron loss in the rotor. The problem in the calculation of effective length is that the magnetization reluctance and the torque cannot be correct at the same time. The air gap torque depends on the square of the flux density (Arkkio 1987):

$$T_{\mathrm{e}} = \frac{l_{\mathrm{eff}}}{\mu_0 (r_{\mathrm{s}} - r_{\mathrm{r}})} \int_{S_{\mathrm{ag}}} r B_r B_\varphi \, d\boldsymbol{S}\,, \tag{7.5}$$

where μ_0 is the permeability of vacuum and r_{s} and r_{r} are outer and inner radii of the air gap, respectively. B_r and B_φ are radial and tangential components of magnetic flux density, respectively. The linear averaging gives values which are too large for l_{eff}. If a more accurate estimation for the air gap torque is needed, the effective length has to be calculated as proportional to the average of the square of the flux density:

$$l_{eff} = \frac{\int_{3\mathrm{D}} (\boldsymbol{B}\cdot\boldsymbol{n})^2 dl}{\int_{2\mathrm{D}} B^2\, dl}\, l_{2\mathrm{D}} \tag{7.6}$$

To approximate the flux fringing for the high-speed motors, 2D FEM software FEMM (Meeker 1999) was used in a similar fashion as was previously used for the end ring inductance. Fig. 7.2 shows a cross-section of the motor with a copper coated solid steel rotor. The magnetic field is induced by the currents at the stator end windings. A planar co-ordinate system is used. The Neumann boundary condition is set on the symmetry axis of the rotor. An artificial flux path was built to model the back iron of the stator and to close the path between the rotor symmetry axis and the stator core. Figs. 7.3 and 7.4 show the air gap flux distribution close to the stator and rotor surfaces. The long air gap smoothens the stator flux peaks and the peaks are not visible at the rotor side.

Table 7.1 shows the results for the calculation of the effective length. The calculations were done using different integration paths. The first integration was done from the end of one end ring to another. Only a small part of the fringing flux was left out. All the flux was captured by integrating from one end of the rotor to another. The result of the linear averaging (Eq. 7.4) was slightly different when the different integration paths were used. The change of a path did not affect the quadratic averaging result (Eq. 7.6) significantly, since the square of the flux is small beyond the end rings. The integration path was close to the rotor surface.

The results show how the real iron core length of the stator l_{ic} is significantly smaller than the approximations for the effective length. This is a good example of how 3D effects make straightforward 2D modeling difficult.

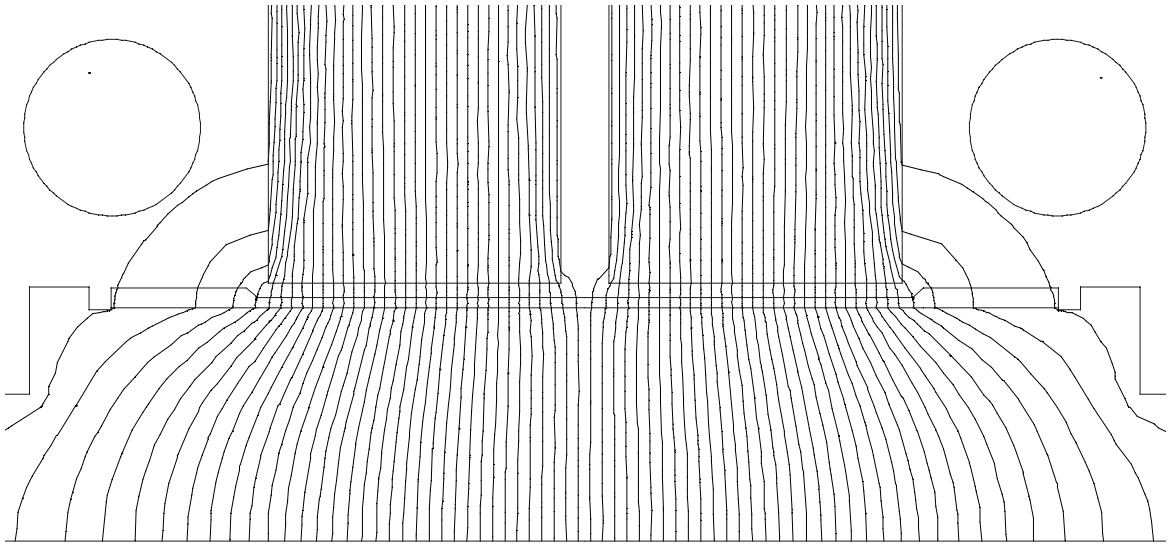

Fig. 7.2 A zoomed picture of a 2D FEM model to approximate the flux fringing.

Table 7.1 Calculated effective length for a high-speed motor with a copper coated solid rotor.

	$l_{eff} = l_{ic}$	$l_{eff} = l_{ic} + 4\delta_g$	2D FEM, linear[1)]	2D FEM, quadratic[2)]
Effective length l_{eff} [mm]	108.0	127.6	128.9 - 131.8[3)]	117.2

[1)] An average of flux across the integration path (Eq. 7.4)

[2)] A average of flux squared across the integration path (Eq. 7.6)

[3)] The smaller value; integration path from end-ring to end ring. The bigger value; integration along the whole rotor

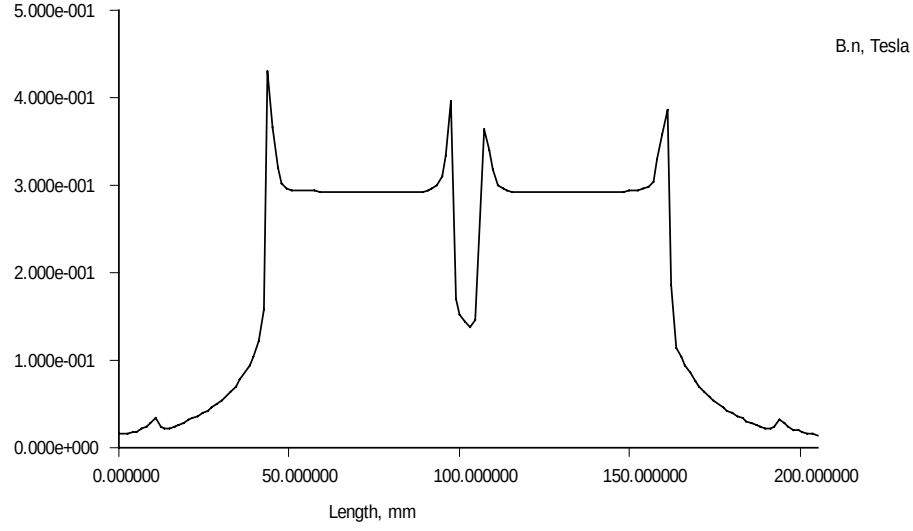

Fig. 7.3 The air gap flux density distribution close to the stator core.

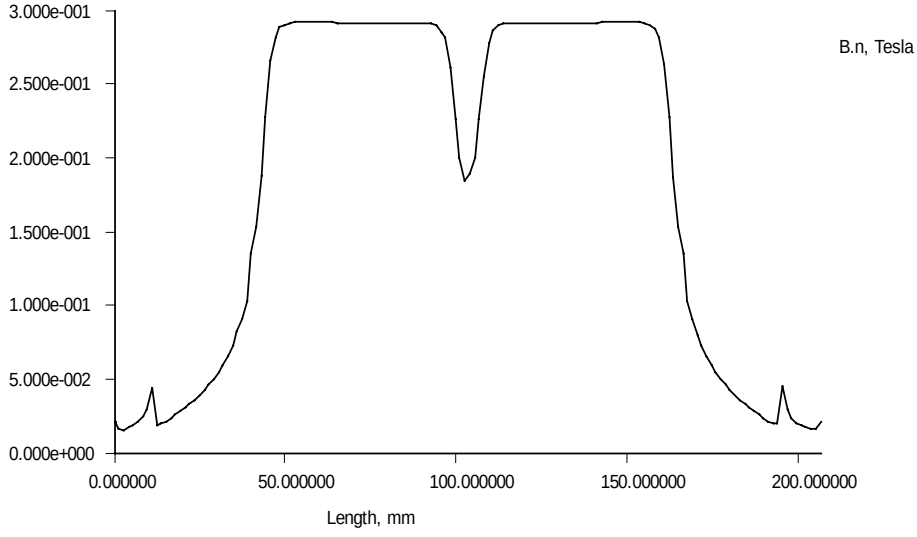

Fig. 7.4 The air gap flux density distribution close to the rotor surface.

7.3 Calculations for the motor with a copper coated rotor

One of the goals in the research project was to compare the calculated and measured results of the high-speed motors in order to find out the feasibility of the models. The results of a comparison for the 60 kW 60000 $^{1}/_{\text{min}}$ motor with a copper coated solid steel rotor are presented here. The measurement setup and the results were discussed in Chapter 5.

The motor characteristics were calculated using the electromagnetic model described in Appendix A, with the modifications presented in this chapter. The impedance of the end ring was calculated using the 2D FEM as explained in Section 7.1. The flux fringing was also taken into account using a 2D FEM model. The results of the linear and quadratic approximation for the effective length were used. The values for the effective length were shown in Table 7.1. The two different linear approximations yielded nearly the same results. The results given by the linear approximation with a shorter integration path are shown in the following comparison.

The electromechanic characteristics were calculated using the time stepping method and second order finite elements. The finite element mesh consisted of 3620 elements and 7313 nodes. Four periods of supply frequency were modeled. Each period was divided into 360 steps, making a total of 1440 steps. The values of the characteristics were calculated using the measured values for the slip. The measured temperatures were used to modify the resistivities of the stator winding, copper coating and solid steel. The amplitude of the fundamental voltage measured was used to scale ideal PAM waveforms as a supply voltage.

Fig. 7.5 shows the measured and calculated stator current as a function of the input power. The linear approximation for l_{eff} is better suited for the estimation of the air gap permeance and the magnetization reactance. It yields a result closer to the measured values. The quadratic approximation leads to overestimation of the current.

A similar result comes from the comparison of the measured and calculated power factors. In Fig. 7.6, the values of the measured power factor are determined from the input voltage, current and power. The linear approximation of l_{eff} gives results close to the measured ones. The quadratic approximation leads to an underestimation of the power factor.

Fig. 7.7 shows that the quadratic approximation of l_{eff} models well the torque-slip curve. In this case, the linear approximation leads to an underestimation of the torque. Thus, the quadratic approximation could be used for torque and the linear approximation for current and power factor.

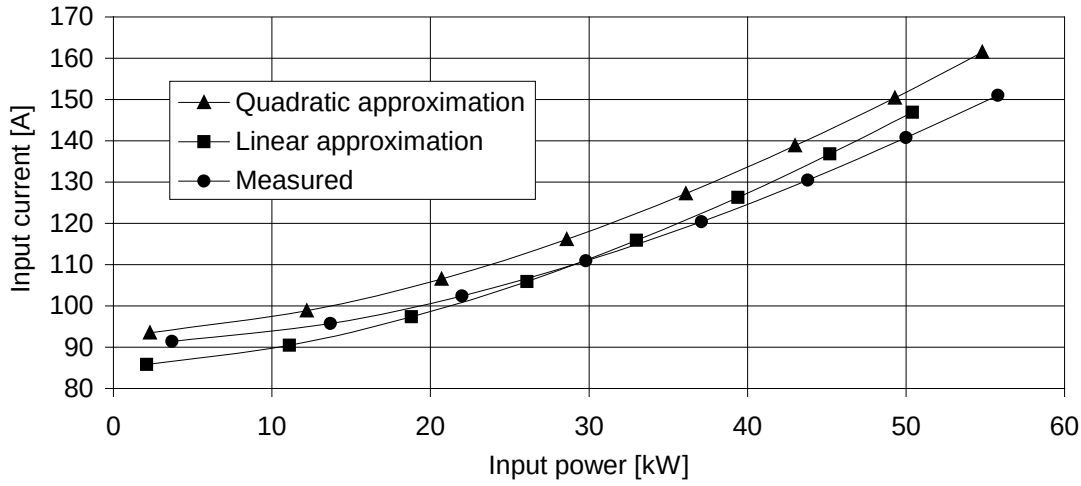

Fig. 7.5 Stator current measured and calculated.

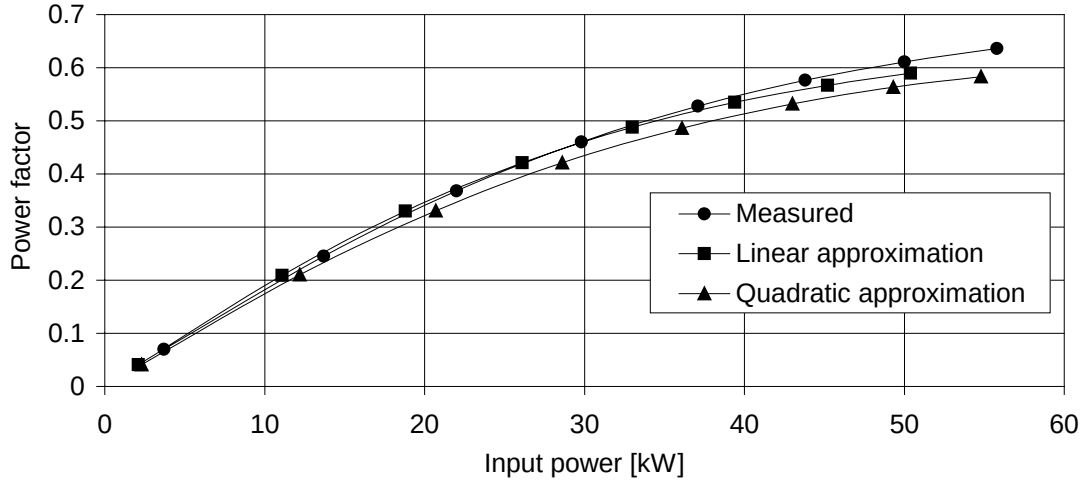

Fig. 7.6 Power factor measured and calculated.

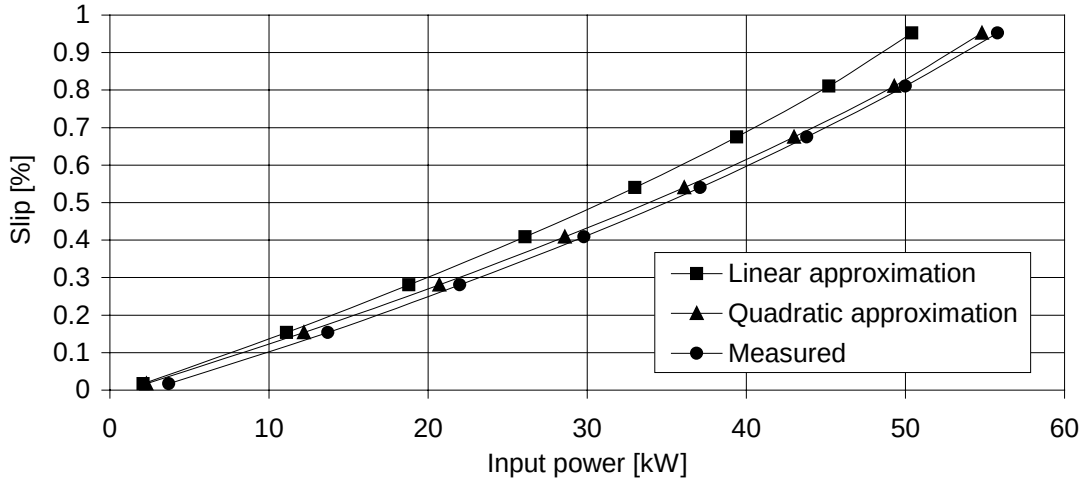

Fig. 7.7 Slip measured and calculated.

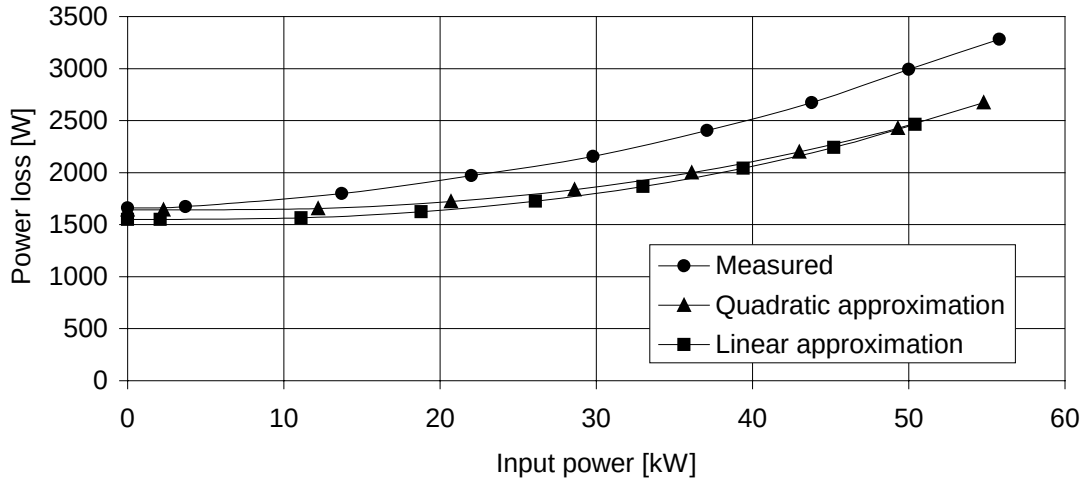

Fig. 7.8 Electromagnetic loss measured and calculated.

Considering the results shown in Figs. 7.5 – 7.7, it seems that the electromechanic characteristics can be modeled and estimated reasonably well. One of the reasons for this is that the temperature rise of the rotor was known. However, Fig. 7.8 shows that the calculation of electric loss goes wrong. At no-load, the calculations agree well. However, as the loading increases the calculated results underestimate the power loss independent of the determination of the effective length. It seems that some loss components or loss phenomena depending on the stator current are not modeled correctly or not taken into account. This issue is studied further in the next chapter.

7.4 Conclusion

A 2D finite element method was modified to take some 3D effects into account. Separate 2D FEM models were used to calculate the end ring inductance and the effective length of the motor. The value of the end ring inductance was increased as the solid iron core was present in the field solution.

The effective length was approximated in two different ways. In the linear approximation, the length is a function of average air gap flux density. This approach emphasizes the correct calculation of magnetization inductance. In the quadratic approximation, the length is a function of the average of the flux density squared. This approach emphasizes the correct calculation of torque.

Comparison of calculated and measured results agreed quite well. The only major difference was in electromagnetic loss measured and calculated.

8 CIRCULATORY CURRENTS IN A STATOR WINDING

The difference between the electromagnetic power loss measured and calculated in Section 7.3 was disturbing. The difference seemed to be a function of the input current or load of the high-speed induction motor. At the nominal operation point, the model used in the calculations underestimated the loss by almost 20%. This raises questions about the usability of the model in designing and optimization of the high-speed machines.

Circulatory currents in the filamentary stator windings were suspected as a possible reason for the difference in the results. These currents can flow in parallel strands and paths of a filamentary conductor winding. This would mean an increased loss in a stator winding. The loss component would be a function of current in the same way as is the discrepancy in the results of comparison mentioned above. Thus, the high-speed motor in question was disassembled for the measurement of the possible circulatory current effect. Fig. 8.1 shows the stator prepared for the measurement.

The reason for the circulatory currents is the magnetic flux penetrating the windings inside the stator slots. The flux causes eddy currents that change the current density distribution in the parallel strands. The amplitude and the phase angle of the currents in parallel conductors are different from each other.

In the FEM model used, the current density in the stator winding is assumed to be constant. The eddy-current loss is modeled separately from the field solution by using Eq. A11. Thus, the circulatory currents in the parallel strands and paths of the filamentary winding are not modeled. In order to model the filamentary winding precisely, every individual strand should have its own voltage equation (Eq. A3) solved together with the field solution. Doing this kind of model is difficult. Every strand should be meshed in detail. As there can be thousands of strands in the stator winding, the size of the model may become unfeasibly difficult to solve. Using macro elements as described by Szücs (2001) could decrease this size of the system of equations.

Even if solving the modeling problem is possible, one problem remains. The positions of the strands inside the slot of a manufactured machine are not known. Accurate and correct positioning of strands of a filamentary winding is considered expensive and time-consuming, if not impossible. This difference between modeling and reality will inherently generate a difference in calculated and measured results for the stator winding loss.

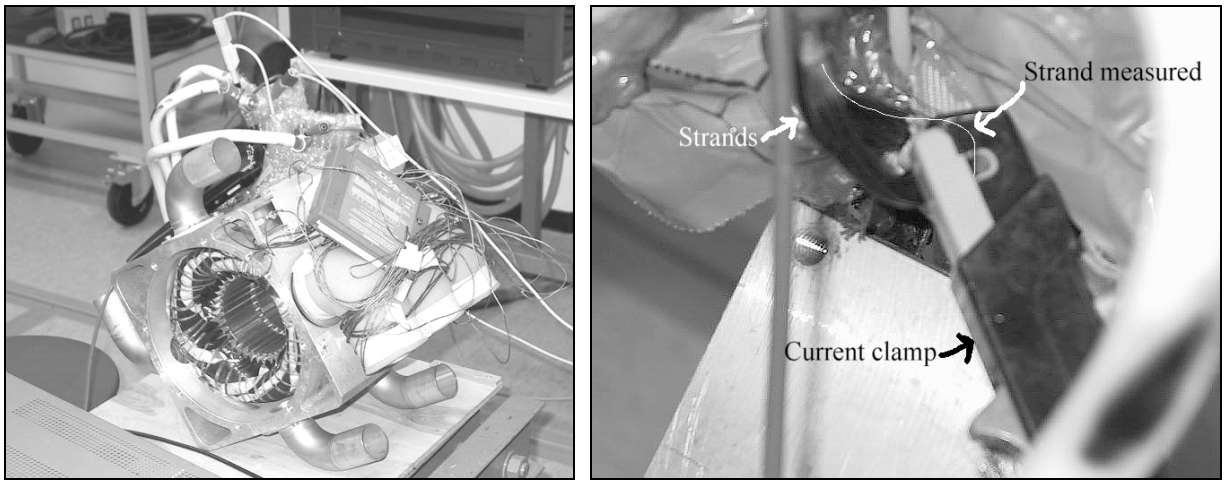

Fig. 8.1 Stator of the 60 kW 60000 $^{1}/_{\mathrm{min}}$ high-speed induction motor prepared for the individual strand current measurement. The rotor is taken away.

8.1 Measurement of strand currents of the filamentary winding

The strand currents were measured without the rotor, with three phase sinusoidal voltage and at different frequencies. Synchronous generator was used to produce the voltage. In the measurements, constant current amplitude was maintained. Individual strand currents and their phase angle relative to a reference signal were measured. One phase-to-phase voltages was selected as a reference signal. The measurement setup is illustrated on the left hand side of Fig. 8.6.

The strand currents were measured with a current clamp meter. The model of the current meter amplifier was a Tektronix tm502a and the model of the current clamp probe was an AM503. Fig. 8.1 shows the current clamp probe and the strands taken out from inside the insulation layers. The current meter signal and the reference signal were synchronously sampled at 10 kHz and post processed using a MBC-11 control board made by HST Ltd. The average temperature of the phase winding was measured at frequent intervals with a DC-resistance method.

Table 8.1 shows the measured circulatory current loss coefficient k_{cc} for the phase windings and the whole three phase winding at different frequencies. The coefficient is defined as

$$k_{\mathrm{cc}} = N_{\mathrm{s}} \frac{\sum_{n=1}^{N_{\mathrm{s}}} \left| \underline{i}_n \right|^2}{\left| \sum_{n=1}^{N_{\mathrm{s}}} \underline{i}_n \right|^2} = \frac{P_{\mathrm{cc}}}{P_{\mathrm{ed}}}, \tag{8.1}$$

where N_{s} is the number of parallel strands and $\underline{i}_n$ is the complex value of the current in strand n. The loss factor is then equal to the ratio of loss produced in the case where circulatory currents exists P_{cc}

Table 8.1 Circulatory current loss coefficient k_{cc} measured at different frequencies.

	15 Hz	50 Hz	150 Hz	300 Hz	450 Hz
Phase U	1.001	1.005	1.042	1.159	1.340
Phase V	1.001	1.008	1.069	1.257	1.527
Phase W	1.001	1.003	1.029	1.113	1.246
Average for the stator winding	1.001	1.005	1.047	1.176	1.371

relative to the situation where the sum of the current is equally divided between the strands P_{ed}. The latter loss is essentially the loss calculated by the present FEM model.

In the stator winding measured, there are two parallel coils in each phase. Each coil has 100 conductors or strands in parallel. Figs. 8.3 – 8.5 show the measured strand currents of the phase windings at 15, 150 and 450 Hz respectively. It can be seen how the individual strand currents start to have a different amplitude and phase angle as the frequency increases.

Fig. 8.2 shows the circulatory part of the loss coefficient ($k_{cc} - 1$), which seems to be proportional to the square of frequency. The difference in coefficients between the phases is quite large. This and Figs. 8.3 – 8.5 show how the randomness of the winding leads to the asymmetric properties of the phases. There are also significant differences between the parallel paths of the same phase.

The circulatory current coefficient can be reduced with a careful and consistent manufacture process. The positions of the strands and parallel paths are rotated inside the slot and between the slots. For example, a single strand would lie on a slot bottom region in one slot and in a slot opening region in the next slot. The idea is to have equal flux linkages for each strand and parallel path. However, this kind of systematic process may increase the cost of the winding.

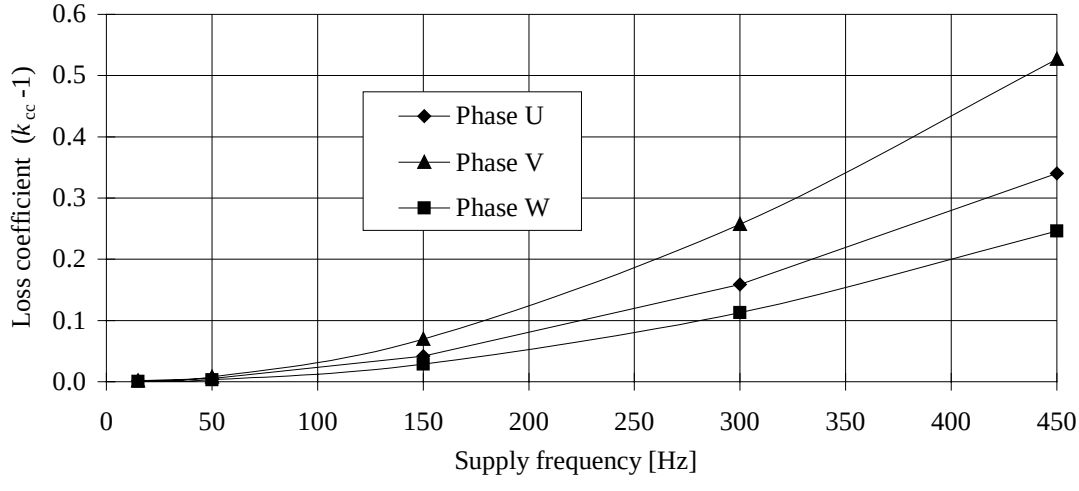

Fig. 8.2 Circulatory parts of the current coefficients k_{cc} of the phases of the stator winding.

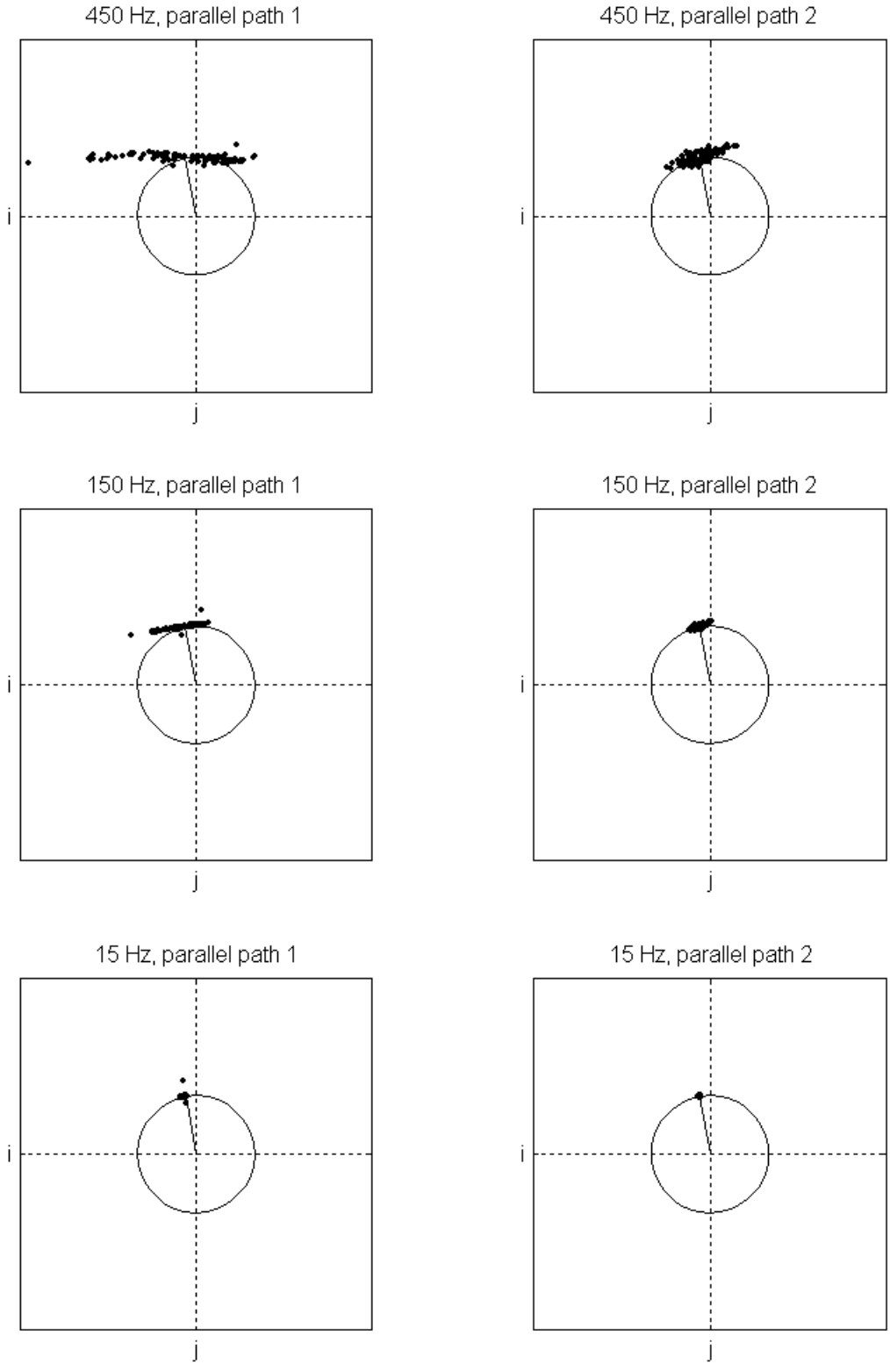

Fig. 8.3 Strand currents in the two parallel paths for phase U in complex coordinate system. Circles show the amplitude of the average strand current. Line shows the direction of average current.

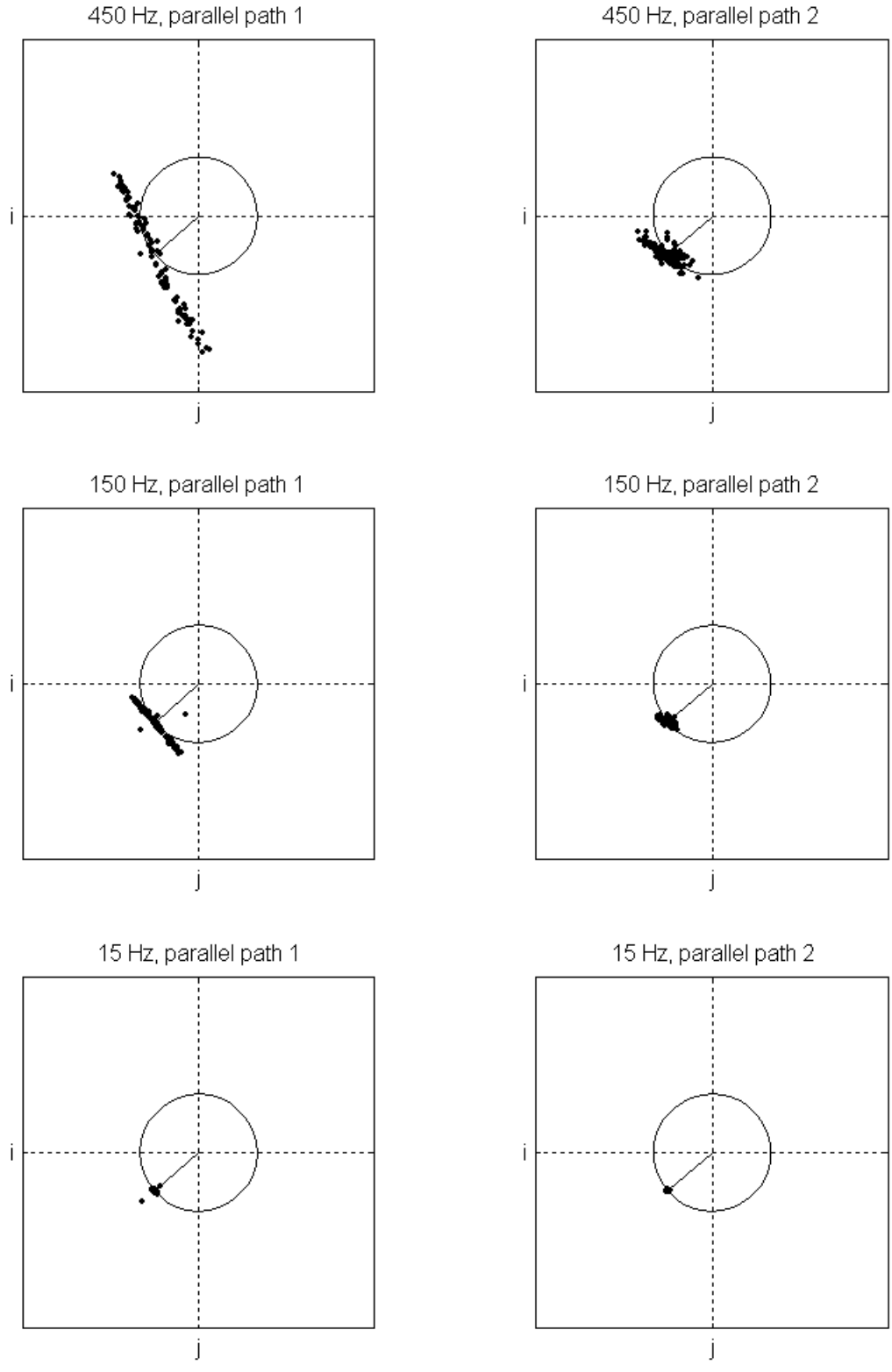

Fig. 8.4 Strand currents in the two parallel paths for phase V in complex coordinate system. Circles show the amplitude of the average strand current. Line shows the direction of average current.

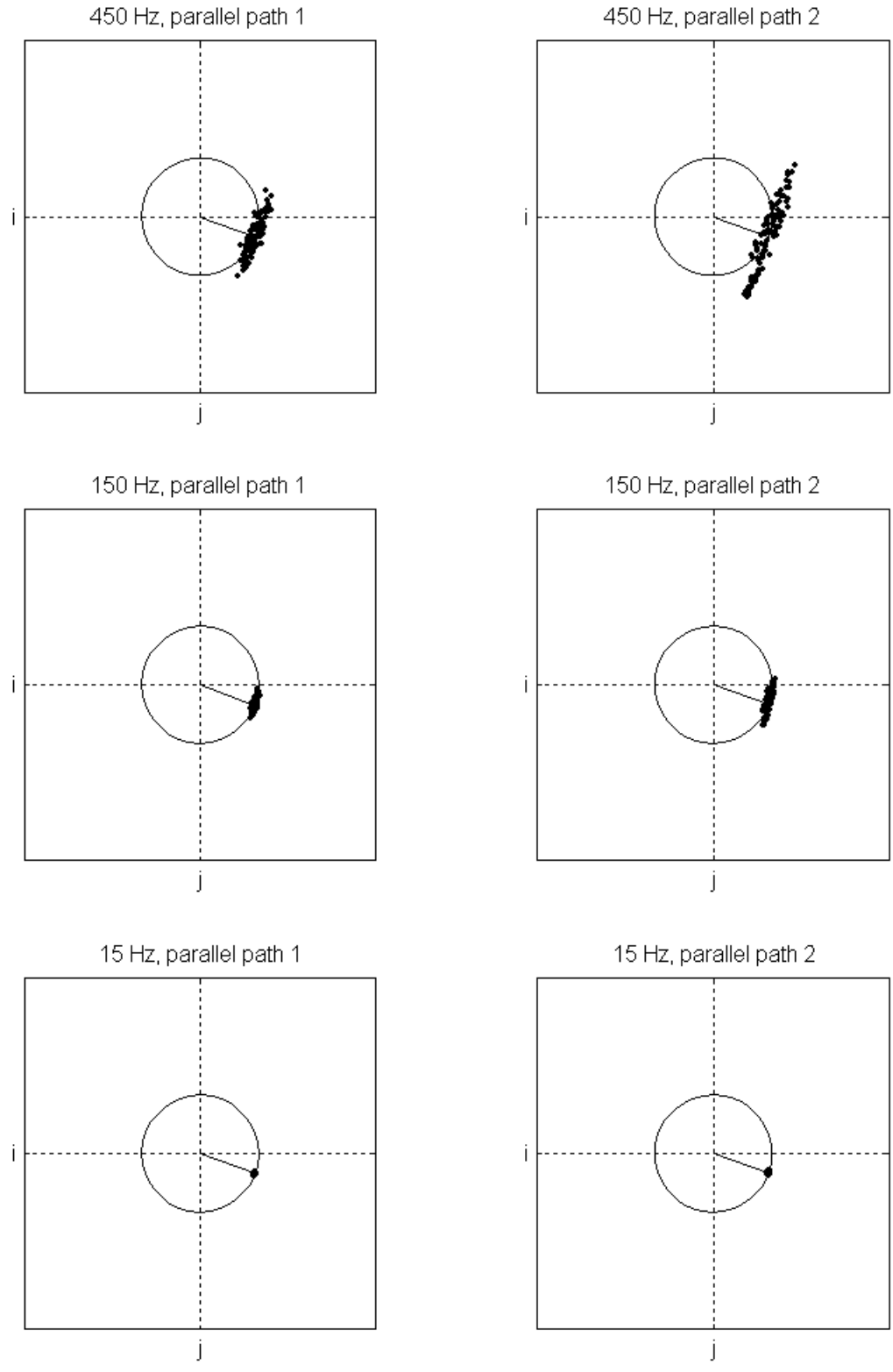

Fig. 8.5 Strand currents in the two parallel paths for phase W in complex coordinate system. Circles show the amplitude of the average strand current. Line shows the direction of average current.

8.2 Impedance of the circulatory current loop

The impedance of a circulatory current loop was also measured as a function of frequency. This was done in order to see whether the frequency of the circulatory current would affect the load impedance it sees. The impedance was measured by selecting two individual strands. The strands were disconnected from the terminal end. Thus, the current had a path from one strand end to the star connection and back along the other strand. A sinusoidal test signal was produced with an arbitrary waveform generator, a Sony/Tektronics AWG2005. The signal was amplified with a Kepco bipolar operational amplifier. Voltage, current and phase shift between them was measured. The phase shift was read from a HP 54600A scope. The current amplitude of the signal was selected to correspond roughly to the strand current in a nominal operation point of the high-speed motor. The measurement setup is illustrated on the right hand side of Fig. 8.6.

Fig. 8.7 shows the measured impedance and load angle or the phase shift between voltage and current of the circulatory current loop. The result shows that the impedance is mainly resistive up to the frequency of 10 kHz. For the 60 kW 60000 $^{1}/_{\text{min}}$ high-speed motor, a significant part of the harmonics spectrum lies within this region. As the emf inducing the currents is proportional to the frequency and the impedance can be assumed constant up to 10 kHz, the circulatory current loss produced becomes proportional to the square of the frequency.

The result implies that moving the harmonic components of the supply voltage and current up in the frequency range will increase the loss relative to the current because of the circulatory currents. This may degrade the benefits of using pulse width modulation as opposed to pulse amplitude modulation. This will be discussed more in Section 8.5.

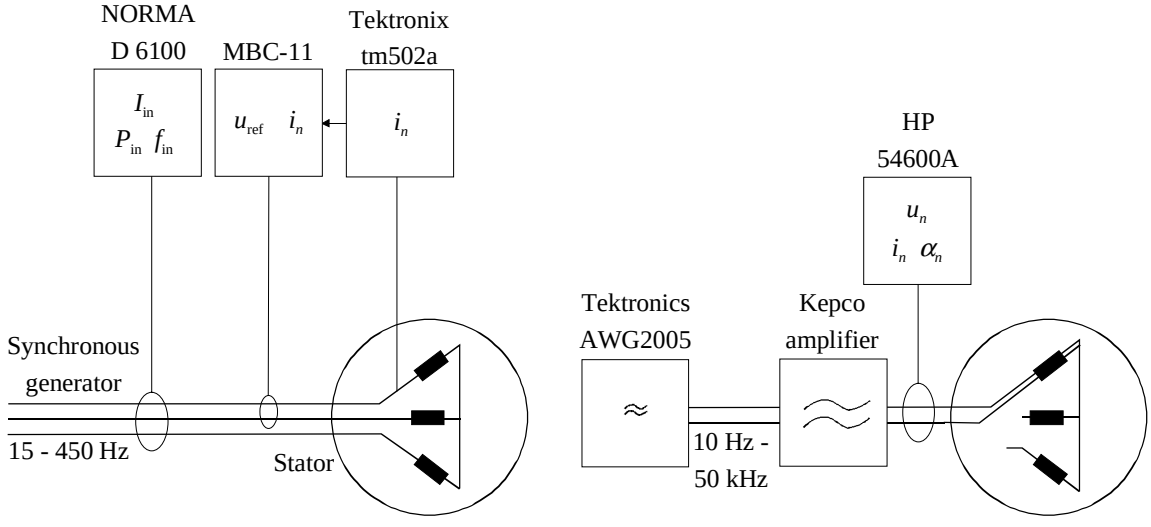

Fig. 8.6 On the left, the measurement setup for strand currents. On the right, the measurement setup for impedance and load angle of a circulatory current loop.

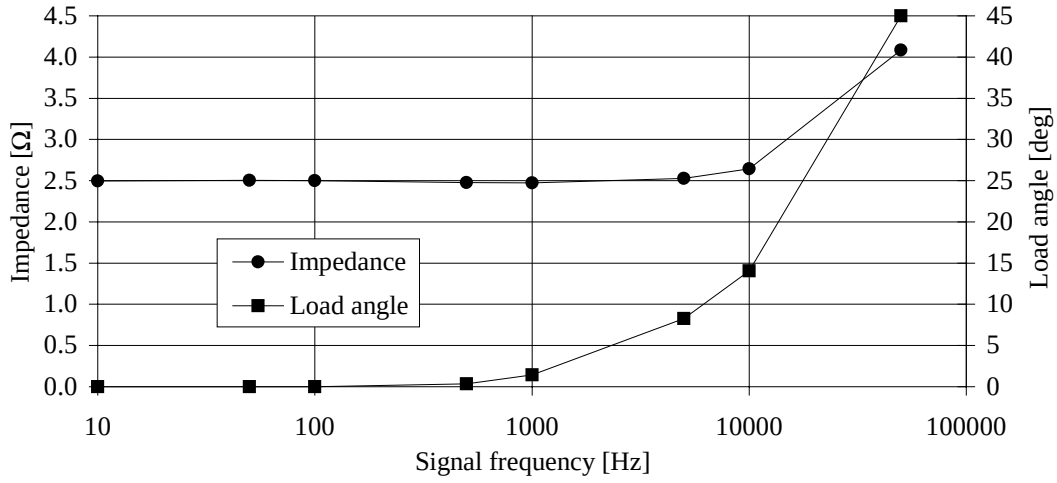

Fig. 8.7 Impedance and load angle of a circulatory current loop.

8.3 Estimation model for winding loss coefficient

The sinusoidal voltage supply used in the measurement of the strand currents could only be used up to 450 Hz. This was a problem since the high-speed motor was measured and calculated at the supply frequency of 835 Hz. In order to estimate the circulatory current loss factor k_{cc} for the stator winding at that frequency, a model for the circulatory current was formulated. The model would be able to predict the value of k_{cc} at any frequency and temperature based on a single reference measurement. The model was tested with the measured data to see if it worked and then it was used to approximate k_{cc} at 835 Hz.

If a circulatory current loop similar to the loop measured in the previous section is considered, the following voltage equation can be written:

$$e_{cc} = \int_l \boldsymbol{E} \cdot d\boldsymbol{l} = -\frac{d\Phi_l}{dt} = 2R_n i_{cc} + L_l \frac{di_{cc}}{dt} \ , \tag{8.2}$$

where e_{cc} is the circulatory current emf equal to the electric field strength $\boldsymbol{E}$ integrated around the loop $\boldsymbol{l}$. Φ_l is the magnetic flux passing through the loop, L_l is the self-inductance and i_{cc} is the circulating loop current. R_n is the resistance of one of the parallel conductors in the loop.

If the parallel strands were ideally wound in the slots and end winding regions, e_{cc} would be insignificant and no circulatory currents would be induced.

The results of the loop impedance measurement showed that the impedance seen by e_{cc} is almost constant in the frequency region for the main harmonics currents of the 60 kW 60000 $^1/_{min}$ high-speed motor. If the impedance is assumed resistive, the last term from Eq. 8.2 can be omitted.

Because Φ_l is approximately at the same phase as the average coil current $\underline{i}_{ave}$ in the conductors, the circulatory current $\underline{i}_{n,cc}$ of a conductor n then has 90° phase shift compared to $\underline{i}_{ave}$ and

$$\underline{i}_{n,cc} = \left(\underline{i}_n - \underline{i}_{ave}\right) \propto \frac{e_{cc}}{R_n} \propto \frac{f}{R_n} \ . \tag{8.3}$$

This means that $\underline{i}_{n,cc}$ is proportional to the frequency f as a result from Eq. 8.2, and inversely proportional to the resistance of a strand. According to the assumptions there should be 90° phase shift between $\underline{i}_{n,cc}$ and $\underline{i}_{ave}$. This is illustrated on the left hand side of Fig. 8.8.

Figs. 8.3 – 8.5 show that the measured results agree on this, especially at low frequencies. The strand current points tend to lie in a plane perpendicular to the average strand current vector. At 450 Hz the phase shift is no longer 90°. This indicates that the circulatory currents loop is no longer purely resistive.

The model used to estimate the circulatory current loss factor k_{cc} is based on the relation in Eq. 8.3. The idea in the model is first to have a reference measurement yielding a strand current distribution. The individual strand currents are divided into an average current part and a circulatory current path. Then the circulatory parts of the strand currents are scaled to another frequency and resistance. In practice, scaling the resistance means the scaling of temperature. The strand currents are then

$$\underline{i}_n = \underline{i}_{ave}^{ref} + \underline{i}_{n,cc}^{ref} \frac{R_n^{ref} f}{R_n f^{ref}} \ , \text{ where} \tag{8.4}$$

$$\underline{i}_{ave}^{ref} = \frac{1}{N_c} \sum_{n=1}^{N_c} \underline{i}_n \quad \text{and} \tag{8.5}$$

$$\underline{i}_{n,cc}^{ref} = \underline{i}_n^{ref} - \underline{i}_{ave}^{ref} \ . \tag{8.6}$$

However, it was found out that this division did not give very good estimations when the frequency of the estimated point was higher than that of the reference point. Instead, $\underline{i}_{n,cc}$ was divided into two components. The component to be scaled is the projection of $\underline{i}_{n,cc}$ into the plane of strand currents. The equation for the plane was numerically fitted into the strand currents data in a least-squares sense. Thus, the model takes into account the phase angle between the average strand current and circulatory strand current components.

$$\underline{i}_{n,cc}^{ref} = \underline{i}_{n,cc\parallel plane}^{ref} + \underline{i}_{n,cc\perp plane}^{ref} \quad \text{and} \tag{8.7}$$

$$\underline{i}_n = \underline{i}_{\text{ave}}^{\text{ref}} + \underline{i}_{n,\text{cc}\perp\text{plane}}^{\text{ref}} + \underline{i}_{n,\text{cc}\parallel\text{plane}}^{\text{ref}} \frac{R_n^{\text{ref}} f}{R_n f^{\text{ref}}} = \underline{i}_{\text{ave}}^{\text{ref}} + \underline{i}_{n,\text{cc}\perp\text{plane}}^{\text{ref}} + k_{\text{sc}} \underline{i}_{n,\text{cc}\parallel\text{plane}}^{\text{ref}}, \tag{8.8}$$

where k_{sc} is the scaling factor for the change in frequency and resistance. The right hand side of Fig. 8.8 shows the components of the strand vector used in this model.

Table 8.2 shows the measurement results for the first parallel path of the phase winding V. The circulatory current loss factors k_{cc} and scaling factors k_{sc} measured are given. The strand current distributions were shown in the left hand column in Fig. 8.3. The phase winding was measured at two temperatures at 450 Hz. In the 'hot' measurement, the average temperature of the winding was 100.5 °C. In other measurements the temperature was 23 – 26 °C. The effect of temperature on the scaling factor can be seen when comparing the data of the two measurements at 450 Hz.

Table 8.3 shows the results of the estimation of k_{cc} with Eq. 8.8. It seems to give good approximations for k_{cc}. It can be seen that for $k_{\text{sc}} > 1$, the model seems to overestimate k_{cc}. For $k_{\text{sc}} < 1$, the model seems to underestimate k_{cc} in some cases. However, based on these results, it can be said that the model for estimating the strand current distribution and k_{cc} works quite well.

The left side of the graph in Fig. 8.9 shows how the strand current distribution is estimated up to 450 Hz, based on the data measured at 15 Hz. It shows how the estimated distribution is slimmer and wider than the real distribution. The value of k_{cc} is overestimated by 10 %. This is a relatively small error when considering the length of the extrapolation.

The right side of the graph in Fig. 8.9 shows how the strand current distribution is estimated down to 15 Hz, based on data measured at 450 Hz. It shows how the estimated distribution is close to the real distribution. The estimated value of k_{cc} is almost equal to the measured value.

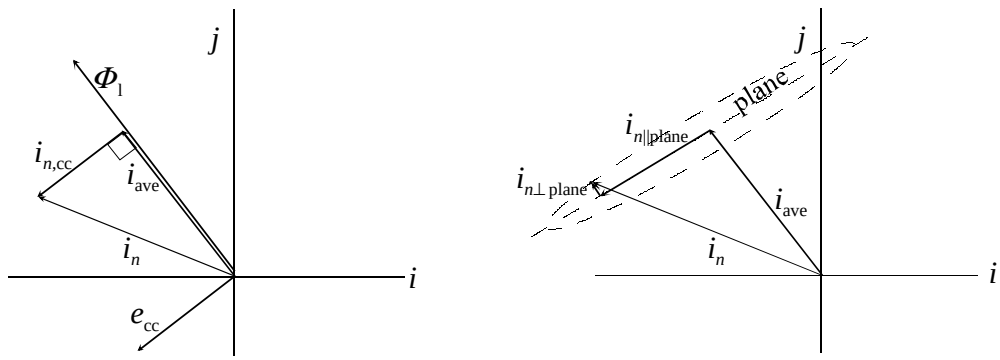

Fig. 8.8 Vector diagrams for strand currents. On the left, initial approach from Eqs. 8.2 and 8.3. On the right, current component division according to the estimation model, Eqs. 8.6 and 8.7.

Table 8.2 Circulatory current loss coefficients k_{cc} and scaling factors k_{sc} measured for phase V.

		k_{cc} at f^{ref}	k_{sc}					
			15 Hz	50 Hz	150 Hz	300 Hz	450 Hz, hot	450 Hz
Estimation frequency f^{ref}	15 Hz	1.002	xxx	0.30	0.01	0.050	0.045	0.033
	50 Hz	1.015	3.31	xxx	0.33	0.17	0.15	0.11
	150 Hz	1.132	10.05	3.03	xxx	0.50	0.45	0.34
	300 Hz	1.485	20.06	6.05	2.00	xxx	0.90	0.67
	450 Hz, hot	1.578	22.26	6.71	2.21	1.11	xxx	0.74
	450 Hz	1.984	29.96	9.03	2.98	1.49	1.35	xxx

Table 8.3 Circulatory current loss coefficient k_{cc} estimated at different frequencies for phase V.

		k_{cc} estimated / error-%					
		15 Hz	50 Hz	150 Hz	300 Hz	450 Hz, hot	450 Hz
Estimation frequency f^{ref}	15 Hz	xxx	1.00 / 0	1.00 / 0	1.00 / 0	1.00 / 0	1.00 / 0
	50 Hz	1.02 / 0	xxx	1.02 / 0	1.02 /0	1.01 / 0	1.02 / 0
	150 Hz	1.13 / 0	1.13 / 0	xxx	1.12 / -1	1.12 /-1	1.11 / -2
	300 Hz	1.53 / 3	1.52 / 2	1.51 /2	xxx	1.47 / -1	1.44 / -3
	450 Hz, hot	1.65 / 5	1.64 / 4	1.63 / 3	1.60 / 1	xxx	1.54 /-2
	450 Hz	2.18 / 10	2.16 / 9	2.14 / 8	2.08 / 5	2.05 / 3	xxx

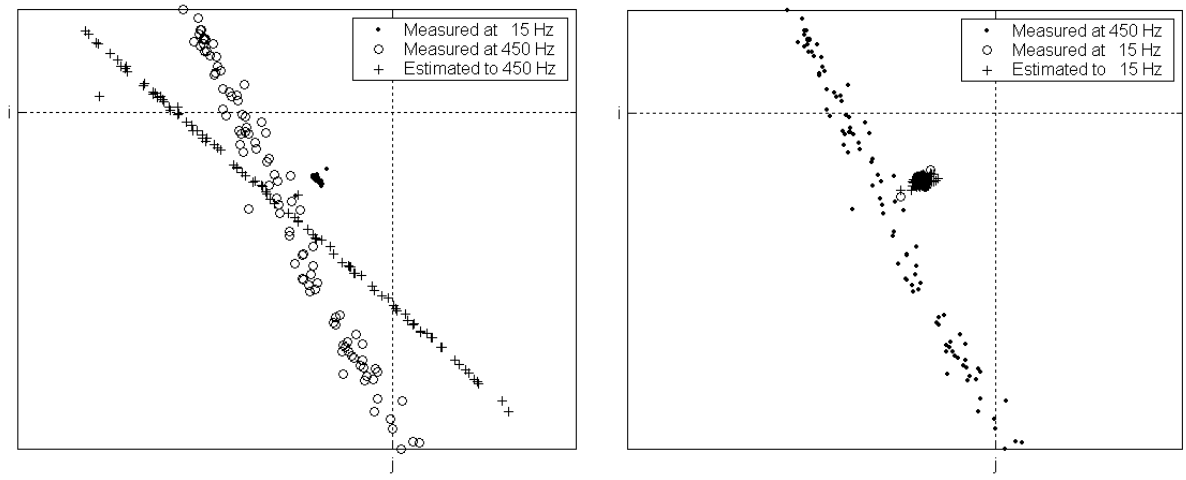

Fig. 8.9 Estimated strand current distributions for parallel path 1 in phase V. On the left, estimation based on the data measured at 15 Hz. On the right, estimation based on the data measured at 450 Hz.

8.4 Calculations for the motor with a copper coated rotor

In Chapter 7, the measured and calculated results for the high-speed motor with a copper coated rotor were compared. The results of the comparison showed that the electromagnetic loss was underestimated in the calculations. The error increased with increasing input current and input power.

As no measurements for the circulatory current coefficients could be made at 835 Hz, the estimation model presented in the previous section was used. The reference data for the estimation was the strand current data at 450 Hz.

The stator winding losses calculated were adjusted with the circulatory current loss factor k_{cc}. Table 8.4 shows the values for the phases and the average value at full load. The average value was used in the calculations. Different values for k_{cc} were used at different load points because the resistance and thus k_{sc} changes along with the temperature. The value of average k_{cc} was between 1.69 – 1.83, depending on the load.

Only the loss factor of fundamental frequency was calculated. Thus, the adjustment is less than if the harmonic loss components were modified with their own factors. The model used to predict k_{cc} seemed to overestimate it when $k_{sc} > 1$. However, the length of extrapolation was small, $k_{sc} \approx 1.4$. According to the test data in the previous section, the error could be 3 – 5 %.

Calculations were done with linear and quadratic approximations for the effective length of the motor. These approximations were defined in Section 7.2. Fig. 8.10 shows that now the difference between the measured and calculated loss is relatively small. At the input power of 50 kW, the quadratic approximation underestimates the electromagnetic loss by 3 %. For the linear approximation, the loss is 5 % lower than measured. The calculations overestimate the loss at no-load. The quadratic approximation gives 11 % and the linear approximation 3 % higher loss than measured. Comparing Figs. 7.8 and 8.10, it can be seen that the circulatory currents can explain much of the difference between the calculated and measured electromagnetic loss. Especially, the difference's dependence on load or current is reduced.

Table 8.4 Circulatory current loss coefficient k_{cc} estimated at 835 Hz and at full load.

	Phase U	Phase V	Phase W	Average k_{cc} for the stator winding
450 Hz measured	1.340	1.527	1.246	1.371
835 Hz estimated	1.633	1.928	1.458	1.691

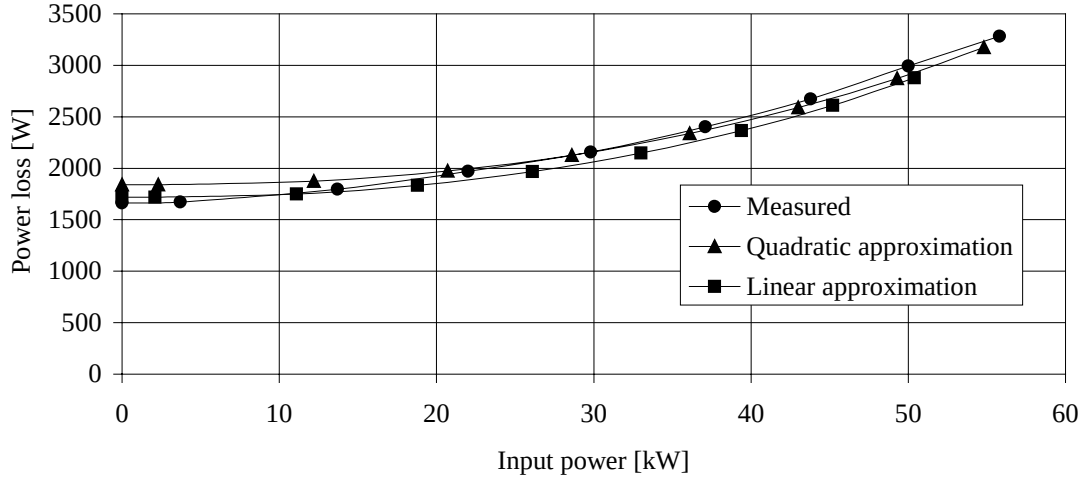

Fig. 8.10 Measured and calculated electromagnetic loss of the high-speed motor with a copper coated rotor. In the calculations, stator winding loss is multiplied with circulatory current loss factor k_{cc}.

Knowledge of the detrimental effect of circulatory currents can be used to improve the design of a stator and stator windings for high-speed machines. The unsymmetrical flux linkage of parallel strands or parallel paths should be minimized. This could be done by changing the dimensions of a stator slot so that the leakage flux through the slot is decreased. The windings should be wound so that all strands and paths have balanced positioning inside the slots as a whole. Using a Litz-wire could improve the winding or make the manufacture of a symmetrical strand distribution easier.

8.5 Effect of circulatory currents on harmonic loss

Circulatory currents influence the general frequency dependence of the electromagnetic loss. Eq. 2.5 in Section 2.4 showed that increasing the speed of a high-speed motor changes the balance between different loss components. Like eddy-current loss, circulatory current loss is proportional to the square of speed or frequency. Thus, a bigger share of the electromagnetic loss is frequency dependent than had been previously thought.

This result may affect the selection of voltage supply waveforms. Because of the frequency dependence of hysteresis, eddy current and circulatory current loss, the currents of a higher harmonic order produce more loss than the same amount of lower order harmonics. This was proven in the measurements for different supply voltage waveforms in Chapter 6.

The influence of circulatory currents on harmonic loss was studied based on the strand current distributions measured at 450 Hz. The loss coefficient k_{cc} was calculated separately for each harmonic order. The measured impedance curve (Fig. 8.7) for the current loops was taken into

account when calculating the scaling factor k_{sc}. The average temperatures measured for the windings in Chapter 6 were also taken into account. The estimation model presented in Section 8.3 (Eq. 8.8) was used to calculate the values for k_{sc}.

The current spectra measured in Chapter 6 were modified by square root of k_{cc}, thus yielding the effective current spectra for the power loss. Results for PWM with 15 pulses per half cycle and PAM are presented.

Fig. 8.11 shows the average value of k_{cc} for the three phase winding as a function of frequency. It is seen that the model gives very high values for k_{cc}. It is clear that the extrapolation from 450 Hz is inaccurate. It is reminded here that the frequency of the fundamental was already 835 Hz. The coupling between the current distribution, circulatory emf e_{cc} and temperature distribution is not present in the model. If the coupling was modeled, the k_{cc} curve in Fig. 8.11 might saturate at some higher frequency. Thus, the result on the effect of the circulatory currents is only qualitative.

Fig. 8.12 shows the current spectra measured at full load points. It shows that PAM has steadily decreasing amplitude for the components. The PWM has low amplitudes for 5^{th} and 7^{th} order harmonics but higher amplitudes at higher frequencies. The rms-values of the harmonic currents are 32.8 A for PAM and 20.6 A for the PWM, as measured in Chapter 6.

Fig. 8.13 shows the same spectra corrected with the square root of k_{cc}, yielding an effective current spectra for power loss. It shows how the higher order currents for the PWM have a major effect on total harmonic content. The rms-values of the effective harmonic currents are 175 A for PAM and 265 A for the PWM.

Using DC-resistance of the stator winding, the harmonic loss due to the circulatory currents is calculated. The effective currents would give harmonic loss of 800 W for PAM and 1870 W for the PWM. These loss values are much too high. The total harmonic loss measured in the motor was only 700 W for PAM and 770 W for the PWM.

Even if the values for k_{cc} and effective currents are too high at higher frequencies, the result shows that the circulatory currents could be one thing to decrease the usefulness of PWM for high speed induction machines. On the other hand, if the k_{cc} - curve shown in Fig. 8.11 saturates at higher frequencies, the situation might be different. The harmonic currents of 5^{th} and 7^{th} order could increase more relative to higher harmonics. Thus, PWM might win the comparison after all. This is an interesting issue and subject for further studies.

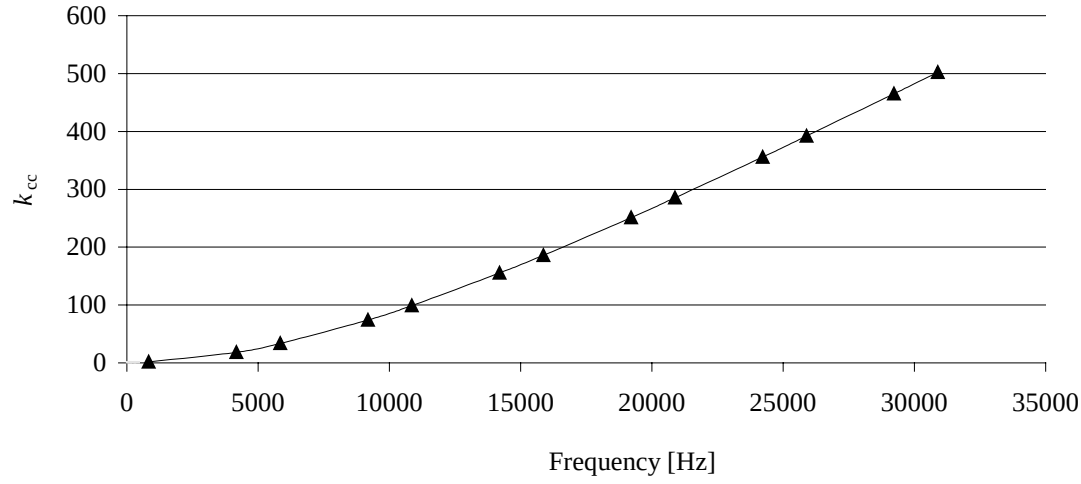

Fig. 8.11 k_{cc} estimated according to the model presented in Section 8.3.

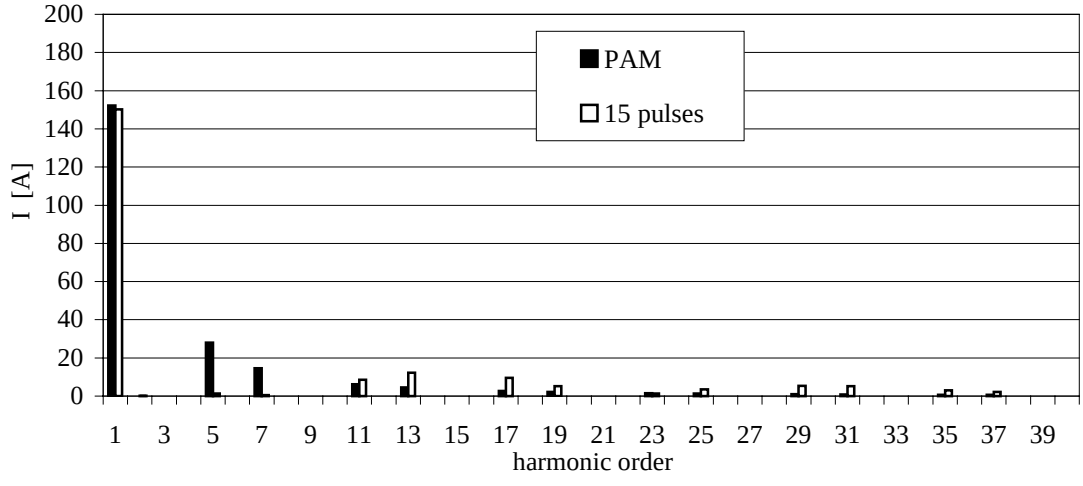

Fig. 8.12 Measured current spectra for PAM and PWM with 15 pphc.

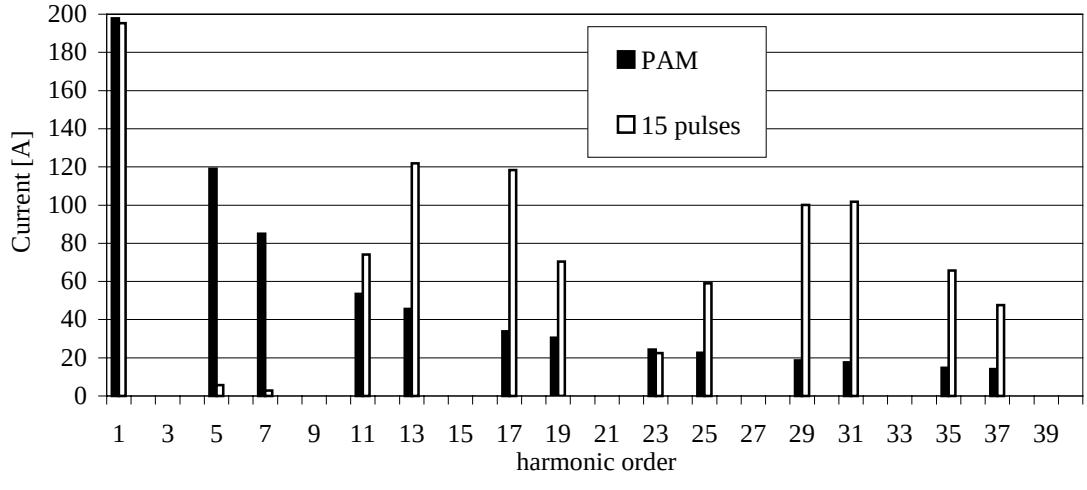

Fig. 8.13 Effective current spectra for PAM and PWM with 15 pphc.

8.6 Conclusion

Circulatory currents in the stator winding were suspected of causing some of the discrepancy between electromagnetic loss measured and calculated. Stator winding of a high-speed motor was prepared for the measurement of individual strand currents of the filamentary winding.

Circulatory current loss coefficients were measured at different frequencies up to 450 Hz with a sinusoidal input current. The measurement proved circulatory currents flowing in the parallel strands of the filamentary winding and causing significant power loss. At 450 Hz, the effective circulatory current loss factor was 1.37. This means a 37 % increase in power loss in the stator winding due to the circulatory currents.

A model to estimate the value of the loss coefficient at the frequency of 835 Hz was made. This is the supply frequency used in the measurements in Chapter 5. The estimated value for the effective circulatory current loss factor was used to scale the calculated values of the power loss in the stator winding. This was done for the motor with a copper coated rotor. After this scaling, the calculated electromagnetic loss agrees well with the measured one. Thus, taking the circulatory currents into account improves the validity of the model in the design and optimization of high-speed machines.

9 OPTIMIZATION OF SOLID STEEL ROTORS

In this work, numerical optimization was used to find suitable values for the design variables of a squirrel cage solid steel rotor. Computational optimization of the rotor design was performed. The 16 bar and the 26 bar rotors compared in Chapter 5 were already designed and manufactured but the existence of better designs was checked.

The rotor designs suitable for a high-speed induction machine were also studied in a more general fashion. The goal was to find designs that were electromagnetically advantageous. Numerical optimization was used to find these designs for the 60 kW 60000 $^{1}/_{\mathrm{min}}$ high-speed motor. Different topologies were given as initial designs and it was left to a genetic optimization algorithm to find the optimal designs. The algorithm is presented in Appendix C.

The optimization process can be very time consuming if numerical modeling is used. The FEM model used in this work belongs to that category. In the first section, an improvement for the optimization algorithms is suggested in order to reduce the computation times. The optimization cases and the results are presented later in this chapter.

9.1 Optimization of electric motors modeled with FEM

A genetic optimization algorithm (GA) was used to find solutions to the cases mentioned above. GAs have been studied and used for designing electric machines, such as in Palko (1996), Bianchi and Bolognani (1998) and Lampola (2000). Lähteenmäki (1997) used a GA with a model for high-speed electric motors. The model includes FEM for electromechanical calculations and/or thermal network software for the calculation of temperature rise and cooling and friction loss.

The numerical optimization process of an electric machine – or any device or problem – can be divided into three discrete items: an optimization algorithm, a numerical model for the optimization case and an objective function. The results of the optimization are subject to verification, which often means the building and testing of a prototype. This division of the optimization process is illustrated in Fig. 9.1.

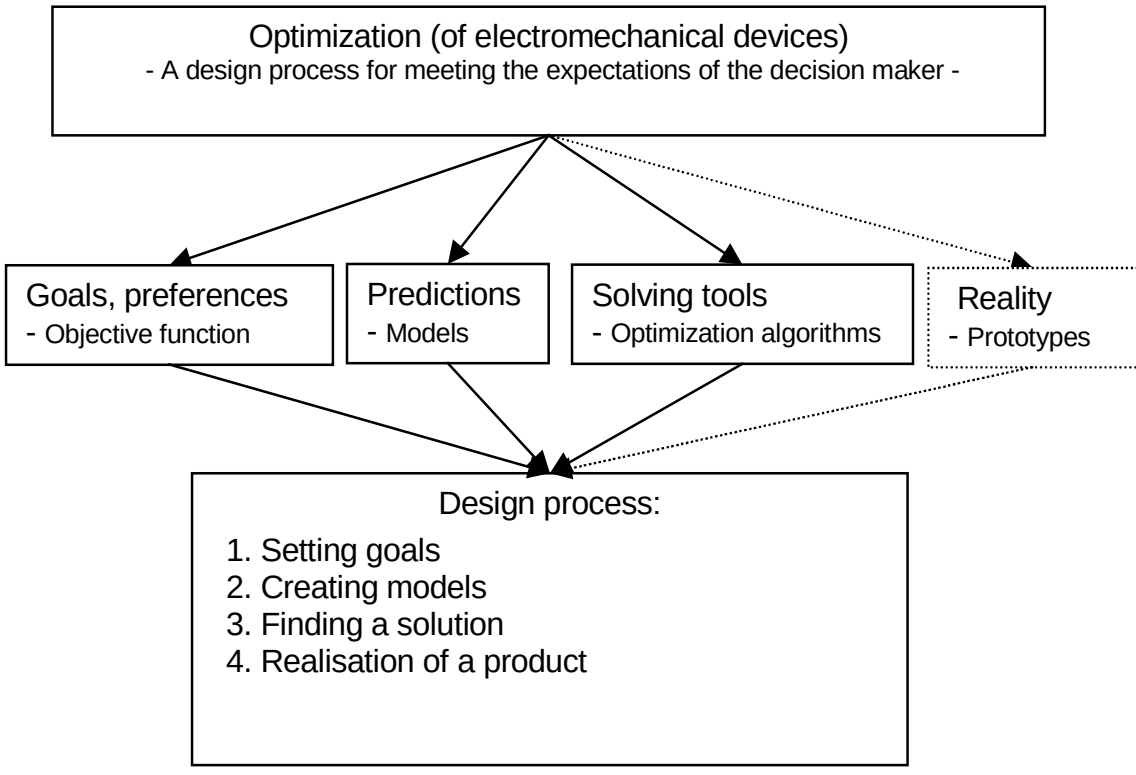

Fig. 9.1 Division of the optimization process into different tasks.

Heavy models are considered to be numerical models which take a considerable amount of time and efficient computers to solve. These models are not very informative as far as the needs of deterministic optimization algorithms are considered. They miss the analytical presentation and first and second order derivatives of the objective function are often used by the optimization algorithms. Finite differences can be used instead of derivatives, but that may lead to case specific tuning of algorithm specific parameters. Using a stochastic algorithm like GA is justified for the following reasons:

- The GA does not need the derivatives of an objective function. If the model includes a numerical computation such as in FEM, the objective function cannot be described explicitly as a function of the design variables. Hence, the derivatives of the function can only be estimated using finite differences. This is not good because the numerical model can include noise and the calculation of the finite differences means the calculation of many designs. Since the calculation of each design can take several minutes or tens of minutes, this should be avoided.
- The objective function describing the goodness of a design may have several local optima. As the algorithms based on a calculation of gradients or a Hessian matrix often converge to a local minimum, the global solution may not be found. The GA searches for the solution from the

whole solution space determined by the limits for the variables and other constraints. Thus, it is more likely that the global optimum is found.

- When designing new kinds of motors like high-speed motors, the optimal designs may be quite different from the conventional designs. The GA is not sensitive to the initial point of the design, which is often the case with the deterministic algorithms. The GA is more like an intelligent stochastic algorithm, combining the ‘freedom of prejudice’ of a stochastic algorithm with the ability of an deterministic algorithm to ‘concentrate on the relevant designs’.

The downside of using a stochastic algorithm is that it takes a large number of function evaluations to get the result. Using a heavy model like FEM means that each function evaluation takes several or several tens of minutes to calculate. In order to decrease the optimization times and make more use of the time spent, a practical improvement not found in the literature review is suggested. This improvement is applicable to any algorithm but it is most efficient when used with a stochastic optimization algorithm running a heavy model.

9.1.1 Combination of discrete search space and solution history

Solving heavy models like FEM can take most of the time used in optimization. In this work, the FEM model discussed in previous sections and Appendix A uses roughly 95 % of the computation time. Hence, the lower number of designs calculated the better. Unfortunately, this is contradictory to the nature of the stochastic optimization algorithms.

The idea of the discretization of the search space is to avoid evaluation of designs that are practically the same. For example, an induction motor with an air gap of 2.0 mm is no different from a motor with an air gap of 2.001 mm. The discretization should be selected so that the smallest difference between two designs is noticeable and realizable. In the above example, the machine produced would probably have the air gap somewhere near 2.0 ± 0.05 mm. Higher tolerances would be possible but not necessarily cost-effective.

For optimization algorithms using heavy models, the discretization is not a problem since the gradient and Hessian information of the objective function is unavailable anyway. Finite difference approximations could still be used. A proper discretization could actually improve the use of finite differences because of noise inherent in the models. However, the relation between discretization or relative perturbations and the accuracy of finite differences is a complicated issue (Palko 1996) and avoided by using stochastic algorithms.

Another way to decrease the number of function evaluations is to make sure that the same design is not evaluated more than once. The stochastic algorithms have no deterministic path to follow and the probability of calculating the same point several times in a discretized solution space exists. This phenomenon can be significant when using algorithms that concentrate their search on a portion of the solution space only. For example, the simulated annealing algorithm and GA used in this work does so to some extent.

In order to avoid repeated evaluation of the same design, a search or solution history can be used. The history data includes the free variables and the corresponding objective function value, but it can also include more information on the designs calculated. Every design evaluated is stored in the memory or in a file. The new designs to be evaluated are compared with the designs in the history data. If the design is already evaluated, the value of the objective function is returned and the time consuming calculation with a heavy model is avoided. Even with a large history data, the time spent in the comparison of designs is a fraction of the time used in heavy modeling. Fig. 9.2 shows the flow chart of the optimization process with a solution history.

To demonstrate the effect of using discretization and solution history, optimization run data for the rotor topologies are presented in Table 9.1. The actual results of the optimizations are presented in Section 9.3. The results in the table show that the optimization time is reduced by 29 – 47 %, depending on the individual run. Summing up all the evaluated and calculated designs respectively,

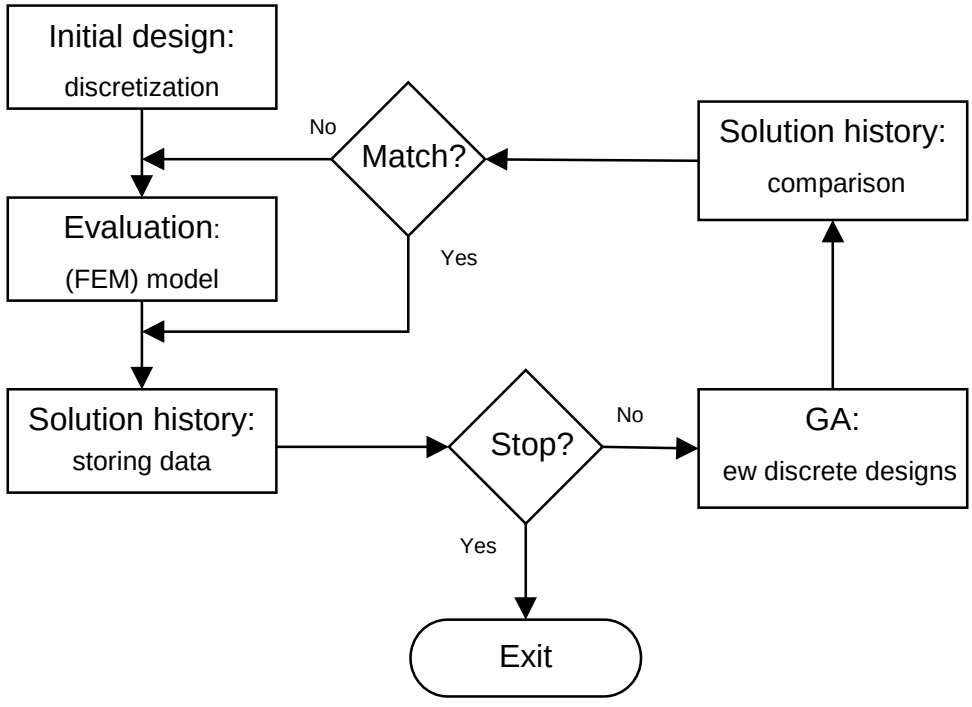

Fig. 9.2 Flow chart of optimization with discretization and solution history.

the average time saving is 39 %. The calculated designs cover the solution space more efficiently because the designs have noticeable differences between them. Thus, not only is time saved but the results contain more information for post-processing.

The time used in optimization relative to the amount of designs calculated is different from case to case. One reason for this is that different cases have different meshes and mesh sizes to start with. The size of the mesh also depends on the values of free variables in some cases. Another reason is that in some cases the solution space of the free variables was not subjected to non-linear constraints. These constrains would have neglected the possibility of impossible combinations for values of the variables. Only linear constraints could be used with the present GA software. An improper value combination is detected by the FEM mesh generator and a penalty function value is returned for that design. Thus the design is considered evaluated but no time is consumed since no actual FEM calculations are made.

Another use for the solution history is the opportunity to include more information on the calculated designs. In the case of an induction motor, different loss components, power factor, supply voltage and current, slip, torque and temperature rise data could be stored. Then, the solution history can be used for post-processing of the optimization results. Different objective functions can be valued simply by taking the data needed for the evaluation from the history data. Thus, the stored data can be used not only for a sensitivity analysis as a function of designs, but also as a function of the objective function, or indeed both. In addition, statistical analysis can be used to find relationships between designs and their characteristics in much the same way as with measured product data (Kytömäki *et al*. 1997). The solution history can be used as a database for ‘surface fitting’ where the behavior of the solved points is approximated by functions that are faster to solve. An example

Table 9.1 Effect of discretization and use of solution space to decrease the computation. The rotor topologies are illustrated in Figs. 9.7 – 9.13.

Optimization case	Free variables	Generations	Designs evaluated	Designs calculated	Optimization time [h]	Time saved [%]
Coated	2	8	323	181	46	44
Cage A	6	14	593	412	101	31
Cage B	8	44	1970	1049	153	47
Cage C	7	33	1488	928	203	38
Double coated	3	11	474	334	119	30
Coating, laminated	2	8	315	173	34	45
Grooved	4	13	550	389	175	29

of this is the use of linear and cubic spline functions as a replacement for a FEM model as illustrated in Bianchi and Bolognani (1999). One potential use for the solution data would be the teaching of a neural network system.

This combined use of discretization and solution history is applicable to any algorithm but it is most efficient when used with stochastic optimization algorithms like GA, fuzzy logic (Bianchi and Bolognani, 1996) or simulated annealing. There, the reduction of calculation time is likely to be most significant. The use of solution history in surface fitting is also utilized best with stochastic algorithms, since the fitting requires large amounts of data in order to give a good estimation of the real behavior of the objective function.

9.2 Optimization of a squirrel cage rotor of the 60 kW 60000 $^{1}/_{\mathrm{min}}$ motor

A numerical optimization of the rotor design was performed for a squirrel cage solid steel rotor. The 16 bar and the 26 bar rotors compared in Chapter 5 were already designed and manufactured but the existence of better designs was checked. For the squirrel cage rotors seen in Fig. 9.3, the main variables are the number of cage bars and the width and height of a bar. The air gap was also taken as a free variable. The dimensions of stator and stator winding were kept constant. The objective was to minimize the temperature rise in the stator winding as this was considered the limiting factor for the utilization of the motor. The objective function for the temperature rise ΔT was of the following form:

$$\Delta T = a_{\mathrm{s}} \left(w_{\mathrm{cus}} p_{\mathrm{cus}} + w_{\mathrm{fes}} p_{\mathrm{fes}} + w_{\mathrm{rot}} p_{\mathrm{rot}} - 1 \right) + S \,, \tag{9.1}$$

where a_{s} is a scaling factor and p_{cus}, p_{fes} and p_{rot} are the normalized power loss for the stator winding, stator iron and rotor, respectively. w_{cus}, w_{fes} and w_{rot} are the corresponding weights. The normalization is done so that the losses of the initial 16 bar design yield zero as a value for the function. S is the penalty function term. The scaling factor and weights for the loss components were derived from the results of a sensitivity analysis for a thermal network model made by Saari (1995). The power loss components were calculated with the finite element model discussed in Chapter 7.

The rotor design was optimized and the comparison was made at the nominal power of 60 kW at the rated speed of 60000 $^{1}/_{\mathrm{min}}$ although speeds only up to 50000 $^{1}/_{\mathrm{min}}$ could be tested, as discussed in Chapter 5. Designs were supplied with PAM. The model for the motor included stator end windings and rotor end rings.

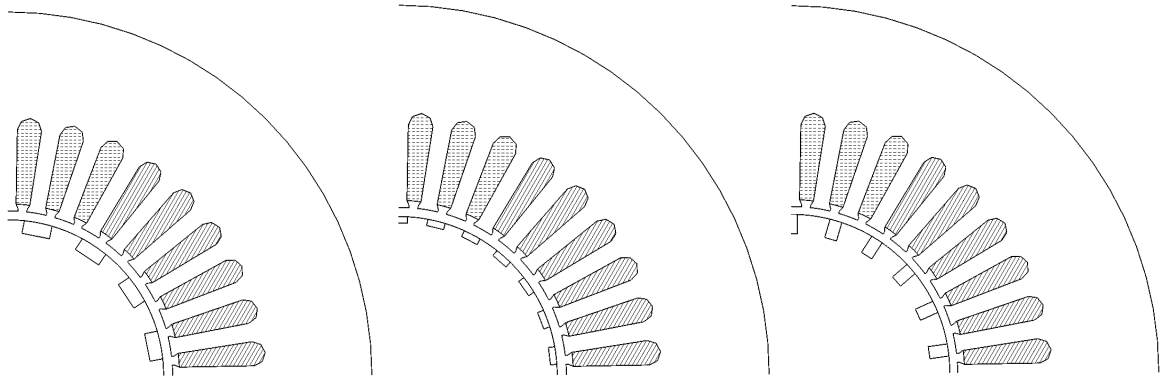

Fig. 9.3 Cross sections of the 16, 26 and 22 bar squirrel cage rotors. The 22 bar rotor on the right is the result of optimization, giving a lowest temperature rise of the stator winding.

The main constraint for the feasible design was the mechanical constraint limiting the height of the slot relative to the width of the solid iron tooth. This constraint was given by the manufacturer of the rotors. The constraint was not originally linear but for optimization purposes it was linearized, as can be seen from Fig. 9.4. There the constraint divides the search space into a feasible and a restricted domain. A penalty function was used to keep the designs in the feasible area. Because external penalty functions were used, the solutions of the optimization tend to be rather on the restricted side. This phenomenon indicates that the mechanical constraint due to the centrifugal forces and stress really prohibits otherwise optimal solutions.

9.2.1 Optimization results

Table 9.2 shows the result of the optimization compared with the actual rotors tested in Chapter 5. The value of the objective function is shown in the last row of the table. The values were scaled so that the initial 16 bar design received a zero value. A positive value meant a hotter stator winding and a negative value for a cooler winding. The geometries of the squirrel cage rotors are shown in Fig. 9.3 and the progress of the optimization run is illustrated in Fig. 9.4.

The result shows that a compromise has been made between the number of bars and the amount of copper. Large numbers of small bars induces less loss at the stator teeth because the permeance fluctuation is smaller. On the other hand, increasing the number of bars decreases the amount of copper because of the mechanical constraint. Fig. 9.5 shows that the bar height relative to the bar width is maximized as long as there is a balance between that ratio and the amount of copper.

The importance of an adequate amount of copper was seen in Chapter 5. There the 26 bar rotor performed poorly because of the mistake in the manufacture. As is seen from Table 9.2, the amount

Table 9.2 Design variables and calculated data for the 60000 $^{1}/_{min}$ 60 kW high-speed motor.

Design variables and calculation results	16 bar rotor, initial design	26 bar rotor	Optimized rotor	Copper coated rotor
Number of bars	16	26	22	-
Height of bar or coating [mm]	4	2.5	5.5	2
Width of bar [mm]	9	5	3.5	-
Amount of copper [mm^2], designed/realized	565/459	322/225	424/-	553/511
Air gap, iron-to-iron [mm]	2	2	2.25	4.5
Calculated total electric loss at 60 kW shaft power [W]	3479	2992	2641	2516
Calculated share of loss in the stator [%]	66	53	57	58
Calculated resistive loss in the stator winding [W]	528	524	513	727
Calculated relative temperature rise of stator winding [K]	-	-4.9	-8.1	7.0

of copper was only 70 % of the specified amount. According to the calculations, the 26 bar rotor would have been better than the 16 bar rotor if manufactured according to the specifications.

Different loss components are shown in Table 9.2 and Fig. 9.6. It is interesting to see that while the total electric loss for the copper coated rotor was the smallest, the temperature rise of the stator winding is the highest. The reason for this is the resistive loss in the stator winding, which was highest for the coated rotor. This result gives the example that a best utilization factor and a best efficiency do not necessarily go hand in hand.

9.2.2 Discussion

The above optimization case results suggested a squirrel cage design which is slightly different than the manufactured and tested designs. The result is reasonable and there are no obvious faults in the optimized design. However, the reliability and the accuracy of the models affect the result.

As is shown in Section 5.3, the calculation of electric loss did not match the measured results too well if the circulatory currents were not modeled. Modeling circulatory currents causing extra loss in the stator winding would affect the result of optimization. A smaller air gap would be preferred in order to decrease the magnetization current.

Another difficulty is the formulation of the objective function. If the weights in Eq. 9.1 are incorrect, the result of the optimization will also be incorrect. For the circulatory currents, the power loss for the stator winding p_{cus} should be increased. The difficult question is by how much?

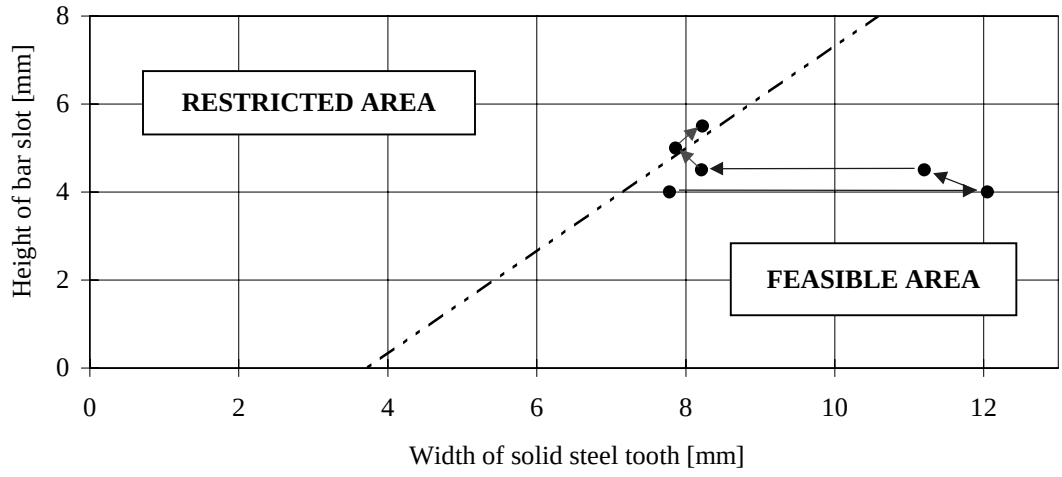

Fig 9.4 Movement of the optimal design as a function of slot shape during the optimization.

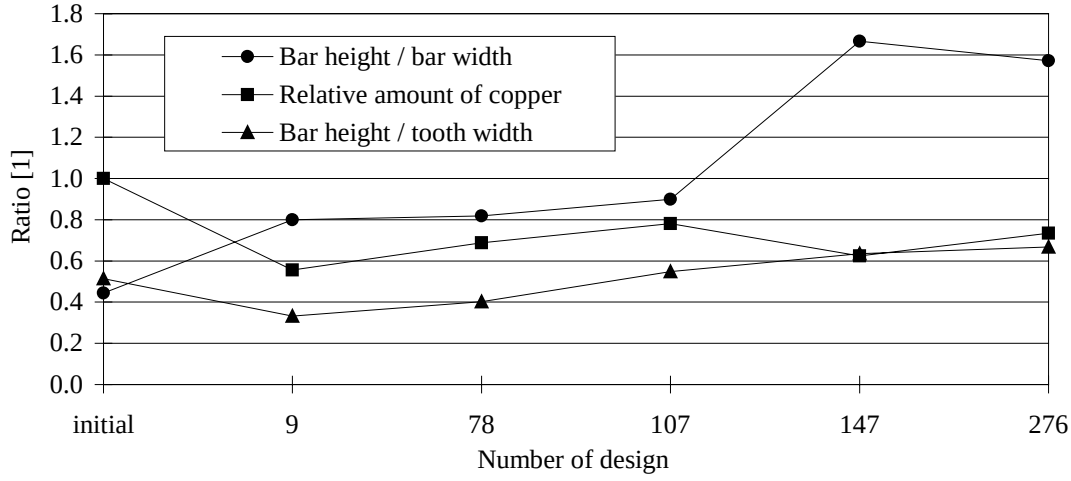

Fig. 9.5 A change of design during the optimization.

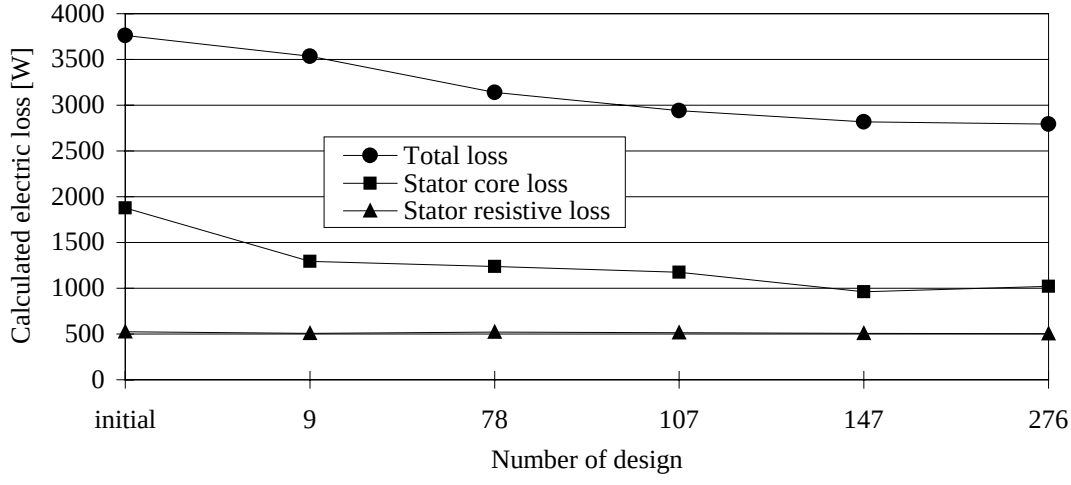

Fig. 9.6 A change of loss components during the optimization.

9.3 Optimization of general topology of a rotor

In this part of study the general topology of a rotor was looked at. This kind of work suits well for the numerical optimization since absolute values are not of key interest. The main idea is to get a general view of the possible solutions and their relative strengths and weaknesses. The copper coated design was also calculated with a laminated core to see if there were any difference in performance. In addition, a plain solid steel rotor with axial grooves was optimized to see the effect of missing good conductivity regions in the rotor design. The seven design cases were as follows.

- Coated design in Fig. 9.7, a solid steel rotor with a cylindrical copper coating on it. The two free variables are the outer diameter of the rotor and the thickness of the copper coating.
- Cage A design in Fig. 9.8, a solid steel rotor with a copper cage of circular bars. The six free variables are the outer diameter of the rotor, number of bars, diameter of bar, distance of bar from rotor surface and the width of the rotor slot opening. The last variable was the index for the slot filling material, representing air, copper or iron.
- Cage B design in Fig. 9.9, a solid steel rotor with a copper cage of quadrilateral bars. The eight free variables are the outer diameter of the rotor, number of bars, upper and lower width of bar, height of bar, height of the rotor tooth tip and the width of the rotor slot opening. The last variable was the index for the slot filling material, representing air, copper or iron.
- Cage C design in Fig. 9.10, a solid steel rotor with a copper cage of polygon bars together with a copper coating. The polygon bar consists of a quadrilateral in the bottom part of the slot and another quadrilateral extending from the top of it. The seven free variables are the outer diameter of the rotor, number of bars, heights and widths of the quadrilaterals, and the thickness of the copper coating.
- Double coated design in Fig. 9.11, a solid steel rotor with a cylindrical copper coating on it and a ferrite coating on top of the copper coating. The three free variables are the outer diameter of the rotor and the thickness of the copper and ferrite coating. The electromagnetic properties of Somaloy 500 powder material were used in the modeling.
- Coated, laminated design in Fig. 9.12, a laminated rotor with a cylindrical copper coating on it. The two free variables are the outer diameter of the rotor and the thickness of the coating. Electromagnetic properties of 0.2 mm high frequency steel sheet were used in the modeling.
- Grooved design in Fig. 9.13, a solid steel rotor with axial grooves at the surface and without any bars or layers. The four free variables are the outer diameter of the rotor, number of grooves and the height and width of the groove.

The different rotor topologies were modeled with their own parameterized element meshes. First order elements were used in the optimization, since modeling with second order elements would have been too time consuming. The calculation times are shown in Table 9.1 in Section 9.1. The resulting designs were calculated afterwards with second order elements to see the possible differences in the results.

This study concentrated only on the rotor design. Thus, the stator core and stator winding were kept constant. No mechanical or manufacturing constraints were enforced. Friction loss was not taken into account. Rotors not having a smooth surface generate more friction loss but they could be coated with a cylindrical sleeve. No thermal modeling was used in this study.

The objective function was simply the total electromagnetic loss of the motor. The motors were modeled at the same operational point yielding the same shaft power. Shaft power of 50.1 kW at 50100 $^{1}/_{\text{min}}$ was selected, as this was the nominal operation point for the tests performed and reported in Chapters 5 and 6. Nominal magnetization was used in the calculations.

The supply of the motors was modeled as a voltage supply giving one ideal voltage pulse per half a cycle. This corresponds to the output of a PAM voltage source inverter. Constant amplitude for the pulse was assumed, i.e., a constant DC-link voltage in an inverter and no voltage drops in power electronic circuits. The rise time of the pulse was considered zero but from the modeling point of view it was determined by the time discretization of the time-stepping method in FEM.

The rotors were modeled without endrings in order to keep the parameterization of the rotors simple. However, the stator was modeled together with the circuit equations for the end winding impedance. This means that the relative importance of stator winding loss was increased with respect to the rotor loss. The results will show that compared to a pure 2D calculation, the stator winding loss is overestimated by a factor of 2.6 – 3.1 as seen in Table 9.3. This more than compensates the effect of circulatory currents in a stator winding discussed in Chapter 8. If the end rings were modeled, the corresponding factor would be smaller for the rotor loss because of the smaller diameter relative to the 2D length of the motor.

9.3.1 Optimization results

The quarter cross sections of the initial and optimized motors are presented in Figs. 9.7. – 9.13. An example of post-processed results of the FEM model for the coated motor are shown in Appendix A. The results of the numerical optimization are presented in Table 9.3. The objective function value, i.e., the total electromagnetic loss, is given together with stator current, power factor, air gap flux and rotor slip. The different loss components are also given. The results of the optimized

designs calculated with second order finite elements are shown in the same Table. The real copper coated design measured and studied in Chapters 5 and 6 is calculated for the reference. In the following, the results are commented on case by case.

- Coated: The optimized design had a 26 % longer iron-to-iron air gap than the real copper coated design. Magnetization loss was increased but rotor loss was decreased more. The amount of copper remained the same. This case shows well how a trade-off has to be made between the loss in the stator winding and the harmonic loss induced in the copper coating.

  By changing the air gap, the loss balance between the stator and rotor can be changed. Considering this and the cooling system used at the same time, the utilization factor of the motor can be improved. However, this does not necessarily guarantee the best efficiency. The relation between utilization and efficiency was also discussed in Section 9.2.1. It is worth mentioning that this optimization result could be applied, as the mechanical properties are not different from the real copper coated rotor.

- Cage A: This design was qualified as a second best after Cage B. The iron-to-iron air gap was the smallest, being only 67 % of the air gap in the real copper coated design. This indicates that the copper bars were well protected from the air gap harmonics. The resulting design had open slots. The magnetization current and stator winding loss are the lowest.

  The optimal design would probably be difficult to implement, as the width of the rotor teeth is small. In this case particularly, a sensitivity analysis could give a good trade-off between the electromagnetic and mechanical characteristics.

- Cage B: This design proved to be the best according to the objective function and the model used. The design had the largest amount of copper in the rotor, over twice as much as in the Cage A design. The initial design had the bars reaching the surface of the slot but in the optimal design there are small rotor iron tooth tips and open slots. The optimal design would also probably be difficult to implement here, as the width of the rotor teeth is small.

  The main reason for the successful cages A and B is probably the more or less conventional placement of the copper bars. The only difference is perhaps the ratio of the amounts of core iron and copper. High-speed induction motor designs studied in this project are more electrically than magnetically loaded. That is, the average current linkage along the air gap is high relative to the air gap flux density (Chalmers and Williamson 1991).

- Cage C: This case tried to take the best elements of the copper cage and combine them with a coating. The result implies that the copper coating should not be used if discrete caging is

possible. The coating practically vanished and was replaced by bars very similar to the bars optimized in Section 9.2. This topology seems not to be useful as the result can be considered as a constrained optimization sub case for the Cage B design.

The amount of copper and rotor loss was about the same as for Cage B but the stator winding loss was higher. The iron-to-iron air gap was 20 % larger, probably in order to level the harmonic loss in the rotor coating and bar tops.

- Double coated: The idea was to shield the copper coating from the harmonic flux components in the air gap. The topmost iron powder coating has relatively good permeability. It produces a relatively low amount of iron loss due to high resistivity. The main flux travels through both coatings while most of the flux harmonics are confined within the topmost iron coating.

  The optimized design had a 9 % shorter iron-to-iron air gap than the real copper coated design and a 27 % shorter one than the optimized copper coated design. Compared to the real design, stator loss was the same but rotor loss was down 29 % according to the calculations with second order elements.

- Coated, laminated: The optimization result was practically the same as in the case for a solid rotor. The air gap was the same and the copper coating was 5 % higher. There was a slight improvement in magnetization properties as the magnetization reactance of the rotor iron increased.

  The results imply that the use of a solid rotor instead of a laminated rotor is not necessarily a significant problem. If this type of low slip and long air gap induction motor is constructed, the relative importance of skin effect in solid steel is not significant. It is good to keep this in mind when considering the mechanical properties of the rotor, whether they are circumferential forces or critical speeds, or a sub/overcritical operation.

- Grooved: The grooved solid steel rotor without any cage or coating suffered from high resistivity for the torque-producing currents. The slip and the rotor loss were high. Constraints for the maximum number and height of grooves became active for the optimal design. Removing these constraints would have improved the outcome somewhat. The radial grooving in addition to the axial grooving would also improve the design. However, the basic difference in the result with respect to the other designs would remain.

The biggest difference in the calculation results for 1^{st} or 2^{nd} order elements seem to be in the cases where the design is more influenced by the skin effect and harmonics. The percentual difference is the biggest for the real copper coated rotor design. The second order elements model the skin effect

regions better and this leads to lower power loss values in these cases. It is interesting to see that for the double coated design the result is practically the same for both orders of elements.

Use of discretization and solution history in optimization makes sensitivity analysis rather straightforward. Sensitivity to the change in a design or in the objective function can be made quickly without using the actual model for the high-speed motor. It is emphasized that while some of the rotors optimized may look difficult to implement, the sensitivity analysis may show that a good trade-off exists between the optimality of a rotor and the feasibility. For example, the optimized cage A rotor looks as if it is not able to withstand high circumferential stress. However, a smaller number of slightly thicker bars keeps the amount of total loss practically the same while the feasibility of the mechanical construction is significantly improved.

Results of comparisons can be informative even if the model used to calculate the designs or the objective function are not exactly correct. Errors that are of the offset or scaling type do not necessarily affect the comparison results. An example of this could be the miscalculation of stator core loss. In the optimization cases, the stator construction was constant and the flux densities in the iron were almost the same in every case.

On the other hand, the existence of some errors may have a major impact on the results of a comparison. An example of this could be the underestimation of ohmic loss in the stator winding due to the circulatory currents. Thus, designs needing a higher magnetization current are not penalized enough and are considered better designs than they really are. The fact that the stator design was kept constant in this study should also be kept in mind. For example, changing the stator teeth dimensions affects the harmonic content of the air gap flux. Designs that are especially sensitive to the air gap harmonics could perform better with respect to other designs if the stator construction was optimized at the same time.

9.3.2 Conclusion

In Chapter 5 and in the optimization case for the squirrel cage solid steel rotor, the amount of copper available for a design was discussed as being an important issue. The results of this optimization study show that in general the question is about the positioning of the conductors for the currents producing the torque. Copper should be shielded from the harmonics of the air gap flux to gain the full benefit of the conductive material.

Laminating the rotor may not improve the electromagnetic design of the rotor significantly. Thus, solid steel rotors may well be used if the positioning and sizing of the conductors are not changed.

Table 9.3. Optimization results for the general topology of a rotor for the high-speed induction motor.

Motor design	Real design		Coated		Cage A		Cage B		Cage C		Double coated		Coated, laminated		Grooved	
Order of elements	1st order	2nd order	1st order	2nd order	1st order	2nd order	1st order	2nd order	1st order	2nd order	1st order	2nd order	1st order	2nd order	1st order	2nd order
Objective function [W]	2074	1850	1923	1818	1577	1538	1490	1429	1621	1549	1665	1662	1892	1789	3176	2991
Stator current [A]	149	148	165	163	134	132	145	140	162	153	148	147	160	158	137	135
Power factor [1]	0.58	0.58	0.52	0.52	0.64	0.65	0.59	0.60	0.53	0.56	0.58	0.58	0.54	0.54	0.64	0.65
Air gap flux [T]	0.36	0.36	0.36	0.35	0.37	0.37	0.37	0.37	0.36	0.36	0.36	0.36	0.36	0.36	0.37	0.37
Rotor slip [%]	0.52	0.52	0.55	0.56	0.32	0.29	0.14	0.14	0.16	0.16	0.53	0.53	0.59	0.60	1.53	1.56
Stator resistive loss [W]	597	628	728	758	479	502	560	568	703	666	580	607	681	710	500	523
– loss in end winding [W]	400	391	490	479	320	311	375	354	473	418	391	386	458	447	335	329
Stator core loss [W]	641	625	625	610	670	650	654	636	639	622	648	632	630	615	654	637
Rotor resistive loss [W]	836	596	569	449	416	372	275	223	279	260	369	362	581	463	1848	1677
Rotor core loss [W]	0	0	0	0	11	14	2	3	0	0	67	61	0	0	175	154

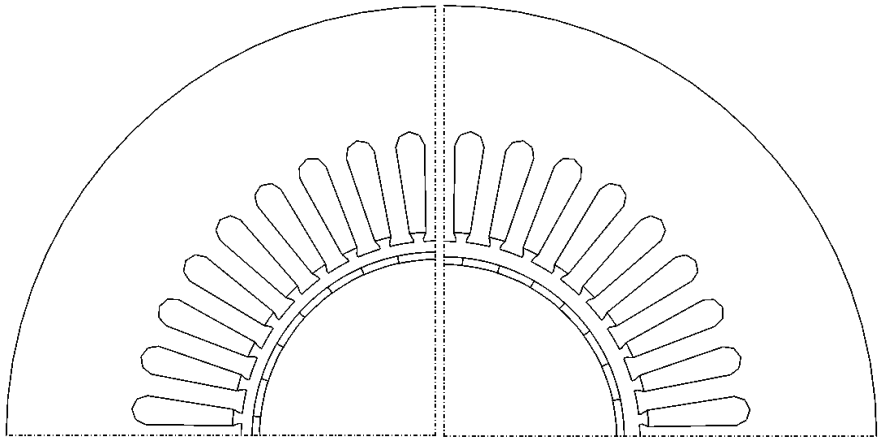

Fig. 9.7 Initial (left) and optimized (right) designs of the coated rotor.

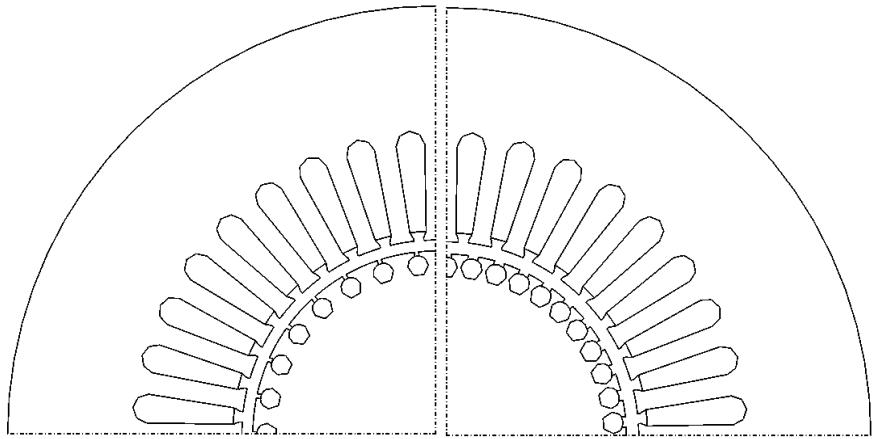

Fig. 9.8 Initial (left) and optimized (right) designs of the cage A rotor.

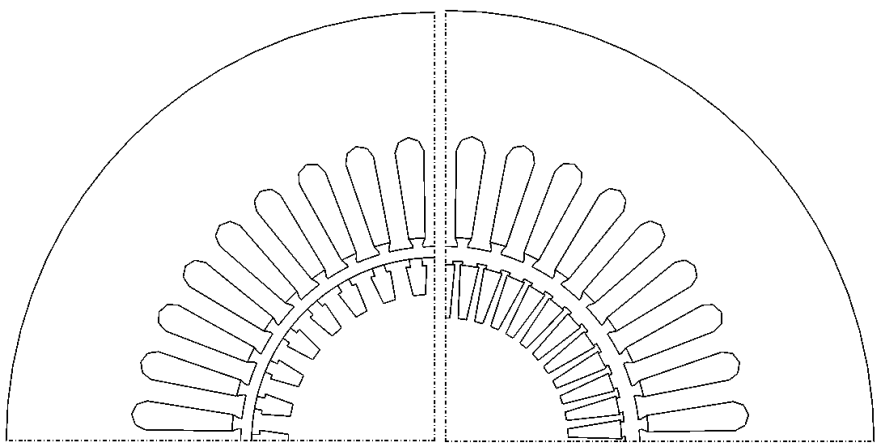

Fig. 9.9 Initial (left) and optimized (right) designs of the cage B rotor.

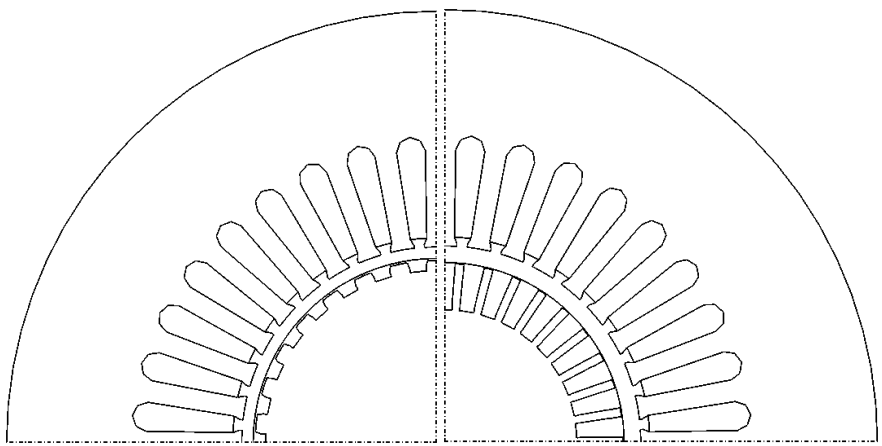

Fig. 9.10 Initial (left) and optimized (right) designs of the cage C rotor.

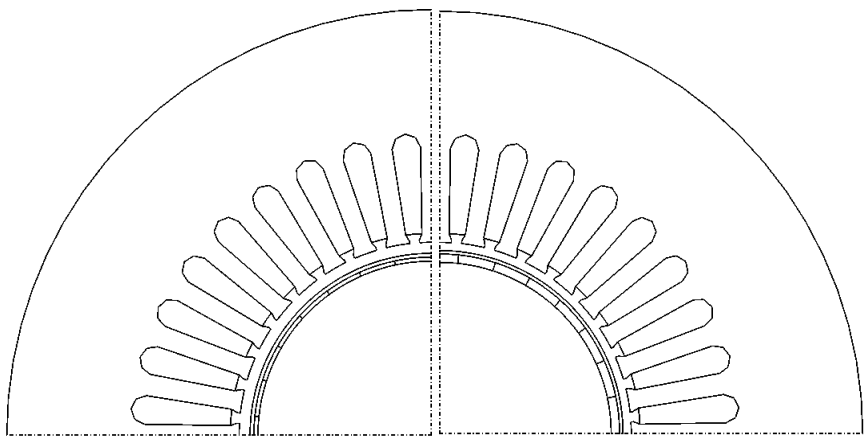

Fig. 9.11 Initial (left) and opt. (right) designs of the double coated rotor.

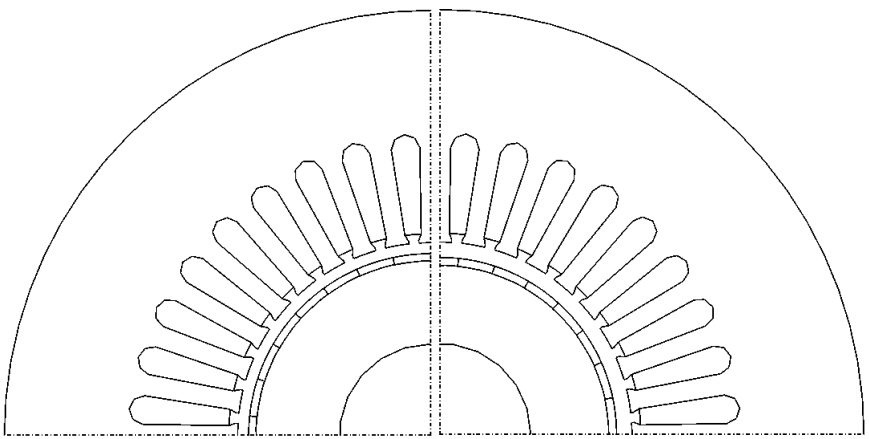

Fig. 9.12 Initial (left) and opt. (right) designs of the coated laminated rotor.

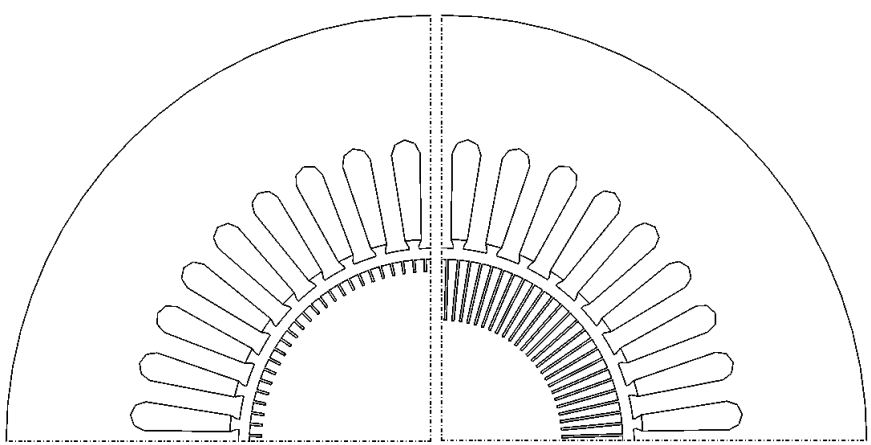

Fig. 9.13 Initial (left) and optimized (right) designs of the grooved rotor.

10 SUMMARY

The motivation and aim of this work was to find good designs for high-speed induction machines. Special attention was paid to rotors suitable for these machines. Another goal was to find supply voltage waveforms appropriate for a high-speed induction machine with a solid rotor. In order to design good high-speed machines, modeling was modified and verified.

A study of literature showed that a high-speed induction motor design is different from a conventional design. The lamination and winding materials must be suited to a high frequency voltage, current and flux. The waveform of the magnetic air gap flux should be made as sinusoidal as possible in order to avoid excessive power loss at the rotor side. This is especially important with solid steel rotors. Different ways to obtain the flux with a low harmonic content are suggested in the literature review.

Mechanical and thermal constraints affect the feasible design of a high-speed rotor. These constraints indicate that a higher power relative to speed can be achieved with a solid steel rotor rather than with a laminated rotor. Solid rotors can stand a higher centrifugal stress and the bending critical speeds are higher than those of a laminated rotor. On the other hand, the electromagnetic properties of a laminated rotor are better. This contradiction was studied by testing a laminated rotor modified for a high-speed motor and a solid steel rotor with a squirrel cage.

The laminated rotor was tested for a 65 kW 30600 $^{1}/_{\mathrm{min}}$ compressor drive. Two squirrel cage solid steel rotors were tested for a 60 kW 60000 $^{1}/_{\mathrm{min}}$ high-speed motor. In both the cases, the rotors were compared against a commercially used copper coated solid steel rotor. In the case of the 65 kW drive, the actual compressor was used for loading the motor. For the 60 kW motor, two similar motors were coupled together, one working as a motor and the other as a generator. This back-to-back setup provided more information and made a division of power loss into loss components possible. In this setup, the temperature of the rotor surface could also be measured using an infrared camera.

Pulse amplitude modulation and pulse width modulation are commonly used techniques in adjusting the supply voltage of electric machines. Pulse width modulation needs a high switching frequency relative to the supply frequency in order to produce feasible voltage waveforms. The results of the measurements showed that the idea of moving the harmonic content of voltage and current upwards in spectral scale by increasing the switching frequency does not apply well for the

high-speed induction machine. According to the results, the currents of a higher harmonic order produce more loss than the same amount of lower order harmonics. This result, together with the consideration of inverter and drive loss, implies that pulse amplitude modulation should be preferred as a voltage waveform for high-speed induction machines.

The modeling of the high-speed induction motor was studied. For the motors considered, the 3D effects made the 2D modeling of the electromagnetic properties difficult. Two modifications to the current modeling software were made. In the first modification, the end ring inductance was calculated with a separate 2D FEM model. In the other modification, the flux fringing in the air gap region was also modeled with a separate 2D FEM model. The modified software was used to calculate the characteristics of the high-speed induction motors.

The comparison of the measurements and calculations showed that the calculated electromagnetic loss was not accurate. Circulatory currents in the stator winding were suspected of causing some of the discrepancy in the results. Additional measurements showed circulatory currents flowing in the parallel paths of a stator winding of the high-speed motor. Circulatory current loss coefficients were measured at different frequencies. An estimation model was used to estimate the value of the loss coefficient at the frequencies which could not be measured. Taking the circulatory currents into account, the model used in calculations provides results close to the measured ones. Thus, the model can be used for the designing and optimization of high-speed machines.

In this work, the numerical optimization has been used to highlight and value new designs for rotors in a high-speed induction machine. The use of design variable discretization together with solution history were proposed as a new improvement for the optimization algorithms used with numerical modeling. This improvement can significantly decrease the computation time and makes more informative post processing of the results possible.

Genetic optimization software was used to derive the optimal parameters for a squirrel cage solid steel rotor. The results indicated that the actual squirrel cage rotors manufactured and tested could be improved using a different kind of cage. A general topology suitable for a high-speed induction machine was also studied by using optimization.

The measurements for the 30600 $^{1}/_{\mathrm{min}}$ compressor drive and 60000 $^{1}/_{\mathrm{min}}$ high-speed motor and the results of the optimization cases show that both the positioning and the volume of conductors in the rotor are important. The choice between a laminated and a solid rotor core material seems less significant for a high-speed induction machine if it does not affect the positioning of the conductors. This is so if only the electromagnetic properties of rotors are considered.

REFERENCES

Arkkio A. 1987. **Analysis of Induction Motor Based on the Numerical Solution of the Magnetic Field and Circuit Equations**. Acta Polytechnica Scandinavica, Electrical Engineering Series No. 59. Helsinki, Finland. 97 p.

Bertotti G., Boglietti A., Chiampi M., Chiarabaglio D., Fiorillo F. and Lazzari M. 1991. **An Improved Estimation of Iron Losses in Rotating Electrical Machines**. IEEE Transaction on Magnetics. Vol. 27, No. 6, November. pp. 5007 – 5009

Bianchi N., Bolognani S. and Zigliotto M. 1996. **Fuzzy Knowledge Based Design of PM Synchronous Motors**. International Conference on Electrical Machines ICEM '96. Conference Proceedings. Vigo, Spain. Vol. 2. pp. 365 – 369

Bianchi N. and Bolognani. S. 1998. **Design Optimisation of Electric Motors by Genetic Algorithms**. IEE Proceedings of Electric Power Applications. Vol. 145. No. 5. September. pp. 475 – 483

Bianchi N. and Bolognani S. 1999. **Design Optimisation of Electrical Motors by an Adaptive Model Based Optimisation Technique**. Ninth International Conference on Electrical Machines and Drives. Conference Publication No. 468, IEE. pp. 291 – 296

Boglietti A., Ferraris P., Lazzari M. and Profumo F. 1988. **Preliminary Considerations About the Adoption of Unconventional Magnetic Materials and Structures For Induction Motors**. IEEE IAS meeting. Vol. 1. pp. 188 – 194

Boglietti A., Ferraris P., Lazzari M. and Profumo F. 1992. **About the Design of Very High Speed Induction Motors for Spindle Applications**. IEEE IAS-meeting. pp. 25 – 32

Boglietti A. 1999. **A First Approach for the Iron Losses Building Factor Determination**. IEEE IAS meeting. Vol. 1. pp. 489 – 493

Chalmers B. and Williamson A. 1991. **A.C. Machines: Electromagnetics and Design**. Research Studies Press LTD. Taunton, UK. 165 p.

Driesen J., Pahner U., Belmans R. and Hameyer K. 2000. **Transient Coupled Magnetic Thermal Analysis of a Permanent Magnet Synchronous Electrical Vehicle Motor**. International Conference on Electrical Machines ICEM 2000. Proceedings. August 28 – 30. Espoo, Finland, Vol 1. pp. 343 – 347

Flack T. J. and Knight R. E. 2000. **Prediction of the Performance of Large Induction Motors Including the Effect of Radial Ventilation Ducts Using 2-D and 3-D finite-element Formulations**. International Conference on Electrical Machines ICEM 2000. Proceedings. August 28 – 30. Espoo, Finland, Vol 1. pp. 372 – 376

Foelsch K. 1936. **Magnetfeld und Induktivität einer zylindrischen Spule**. Archiv für Elektrotechnik. Vol. 30. No. 3. pp. 139 – 157. (In German)

Fuchs E. F. and Frank U. V. 1983a. **High-Speed Motors with Reduced Windage and Eddy Current Losses, Part I: Mechanical Design**. ETZ Archiv. Bd. 5, H. 1. pp. 17 – 23

Fuchs E. F. and Frank U. V. 1983b. **High-Speed Motors with Reduced Windage and Eddy Current Losses, Part II: Magnetic Design**. ETZ Archiv. Bd. 5, H. 2. pp. 55 – 62

Gilon D. C. 1994. **Cooling Solutions for High-Speed High-Power Induction Motors**. International Conference on Electrical Machines ICEM ’94. Conference Proceedings. Paris, France. Vol. 3. pp. 516 – 521

Holtz J. 1994. **Pulsewidth Modulation for Electronic Power Conversion**. Proceedings of IEEE. Vol. 82, No. 8, August. pp. 1194 – 1214.

Huppunen J. and Pyrhönen J. 2000. **Filtered PWM-inverter Drive for High-Speed Solid-Rotor Induction Motors**. Conference Record of the 2000 IEEE Industry Applications Conference, Vol. 3. pp. 1942 – 1949

IEC Standard 34-1. 1994. **Rotating Electrical Machines - Part 1: Rating and performance.** Ninth edition. International Electrotechnical Commission. Geneva, Switzerland. 129 p.

Ikeda M., Sakabe S. and Higashi K. 1990. **Experimental Study of High Speed Induction Motor Varying Rotor Core Construction**. IEEE Transactions on Energy Conversion. Vol. 5, No. 1, March. pp. 98 – 103

Ito M., Arai K., Takahashi N., Kiwaki H. and Seya T. 1988. **Magnetically Anisotropic Solid Rotor of an Induction Motor**. IEEE Transactions on Energy Conversion. Vol. 3, No. 2, June. pp. 427 – 432

Jokinen T. 1982. **Pyörivän sähkökoneen suunnitteleminen**. TKK Offset. Espoo. Finland. 72 p. (In Finnish)

Jokinen T. and Arkkio A. 1996. **High-Speed AC Motors**. Symposium on Power Electronics, Industrial Drives, Power Quality, Traction System, (Speedam ’96). Proceedings. Capri, Italy. June 5^{th} – 7^{th}. pp. B5-9 – B5-14

Jokinen T. and Saari J. 1997. **Modelling of the Coolant Flow with Heat Flow Controlled Temperature Sources in Thermal Networks**. IEE proceedings on Electric Power Applications. Vol. 144, No. 5, September. pp. 338 – 342

Kaga A., Anazawa Y., Akagami H., Watabe S. and Motohiko M. 1982. **A Research of Efficiency Improvement by Means of Soft Ferrite in Small Induction Motors**. IEEE Transactions on Magnetics. vol. Mag-18, No 6, November. pp. 1547 – 1549

Kytömäki R., Arkkio A., Niemenmaa A. and Suontausta A. 1997. **Validity of Conventional and Modern Methods of No-Load Loss Calculation in Asynchronous Machines – Statistic approach**. IEE Conference on Electrical Machines and Drives EMD ’97. Proceedings, August 12 – 16, Cambridge, UK. pp. 185 – 189

Lähteenmäki J. 1997. **Optimisation of High-Speed Motors Using a Genetic Algorithm**. IEE Conference on Electrical Machines and Drives EMD ’97. Proceedings, August 12 – 16, Cambridge, UK. pp. 26 – 30

Lähteenmäki J., Arkkio A., Soitu V. and Saari J. 1999. **Comparison of a Partly Laminated Squirrel Cage Rotor and a Copper-Coated Solid Steel Rotor for a 50 kW High-Speed Compressor**. The Third Chinese International Conference on Electrical Machines. Proceedings., August 29 – 31, Xi'an, P. R. China. Vol 1. pp. 25 – 28

Lähteenmäki J. K. and Soitu V. 2000. **Comparison of Solid Steel Rotors with a Copper Coating or with a Copper Cage for a 60 kW 60.000 RPM Compressor**. International Conference on Electrical Machines ICEM 2000. Proceedings. August 28 – 30. Espoo, Finland, Vol 2. pp. 623 – 626

Lampola P. 2000. **Directly Driven, Low-Speed Permanent-Magnet Generators for Wind Power Applications**. Acta Polytechnica Scandinavica, Electrical Engineering Series No. 101. Espoo, Finland. 62 p (+106p.).

Lantto E. 1997. **Finite Element Model for Elastic Rotating Shaft**. Acta Polytechnica Scandinavica, Electrical Engineering Series No. 88. Espoo, Finland. 73 p.

Lantto E. 1999. **Robust Control of Magnetic Bearings in Subcritical Machines**. Acta Polytechnica Scandinavica, Electrical Engineering Series No. 94. Espoo, Finland. 143 p.

Lantto E. 2002. **Active Magnetic Bearings**. Design of High-Speed Electrical Machines, Postgraduate Seminar on Electromechanics. Helsinki University of Technology, Laboratory of Electromechanics. 20 – 26.5.2002, Espoo, Finland.

Lindell I. 1994. **Sähkötekniikan Historia**. Otatieto Oy. Publication No: 552. Tampere, Finland. 516 p. (In Finnish)

Meeker D. 1999. **Finite Element Method Magnetics, User's Manual**. Http://members.aol.com/dcm3c. August 25. 51 p.

Mekhiche M., Kirtley J.L., Tolikas M., Ognibene E., Kiley J., Holmansky E. and Nimblett F. 1999. **High Speed Motor Drive Development for Industrial Applications**. International Conference on Electric Machines and Drives, IEMD '99. pp. 244 – 248

Mohan N., Undeland T. and Robbins W. 1995 **Power Electronics: Converters, Applications, and Design**. John Wiley & Sons Inc. USA. 802 p.

Palko S. 1996. **Structural Optimization of an Induction Motor using a Genetic Algorithm and a Finite Element Method**. Acta Polytechnica Scandinavica, Electrical Engineering Series No. 84. Helsinki, Finland. 99 p.

Patent FI 100749. **Epätahtikoneen roottorissa käytettävä levyroottorirakenne**. High Speed Tech Oy Ltd, Tampere, Finland. 13.2.1998, 16 p. (In Finnish)

Patent US 5473211. **Asynchronous Electric Machine and Rotor and Stator for Use in Association therewith**. High Speed Tech Oy Ltd, Tampere, Finland. Appl. No 86880, 7.7.1992, 9 p.

Pyrhönen J. and Kurronen P. 1993. **Massiiviroottorisen Suurnopeusoikosulkumoottorin Hyötysuhteen Parantaminen, Osa 3, Loppuraportti**. Tutkimusraportti EN B-80 LTKK. Energiatekniikan osasto, Lappeenrannan Teknillinen Korkeakoulu. 16 p. (In Finnish)

Pyrhönen J. and Kurronen P. 1994. **Increasing the Efficiency of High-Speed Solid-Rotor Induction Machines**. International Conference on Electrical Machines ICEM ‘94. Conference Proceedings. Paris, France. Vol. 1. pp. 47 – 52

Pyrhönen J. and Huppunen J. 1996. **A New Medium Speed Solid Induction Motor for A High-Speed Milling Machine**. Symposium on Power Electronics, Industrial Drives, Power Quality, Traction System, (Speedam ‘96). Proceedings. Capri, Italy. June 5 – 7. pp. B5-1 – B5-7

Rajagopalan P. K. and Balarama Murty V. 1969. **Effects of Axial Slits on the Performance of Induction Machines with Solid Iron Rotors**. IEEE Transactions on Power Apparatus and Systems. Vol. PAS-88, No. 11, November. pp. 1695 – 1709

Reichert K. and Pasquarella G. 1995. **High Speed Electric Machines, Status, Trends and Problems**. Stockholm Power Tech Conference. Proceedings. June 18 – 22. Stockholm, Sweden. pp. 41 – 49

Richter R. 1951. **Elektrische Maschinen I, Allgemeine Berechnungselemente Die Gleichstrommaschinen**. Zweite verbesserte Auflage. Verlag Birkhäuser. Basel, Switzerland. 630 p. (In German)

Saari J. and Arkkio A. 1994. **Losses in High-Speed Asynchronous Motors**. International Conference on Electrical Machines ICEM ‘94. Conference Proceedings. Paris, France. Vol. 3. pp. 704 – 708

Saari J. 1995. **Thermal Modelling of High-Speed Machines**. Acta Polytechnica Scandinavica, Electrical Engineering Series No. 82. Helsinki, Finland. 82 p.

Saari J. and Arkkio A. 1995. **Cooling of a 100.000 RPM High-Speed Electrical Motors**. The Second Chinese International Conference on Electrical Machines CICEM ’95. Conference Proceedings. Hangzhou, China. pp. 317 – 322

Saari J. 1998. **Thermal Analysis of High-Speed Induction Machines**. Acta Polytechnica Scandinavica, Electrical Engineering Series No. 90. Helsinki, Finland. 73 p.

Schmied J. 1990. **Experience with Magnetic Bearings Supporting a Pipeline Compressor**. 2nd International Symposium on Magnetic Bearings. Proceedings. Tokyo, Japan. pp. 47 – 55

Shanel M., Pickering S. J. and Lampard D. 2000. **Application of Computational Fluid Dynamics to the Cooling of Salient Pole Electrical Machines**. International Conference on Electrical Machines ICEM 2000. Proceedings. August 28 – 30. Espoo, Finland, Vol 1. pp. 338 – 342

Sharma N. D., Anbarasu R., Nataraj J., Dangore A. Y. and Bhattacharjee B. 1996. **Experimental Investigations on High Speed Solid and Composite Rotor Induction Motor**. International Conference on Power Electronics, Drives and Energy Systems for Industrial Growth. Proceedings. Vol. 2. New York, New York, USA. pp. 913 – 919

Siegwart R., Larsonneur R. and Traxler A. 1990. **Design and Performance of High Speed Milling Spindle in Digitally Controlled AMB’s**. 2nd International Symposium on Magnetic Bearings. Proceedings. Tokyo, Japan. pp. 197 – 204

Smith A. C., and Edey K. 1995. **Influence of Manufacturing Processes on Iron Losses**. Seventh International Conference on Electrical Machines and Drives EMD ‘95. Conference Publication No. 412, IEE. pp. 77 – 81

Soong W. L., Kliman G. B., Johnson R. N., White R. A. and Miller J. E. 2000. **Novel High-Speed Induction Motor for a Commercial Centrifugal Compressor**. IEEE Transactions on Industry Applications. Vol. 36, No. 3, May/June. pp. 706 – 713

Surahammars Bruk. 1998. **Non-oriented Fully Processed Electrical Steels.** Product catalogue, Surahammars Bruks AB, Sweden

Szücs Á. 2001. **Macro Element Method for Modeling Eddy Currents in the Multi-Conductor Windings of Electrical Machines**. Acta Polytechnica Scandinavica, Electrical Engineering Series No. 106. Espoo, Finland. 88 p.

Takahashi I., Koganezawa T., Su G. and Ohyama K. 1994. **A Super High Speed PM Motor Drive System by a Quasi-Current Source Inverter**. IEEE Transactions on Industry Applications. Vol. 30. No. 3. May/June. pp. 683 – 690

Viggiano F. and Schweitzer G. 1992. **Active Magnetic Support and Design of High Speed Rotors for Powerful Electric Drives**. Third International Symposium on Magnetic Bearings. Proceedings. July 29 – 31. Alexandria, Virginia, USA. pp. 549 – 558

Wood B. M., Olsen C. L., Hartzo G. D., Rama J. C. and Szenasi F. R. 1997. **Development of an 11000-r/min 3500-HP Induction Motor and Adjustable-Speed Drive for Refinery Service**. IEEE Transactions on Industry Applications. Vol. 33, Issue 3, May-June. pp. 815 – 825

Zach F. 1989. **Comparison of Voltage and Current Spectra Using Optimized Forms of Inverter Pulsewidth Modulation**. IEE Transactions on Power Electronics. Vol. 4, No. 1. pp. 64 – 72

APPENDIX

A. CALCULATION OF ELECTROMECHANIC CHARACTERISTICS

The calculation of electromagnetic characteristics, including the electromagnetic torque, is based on the finite element method, FEM. Only the basic idea and the equations for losses are presented here.

The electromagnetic model is based on Maxwell's equations. Even in high-speed machines, the frequencies of the electromagnetic quantities are low enough to use the quasi-static formulation. There, the displacement current term $^{\partial \mathbf{D}}/_{\partial t}$ is omitted from the equations. In the quasi-static case, the magnetic vector potential $\boldsymbol{A}$ is

$$\nabla \times (\nu_r \nabla \times \boldsymbol{A}) = \boldsymbol{J}\,, \tag{A1}$$

where ν_r is reluctivity of a material and $\boldsymbol{J}$ is a current density. The current density can be expressed using the magnetic vector potential and scalar potential ϕ of an electric field:

$$\boldsymbol{J} = -\gamma \frac{\partial \boldsymbol{A}}{\partial t} - \gamma \nabla \phi\,, \tag{A2}$$

where γ is electric conductivity. In a 2D case, $\boldsymbol{A}$ and $\boldsymbol{J}$ only have components normal to the 2D-plane, which is selected to be the cross-section of the motor. Eq. A2 can be substituted in A1, assuming that the electric potential difference u between the ends of the conductor is known. The substitution yields

$$\nabla \times (\nu_r \nabla \times \boldsymbol{A}) + \gamma \frac{\partial \boldsymbol{A}}{\partial t} = \frac{\gamma}{l} u \boldsymbol{e}_z\,, \tag{A3}$$

where l is the length of a conductor. Integrating the current density in Eq. A2 over the cross section of the conductor, a relation between the u and the current i of the conductor becomes:

$$u = Ri + R \int_{S_j} \gamma \frac{\partial \boldsymbol{A}}{\partial t} \cdot d\boldsymbol{S}\,, \tag{A4}$$

where R is a DC-resistance. The end winding impedance of the stator windings and the supply voltage are taken into account using Kirchoff laws for electric circuits together with Eq. A4.

The end ring of the squirrel cage is modeled with circuit equations. The resistance is calculated from the conductivity and the dimensions of the end ring. The end ring inductance is modeled with a separate 2D FEM model. For the solid iron, there is no end ring impedance modeled. Thus, the

currents in the solid iron flow more freely as they would in the real case. The total impedance of the rotor is underestimated and the torque produced by these currents is slightly overestimated as a function of a slip. In the case of a coated rotor, the coating is divided into bars and the end ring sections.

The third dimension, the length of the machine is defined by the effective motor length l_{eff}, which takes into account the axial flux fringing at the air gap region. The flux fringing and the determination of the effective length is modeled with a separate 2D FEM model. An electromagnetic torque is calculated using Maxwell's stress tensor, integrating the tensor over the air gap region S_{ag}.

$$T_{\mathrm{e}} = \frac{l_{\mathit{eff}}}{\mu_0 (r_{\mathrm{s}} - r_{\mathrm{r}})} \int_{S_{\mathrm{ag}}} r B_{\mathrm{r}} B_{\varphi} d\boldsymbol{S} \,, \tag{A5}$$

where μ_0 is the permeability of vacuum and r_{s} and r_{r} are outer and inner radii of air gap, respectively. B_{r} and B_{φ} are radial and tangential components of magnetic flux density, respectively.

The computation is done using either a time-harmonic formulation or a time discretization. The solution of the equations yields the magnetic vector potential, the currents for the stator windings and the voltages for the rotor bars.

In time-harmonic formulation, the rotation of the rotor is approximated by multiplying the conductivities of the rotor conductors with the value of the slip. The non-linearity of iron is taken into account by using effective reluctivity.

In the time stepping formulation, the time is discretized into time steps using the Crank-Nicholson method. At each time step, the rotor is rotated by an appropriate angle corresponding to its rotational speed. Non-linearity of the magnetic materials is taken into account and the system of the non-linear equations is solved with the Newton-Raphson iteration method. With the time-stepping method, any supply waveforms can be modeled. This is a basic requirement in order to model the inverter fed machines.

The time stepping method has been used in the study to obtain the results for the calculations. However, the harmonic analysis is needed to give an initial starting point for the time-stepping method. The initial point given by the harmonic analysis is improved by computing a DC field from the instantaneous values of the currents solved. Thus, the initial starting point includes the instantaneous currents from the time harmonic solution and the DC-field based on those currents.

Instantaneous power components are calculated using the following equations:

$$P_{\text{in}} = \sum_{i=1}^{m} u_i^{\text{s}} i_i^{\text{s}} \tag{A6}$$

$$P_{\text{res}}^{\text{s}} = \sum_{i=1}^{m} R_{\text{s}i} \left(i_i^{\text{s}} \right)^2 \tag{A7}$$

$$P_{\text{res}}^{\text{r}} = -\int_V \boldsymbol{J} \cdot \frac{\partial \boldsymbol{A}}{\partial t} dV \tag{A8}$$

P_{in} is input power of a machine. $P^{\text{s}}_{\text{res}}$ is resistive loss of a stator winding and $P^{\text{r}}_{\text{res}}$ is resistive loss in the rotor. $R_{\text{s}i}$ is the DC-resistance of one phase winding. Resistive loss in the rotor is calculated both in current carrying copper (bars or coating) and in the solid part of the rotor. The effective values for loss components are calculated from the instantaneous values, integrating over time of some periods of a supply frequency.

Eddy-current loss for the elements in a laminated iron P_{feE} and hysteresis loss for the elements in iron P_{feH} are calculated using the Fourier coefficients of the flux density $\boldsymbol{B}_{\text{n}}$, solved from the vector potential $\boldsymbol{A}$ during the time-stepping. C_{E} and C_{H} are loss coefficients fitted from the material data. These losses do not affect the solution of the magnetic field. In case of a solid steel rotor, Eq. A8 is used instead of Eq. A10.

$$P_{\text{feE}} = -\int_V \left(\sum_{n=1}^{N} C_{\text{E}} (n\omega)^2 \boldsymbol{B}_n^2 \right) dV \tag{A9}$$

$$P_{\text{feH}} = -\int_V \left(\sum_{n=1}^{N} C_{\text{H}} (n\omega) \boldsymbol{B}_n^2 \right) dV \tag{A10}$$

In order to estimate the eddy-current loss in the stator windings the following equation was used. It was approximated that the eddy-currents in the small diameter conductors did not affect the magnetic field:

$$P_{\text{E}}^{\text{sw}} = -\int_V \left(C_{\text{E}}^{\text{sw}} \gamma r^2 \boldsymbol{B}^2 \right) dV \,, \tag{A11}$$

where the $C^{sw}{}_E$ is the loss coefficient taking into account the slot filling factor and the shape of the conductor. γ is the conductivity and r is the radius of the conductor.

As an example, Fig. A1 shows a picture of a high-speed induction motor having a copper coated solid steel rotor with the calculated magnetic field solution. It shows how the copper coating is divided into bars in order to model it with the endrings. Fig. A2 shows the output file of post-processed data of the same motor in a time domain. It can be seen that the motor was fed with one voltage pulse per half a cycle.

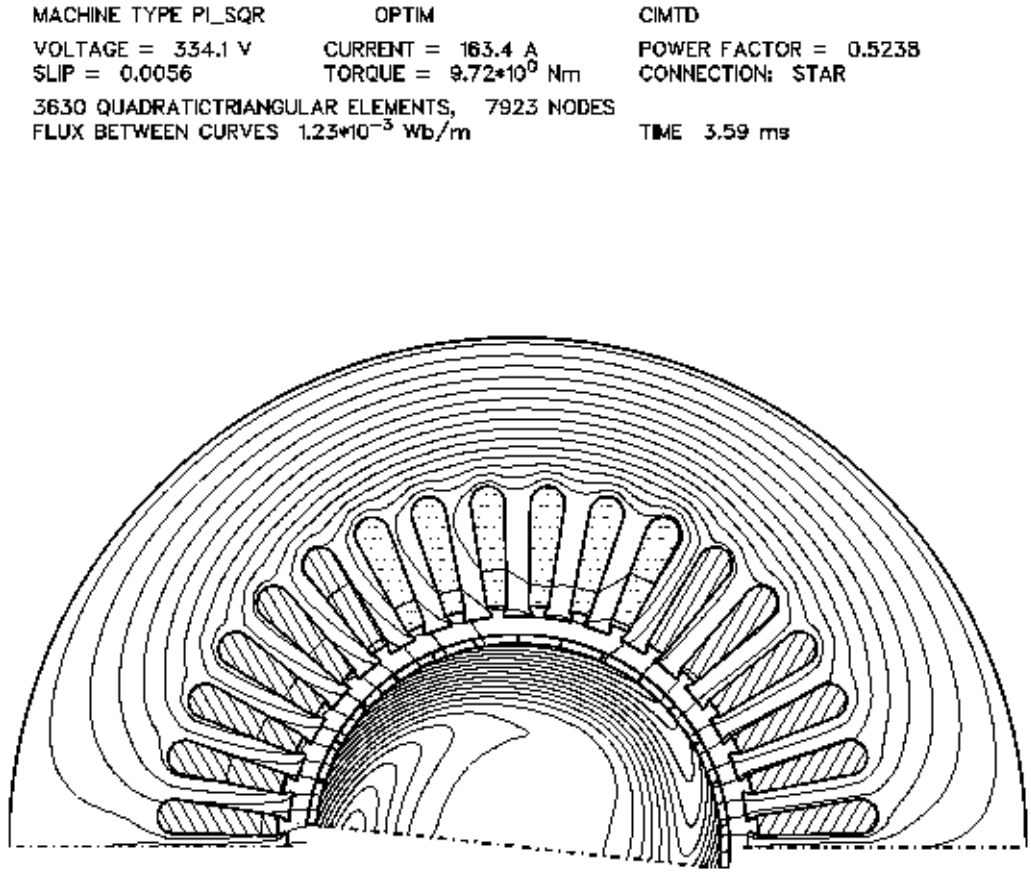

Fig. A1 Calculated field and the design of a high-speed induction motor with a copper coated rotor.

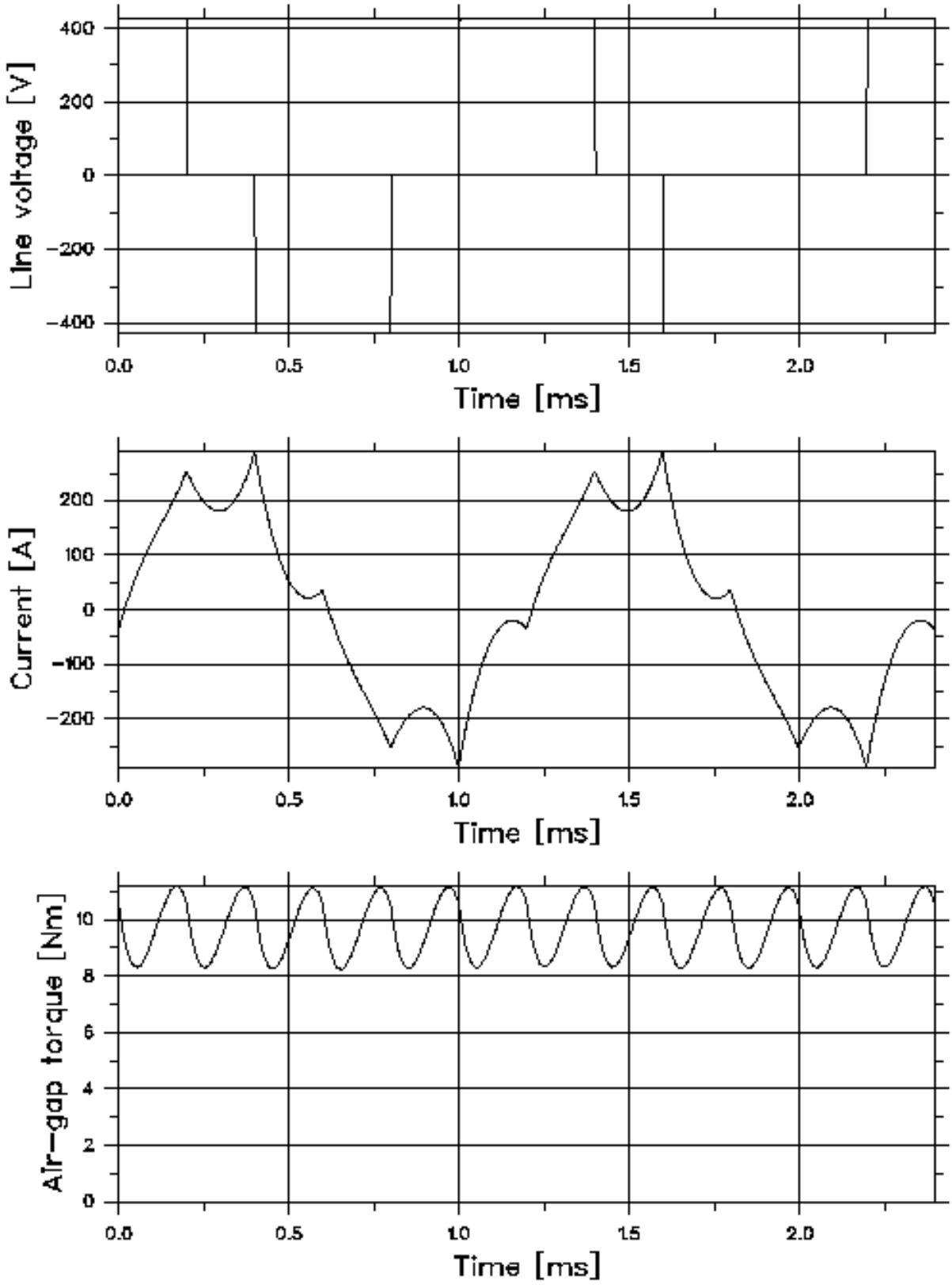

Fig. A2 Post-processed data of a high-speed induction motor with a copper coated rotor calculated with FEM.

B. CALCULATION OF THERMAL CHARACTERISTICS

The thermal calculations model uses equivalent thermal circuits to calculate temperature rises in different parts of electric machines. Here, only a short review of the model is given.

There is an analogy between thermal and electric circuits. A heat flow corresponds to an electric current and a temperature corresponds to a voltage. A heat flow resistance corresponding to an electric resistance is defined by the dimensions and the heat transfer properties of the flow path.

The model is used to calculate only static cases. Thus, the thermal circuits have only resistive components. In forced cooled high-speed motors, the convection dominates the radiation as a heat transfer mechanism.

The equivalent thermal circuit is solved using a node point formulation. The electromagnetic loss components are calculated by the 2D-FEM software. The friction and cooling losses are calculated by the thermal calculation software. The temperature rise vector $\boldsymbol{T}$ is solved from the following equation:

$$\boldsymbol{G}\boldsymbol{T} = \left(\boldsymbol{G}_{\mathrm{str}} + \boldsymbol{G}_{\mathrm{c}}\right)\boldsymbol{T} = \boldsymbol{P}\,, \tag{B1}$$

where $\boldsymbol{P}$ is the power loss vector and $\boldsymbol{G}$ is the thermal conductance matrix including the conductance matrix $\boldsymbol{G}_{\mathrm{str}}$ for the mechanical structure and the conductance matrix $\boldsymbol{G}_{\mathrm{c}}$ for the cooling flows.

Fig. B1 shows the geometry of a high-speed induction motor with a copper coated solid steel rotor. The geometry is parameterized and this parameterization can be utilized with the modeling and optimization software used in this study. The equivalent thermal network corresponding to the geometry can be seen in Fig. B2. The formulas and values for the parameters in Fig. B2 can be found in Saari (1998).

Reference

Saari J. 1998. **Thermal Analysis of High-Speed Induction Machines**. Acta Polytechnica Scandinavica, Electrical Engineering Series No. 90. Helsinki, Finland. 73 p.

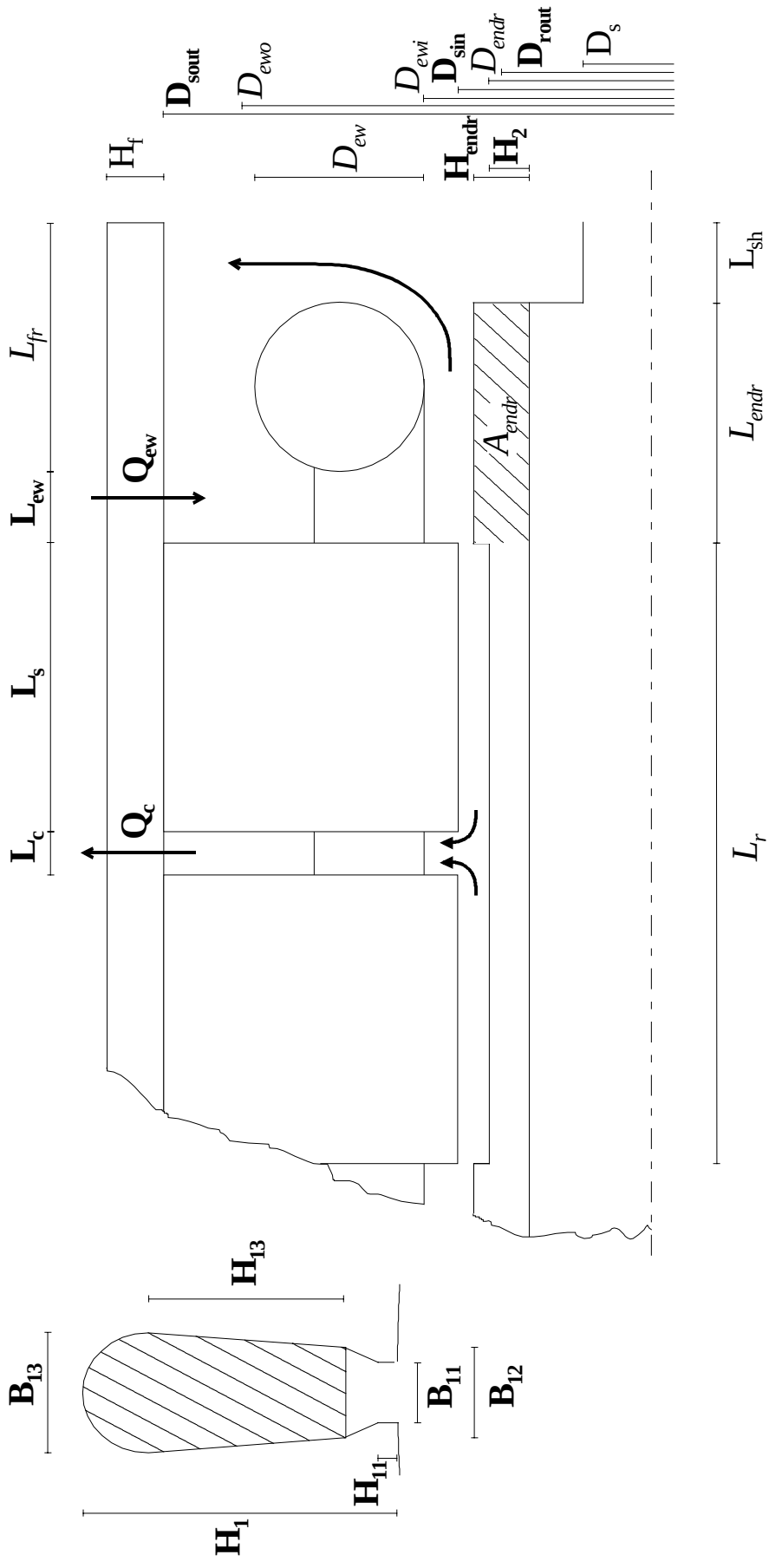

Fig. B1 The parametrized design of a high-speed induction machine. The cooling air flows are shown with the bold face arrows

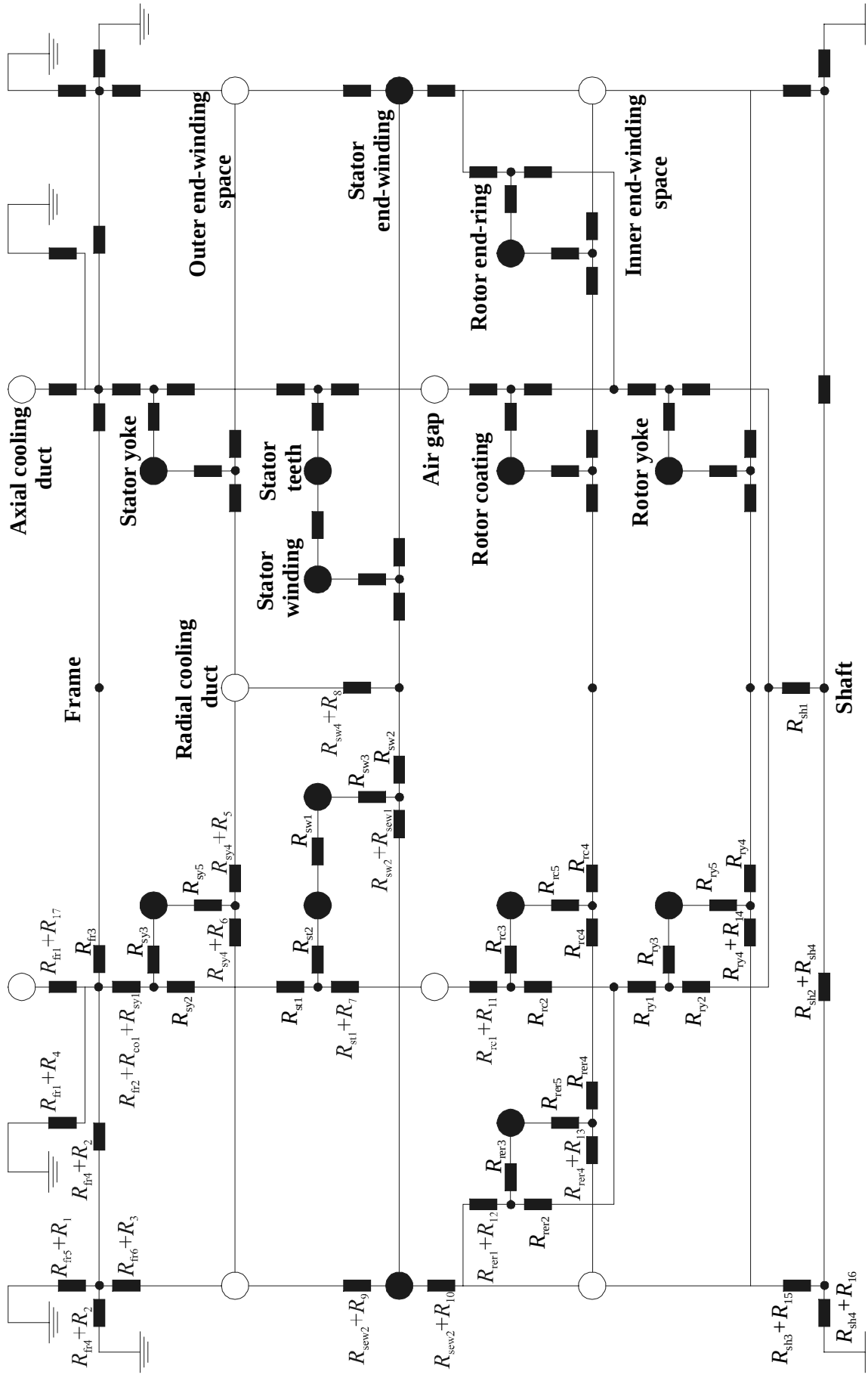

Fig. B2 Circuit diagram of the thermal network. Big black nodes are the heat sources calculated by finite element analysis. Big white nodes are situated in the air space and friction and cooling losses are heat sources there. Circuit ground is the ambient air temperature

C. GENETIC ALGORITHM

The idea in genetic optimization is to imitate the evolution of nature. A whole population of designs is studied instead of a single one. Each design has a design vector consisting of the values of the design variables. This vector $\boldsymbol{x}$ can be viewed as a chromosome where a single design variable corresponds to one gene

$$\boldsymbol{x} = [x_1,...,x_n], \tag{C1}$$

where x_i is a value of i:th design variable and n is the number of variables.

Genetic operators imitate the phenomena in nature which change the genes of the designs. These operators can be divided into mutation and crossover operators. Mutation operators change the value of one or more genes in a chromosome. Crossover operators imitate breeding where two designs give birth to new designs. In this case, the genes of the new designs are a mix or a combination of the parents' genes. New design vectors replace some of the old ones and thus we have a new generation of the population. Selection routines that select the parents for breeding and the individuals to perish imitate the selective laws of evolution in nature. Strong individuals are more likely to produce offspring and weak individuals are more likely to die.

The GA program used in this study has the following algorithm:

1. Initialize a population of designs
2. Evaluate each design in a population
3. Select designs for breeding and designs to die
4. Apply genetic operators to create new designs
5. Replace the dying designs with the new designs
6. Evaluate the new designs in a population
7. To continue the optimization, return to step 3. Otherwise return the solution.

The program can handle the following types of linear constraints.

Domain constraints $\boldsymbol{l} \leq \boldsymbol{x} \leq \boldsymbol{u}$, (C2)

where $\boldsymbol{l} = [l_1,...,l_n]$ and $\boldsymbol{u} = [u_1,...,u_n]$.

Linear equalities $\boldsymbol{Ax} = \boldsymbol{b}$, (C3)

where $\boldsymbol{A}=(a_{ij})$, $\boldsymbol{b}=[b_1,...,b_q]$, $1 \leq i \leq q$, $1 \leq j \leq n$ and q is the number of equalities.

Linear inequalities $\boldsymbol{Cx} < \boldsymbol{d}$, (C4)

where $\boldsymbol{C}=(c_{ij})$, $\boldsymbol{d}=[d_1,...,d_m]$, $1 \leq i \leq m$, $1 \leq j \leq n$ and m is the number of inequalities.

Domain constraints are necessary to limit the search space into a reasonable domain. In addition, some of the genetic operators use the boundaries of the domain in search of better designs much for the same reason as in boundary search methods. Non-linear constraints can be taken into account with linearization of the constraints or with penalty functions.

Linear equality constraints can be eliminated and used to decrease the number of design variables by representing some of the variables as a linear combination of the others. Another benefit of linearity of the constraints is that the search space is always convex. Convexity guarantees that the offspring produced by some of the genetic operators fulfill the constraints automatically.

As an input to the GA software, the user gives the size of the population, the number of generations and the number of times the genetic operators are applied within each generation. Parameters for the operators and for the selection algorithms are also given together with the constraints. The genetic operators are:

Uniform mutation: one of the design variables x_i is given a random value within a feasible domain. Because of the inequality constraints the feasible domain of a design variable is dynamic. The domain changes with the change of the values of other design variables $l_i^{\mathrm{d}} \leq x_i \leq u_i^{\mathrm{d}}$.

Boundary mutation: one of the design variables x_i is given either a lower or upper boundary value of the dynamic feasible domain $x_i = l_i^{\mathrm{d}}$ or $x_i = u_i^{\mathrm{d}}$.

Non-uniform boundary mutation: the value of one design variable x_i is mutated either with higher or lower part of the dynamic feasible domain

$$x_i = x_i + \left[r\left(u_i^{\mathrm{d}} - x_i\right)\left(1 - \frac{t}{T}\right)^B \right] \text{ or} \tag{C5}$$

$$x_i = x_i - \left[r\left(x_i - l_i^{\mathrm{d}}\right)\left(1 - \frac{t}{T}\right)^B \right] \tag{C6}$$

where B is an operator parameter, t is the number of a current generation, T is the number of generations total and r $\in$]0 1[.

Whole non-uniform boundary mutation: the same as non-uniform boundary mutation but the operator affects all the design variables of $\boldsymbol{x}$.

Whole arithmetical crossover: two parent vectors $\boldsymbol{x}^{p1}$ and $\boldsymbol{x}^{p2}$ are selected. Two new design vectors are then of the form

$$\boldsymbol{x}_{1(2)} = a\boldsymbol{x}^{p1(2)} + (1-a)\boldsymbol{x}^{p2(1)} \tag{C7}$$

where $a \in \,]0\ 1]$ is an operator parameter. Because of the convexity of the search space, the new design vectors automatically fulfill the constraints.

Simple arithmetical crossover: two parent vectors $\boldsymbol{x}^{p1}$ and $\boldsymbol{x}^{p2}$ are selected. Two new design vectors are then of the form

$$\boldsymbol{x}_{1(2)} = \left[x_1^{p1(2)},\ldots, x_c^{p1(2)}, \left(ax_{c+1}^{p1(2)} + (1-a)x_{c+1}^{p2(1)}\right),\ldots, \left(ax_n^{p1(2)} + (1-a)x_n^{p2(1)}\right)\right] \tag{C8}$$

where $a \in \,]0\ 1]$ is an operator parameter. In this case the validity of the new vectors in respect to the constraints must be checked. a is given different values and the validity is checked. If no eligible solution is found within a reasonable number of trials, a is given the value of unity and

$$\boldsymbol{x}_{1(2)} = \boldsymbol{x}^{p1(2)} \tag{C9}$$

The selection of the parent designs for the crossover operators is based on ranking the individual designs in the population. The best design is ranked first and the worst is ranked last. Each design, i:th in rank, is assigned a probability $p(i)$

$$p(i) = Q(1-Q)^{i-1},\ \ i=1,\ldots,S \tag{C10}$$

where $Q \in \,]0\ 1[$ is a probability parameter and S is the number of designs in the population. The greater the probability, the better the chances of being selected. A design can be chosen to be a parent in more than one crossover operation. To keep the size of the population constant, old designs must be removed in order to make room for the offspring of the crossover operations. The probability of removal is calculated in the same manner as the probability of parenthood. The only exception is the best design, which cannot be removed. This exception is called an elitist rule that assures smooth evolvement of the population. Optimization algorithm also checks that mutated designs are not removed.

A mutation can happen to every design regardless of its rank. Then the probability for mutation is the same for every design. The only exception is, again, the best design, which is kept intact. A mutation changes an old design in such a way that the size of the population does not change.